AN INNOVATIVE EPITAXIAL GROWTH METHOD FOR MINIMIZING DISLOCATIONS IN THIN-FILM QUANTUM-DOT OPTOELECTRONIC AND PHOTOVOLTAIC DEVICE APPLICATIONS

by

JATEEN S. GANDHI

Presented to the Faculty of the Graduate School of

The University of Texas at Arlington in Partial Fulfillment

of the Requirements

for the Degree of

DOCTOR OF PHILOSOPHY

THE UNIVERSITY OF TEXAS AT ARLINGTON

December 2011

ACKNOWLEDGEMENTS

This work was supported in part by the NSF under awards ECCS-1002133 and DMR-0821745, by NASA under awards NCC-1-02038 and NCC-8-236, and by a Texas Instruments, Inc. Gift award.

First I would like to express my deepest gratitude towards Dr. Wiley P. Kirk for giving me an opportunity to work with him. An opportunity that was accompanied by a strong guidance to research, countless technical discussions and not to forget persistent attempts of proofing this write up. I also would like to present my profound acknowledgement to Dr. Choong-un Kim for his tireless enthusiasm, indispensable tutelage at compelling times and unending encouragements. I am obliged, forever, to both of you.

I want to thank my committee members, Dr. Michael Jin, Dr. Roger D. Goolsby and Dr. Yaowu Hao for their participation and evaluation of my dissertation, especially, Dr. Jin for various discussions and also for allowing me to use his lab for sample characterizations. I want to give a special thanks to Dr. Kevin Clark, who helped me initiate this work by training me on the MBE and also for providing useful discussions. Speaking of MBE, thank you Mr. Eduardo Maldonado for helping me out with the sample growths. Also my team-mate, Mr. Rick Agrawal, for getting me acquainted with various tools in the NanoFAB. I also want to thank Dr. Anton Malko, at The University of Texas at Dallas, for conducting the much needed photoluminescence characterizations. Also Dr. Cheolwoong Yang at the Department of Advanced Materials Science and Engineering, Sungkyunkwan University, Republic of Korea, for helping us out with the HRTEM sample characterizations. Dr. Lian-Shan Chen, I appreciate your help during metal depositions. Various colleagues at UT Arlington thank you for your support. I want to thank Mrs. Jennifer Standlee and Mrs. Libia Cuauhtli at the Materials Science and Engineering Department for their constant help and support.

This note would be empty without a mention to my family. Thank you Mama and Bhavasa for your support ever since I decided to pursue higher education. Thank you very much Nisha, my wife, for standing beside me during each phase of my life. My twin brothers, Nitin and Bipin, thank you for taking care of our parents while I was away from home. My entire family, I would not have reached where I am right now without your love and support.

I have saved the best for last. I deeply appreciate the encouragement and support from my friends. My feelings for you could not be expressed in a better way than this quote –

*"A fella ain't got a soul of his own, but on'y a piece of a big one".**

December 9, 2011

* Steinbeck, John; *The Grapes of Wrath*, The Viking Press, 1939, p 534

ABSTRACT

AN INNOVATIVE EPITAXIAL GROWTH METHOD FOR MINIMIZING DISLOCATIONS IN THIN-FILM QUANTUM-DOT OPTOELECTRONIC AND PHOTOVOLTAIC DEVICE APPLICATIONS

Jateen S. Gandhi, PhD.

The University of Texas at Arlington, 2011

Supervising Professor: Choong-un Kim

A new buffer layer method for epitaxial growth of lattice-mismatched semiconductor quantum-dots based *p-i-n* structures is presented. To our knowledge this is the first instance of a dislocation-reduction approach that has shown reduced dark current behavior in a quantum-dot device compared to its counterpart homojunction *p-n* device consisted of the barrier material.

The present work compared a lattice misfit strain build-up behavior between an $In_{0.15}Ga_{0.85}As$ (*p*) / InAs (*i*) / $In_{0.15}Ga_{0.85}As$ (*n*) (QD) device to an $In_{0.15}Ga_{0.85}As$ (*p*) / $In_{0.15}Ga_{0.85}As$ (*n*) (HOM) device, as both were grown on an un-doped gallium arsenide (GaAs) (100) substrate. The intrinsic region of QD device incorporated 5 layers of 2.1 ML indium arsenide quantum dots that were fabricated using self-assembly *via* Stranski-Krastanov strain release mechanism. Atomic force microscopy measurements exhibited 35 ± 3 nm sized pyramidal islands with a narrow distribution and a density of 2.5×10^{10} per cm^2. A low temperature (6K) photoluminescence characterization of the QD sample revealed an activity at 1400 nm

wavelength that was attributed to optical pumping of carriers, which experienced a 3-dimensional quantum confinement due to a potential well formed by $In_{0.15}Ga_{0.85}As$ matrix, and their subsequent radiative recombination. Both of the QD and HOM samples were characterized using x-ray diffractometer (XRD) and a high resolution transmission electron microscopy (HRTEM) method. The XRD data recorded a signature of the biaxially strained pseudomorphic section of $In_{0.15}Ga_{0.85}As$ buffer layer that absorbed a lattice misfit due to epitaxial growth on GaAs substrate. This signature consisted of a set of twin peaks at higher and lower 2θ degrees resembling elastically strained and plastically relaxed sections, respectively, of the buffer layer residing in the vicinity of buffer-GaAs interface. A comparison of those peaks between QD and HOM samples exhibited an increase in the volume of the plastically relaxed region in HOM sample and a cross-sectional HRTEM image revealed absence of dislocations within the intrinsic region of QD sample. A current-voltage characterization using a four-probe tool recorded lower dark current from the QD device compared to HOM that, along with XRD and HRTEM results, confirmed an enhanced elastic absorption of the lattice misfit in the QD device. The buffer layer method is advantageous in the field of epitaxial growth due to the virtues of simplicity, efficient device fabrication, improved thermal stress performance and easier strain build-up management.

TABLE OF CONTENTS

LIST OF ILLUSTATIONS

LIST OF TABLES

CHAPTER 1

INTRODUCTION

[A] dislocation is haunted by its past
– J. D. Eshelby, Phil. Trans. A, 244, 1951

1.1 Overview

Dislocation generation by strain energy is an inherent issue when growing thin-film epitaxial structures of low-dimensional semiconductors [1.1]. Epitaxial growth of quantum confined lower band-gap materials, *e.g*. indium arsenide (InAs) quantum dots (QDs), within a different lattice matrix of higher band-gap material, *e.g*. gallium arsenide (GaAs), generates epitaxial strain due to the lattice constant difference between the two materials. Because of limited mechanical properties, the semiconductor can only absorbs lattice strain up to a critical point, beyond which the absorbed strain energy is released by interface misfit dislocation generation [1.2]. These dislocations function as traps for excited carriers in optoelectronic devices, thereby degrading their performance. The main purpose of this research is to address the issue of epitaxial strain encountered in the growth of III-V QD based semiconductor devices and to show through experimental measurements and quantitative analyses some methods that can lead to improved device performance even when epitaxial strain is present.

In 1934 Orowan, Taylor and Polanyi demonstrated the concept of dislocations [1.3]. It took more than a decade for the development of this concept into a thermodynamic model by Frank and van der Merwe (FVM) [1.4]. FVM introduced a one-dimensional model consisting of metals with different lattice constants. Using strain energy balance, FVM identified a critical thickness beyond which the growth incorporated dislocations through strain release. Later in 1974 Matthews and Blakeslee (MB) reported generation of misfit dislocations in semiconductors

by studying multilayer growth of GaAs/GaAsP on GaAs substrates using vapor deposition [1.2]. As an extension to the FVM model, MB used continuum elasticity theory to formulate critical thickness of lattice-mismatched semiconductors in layers that would trigger dislocation generation. MB's series of publications formed the foundation for the strain analysis field throughout the era of semiconductor miniaturization [1.5]. Even though the motivation behind the development of low-dimensional semiconductor devices, *e.g*. quantum dots (QDs), has led to a drastic transformation in optoelectronic properties and capabilities [1.6], their success has been mostly judged by their effect on device performance [1.1].

Low-dimensional semiconductor devices consist of lower band-gap structures incorporated within a higher band-gap matrix. Over the last few decades epitaxial growth, *e.g.* by molecular beam epitaxy (MBE), has shown considerable success in the fabrication of such devices [1.7]. Even though MBE is not a particularly cost-effective technique for manufacturing applications, its atomic reproducibility and suitability in broad device applications has led to its wide acceptance in academic studies and for certain important specialized industries. In epitaxy the atoms of the growing layer, called the epilayer, are covalently bonded to the atoms on the surface of the underlying substrate. If the two materials to be grown epitaxially have identical lattice constants then there is no mismatch strain. However, if the two materials with varying band gaps also have different lattice constants then the covalence during epitaxial growth inevitably results in misfit strain incorporation that subsequently leads to defect generation. These defects function as carrier traps, which diminish the performance of optoelectronic devices.

The selection of an epilayer alloy with a lattice constant that matches the substrate would primarily avoid any misfit strain induced dislocation generation. But this method suffers from the limitation in the desired freedom of the band-gap choice for the epilayer. Most optimal designs of optoelectronic devices require band-gap selection and the engineered utilization of lattice mismatched systems. In this project we have employed epitaxial lattice strain to

effectively grow lower band-gap quantum dot structures within a higher band-gap matrix which utilizes misfit strain to manipulate and manage defect generation.

1.2 Misfit Strain and its Consequences

The misfit strain *f* is the difference between the lattice constants of the substrate (δ_0) and the epilayer (δ_a), as given by equation 1.1.

$$f = \frac{\delta_a - \delta_0}{\delta_0} \tag{1.1}$$

Semiconductor III-V materials possess certain mechanical properties. Those properties are described by the elastic stiffness tensor [C] [1.8].

$$[C] = \begin{bmatrix} C_{11} & C_{12} & C_{12} & 0 & 0 & 0 \\ C_{12} & C_{11} & C_{12} & 0 & 0 & 0 \\ C_{12} & C_{12} & C_{11} & 0 & 0 & 0 \\ 0 & 0 & 0 & C_{44} & 0 & 0 \\ 0 & 0 & 0 & 0 & C_{44} & 0 \\ 0 & 0 & 0 & 0 & 0 & C_{44} \end{bmatrix} \tag{1.2}$$

This elastic stiffness tensor takes the form of 1.2 as a 2nd order tensor due to the tendency of III-V materials to crystallize into zinc-blende structures. The elastic stiffness constants (or the coefficients of the elastic stiffness tensor) C_{11}, C_{12} and C_{44} are associated with the elastic properties of the atomic bonds as expressed in units of force per unit area. Suppose a III-V semiconductor, *e.g.* indium arsenide (InAs, δ_a = 6.058 Å, C_{11} = 8.34 x 10^{11} dyn/cm^2, C_{12} = 4.54 x 10^{11} dyn/cm^2, C_{44} = 3.95 x 10^{11} dyn/cm^2), is epitaxially grown over a lattice mismatched substrate, *e.g.* gallium arsenide (GaAs, δ_0 = 5.653 Å, C_{11} = 11.90 x 10^{11} dyn/cm^2, C_{12} = 5.34 x 10^{11} dyn/cm^2, C_{44} = 5.96 x 10^{11} dyn/cm^2). Epitaxy leads to coherent (one-to-one) atomic bonding of InAs to the dangling bonds at GaAs surface. Due to lattice mismatch the atomic bonds of the epilayer suffer elastic straining. This leads to bi-axial distortion of the bonds forming a strained overlayer. The energy per unit area of the strained overlayer is given by,

$$E_\varepsilon = \varepsilon^2 Y h \tag{1.3}$$

where ε is the elastic strain, *h* is the thickness of the overlayer and *Y* is the Young's modulus under biaxial stress given as,

$$Y = \frac{1}{2}(C_{11} + 2C_{12})\left[3 - \frac{C_{11} + 2C_{12}}{C_{11} + 2(C_{44} - C_{11} + C_{12})(l^2m^2 + m^2n^2 + l^2n^2)}\right] \tag{1.4}$$

where *l*, *m* and *n* are the directional cosines of the angles between the normal to the interface and the cube axes. Equation 1.4 is applicable to anisotropic semiconductor systems. Matthews assumed an isotropic system with the Young's modulus given by,

$$Y = 2G\frac{(1+v)}{(1-v)} \tag{1.5}$$

where *G* and *v* are the shear modulus and Poisson's ratio respectively. From 1.3 it is implied that with thicker over layer growth the elastic strain energy increases. To relieve elastic strain dislocations in the lattice structure are produced. These are generated by breaking atomic bonds that destroys the one-to-one coherency in the atomic array. The energy per unit area of an epilayer with a dislocated array is given by,

$$E_d = 2\left(\frac{1}{s}\right)\left[\frac{1}{2}Db(1 - v\cos^2\alpha)\right]\left[\ln\left(\frac{R}{b}\right) + 1\right] \tag{1.6}$$

where *s* is the spacing between dislocations, *D* is the average shear modulus, *b* is the magnitude of Burger's vector and *R* is the cut-off radius of the dislocations energy. Along with E_ε and E_d the surface energy of the newly formed epilayer, E_{surf}, forms an interplay that leads to, mainly, three scenarios:

1. If E_ε does not exceed the dislocations generation energy, E_d, and is less than E_{surf} then the epilayer absorbs the misfit strain. This growth results in coherent interface with 100% atomic registry. Suffice it to say that only a section of the epilayer in the vicinity of the epi-substrate interface stores the strain energy. This pseudomorphic, biaxially strained epilayer exhibits an intermediate lattice constant between δ_a and δ_0. In this case the total misfit is said to be absorbed elastically, $f = \varepsilon$.

2. If E_ε exceeds E_d, while being lower than E_{surf}, then the epilayer prefers forming dislocations to reduce elastic strain. In this scenario a part of the misfit is released by forming plastic strain (p). Then the average lattice constant of the epilayer with defects shifts further towards δ_0. The strain energy is released until it is equal to or less than the E_d. So epilayer exhibits both elastic and plastic strains, $f = \varepsilon + p$.
3. If E_ε exceeds E_{surf} however is less than E_d then the epilayer releases the strain by forming nanometer sized islands, as seen in Fig. 1.1. Formation of islands increases the epilayer's surface area, thereby increasing its surface energy. The island relaxes to its intrinsic lattice constant, δ_a, resulting in reduction of the absorbed strain energy. This mechanism is called as the Stranski-Krastanov (SK) growth mode [1.9]. The SK mode is limited to high misfit strain, f, which is released within the deposition of a few atomic monolayers. The SK mode, to a certain extent, retains coherency and proves [1.10] to be an effective technique to incorporate nanometer sized islands, such as quantum dots, within higher band gap matrix.

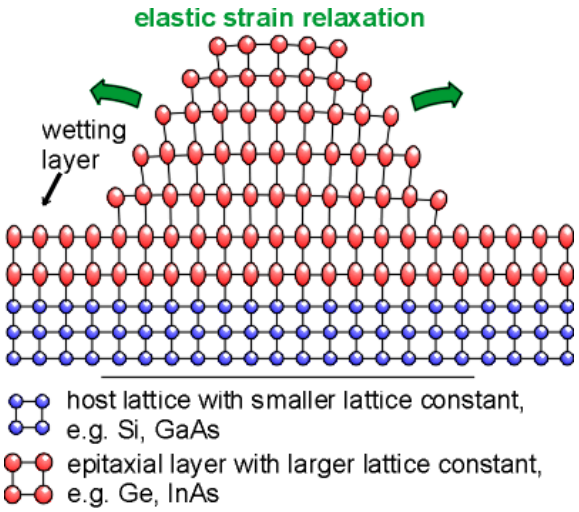

Fig. 1.1 Island formation by epitaxial strain release via the SK growth mode, from [1.11]

The SK mode has led to the study of epitaxial growth of quantum dots while the first (FVM) and second (MB) mechanisms form the basis of the study of epitaxial strain and

dislocation generation in lattice mismatched devices. Many recent studies of QD based *p-i-n* devices have employed the strain compensation (SC) technique [1.12, 1.13]. Those studies involved techniques of epitaxial growth of alternate layers of materials with larger and smaller lattice constant, so that the average lattice constant of the epilayer theoretically matched the host material. SC relies on the MB model of critical thickness by utilizing average lattice constant of the multilayer growths. This technique has proved partially beneficial in the improvement of device performance; however, the inclusion of quantum dots inherently generated dislocations within the final structures as reported in the literature [1.14-1.17]. The current status and understanding of growth mechanisms and defect control suggests that the thermodynamics of the strain release mechanism should be more thoroughly examined. During the course of this project we have observed all of the aforementioned three strain release scenarios. Our measurements and data analysis suggests that the generation of dislocations within QD based devices can be successfully suppressed. The data and associated analysis will be presented in detail in forth coming chapters of this dissertation. We have, for example, analyzed the fundamentals governing the strain release without employing any strain compensation (SC) method.

1.3 Contents of the Dissertation

The purpose of this project is to explore epitaxial strain release behavior for the growth of lattice mismatched InAs quantum dots based on $In_xGa_{1-x}As$ *p-i-n* devices. The schematic of our targeted growth structure is shown in Fig. 1.2. We chose molecular beam epitaxy (MBE) to grow this device because it offers advantages of atomic reproducibility. An InGaAs alloy was chosen as the host matrix to provide band-gap variation and lattice constant freedom. InAs was chosen for its combination low band-gap (0.36 eV) and high lattice misfit with the host, and in addition it provides a useful optoelectronic device application along with strain-induced island formation. The grown samples were analyzed for both epitaxial strain incorporation and the misfit strain induced dislocation generation. After the introductory Chapter 1, the remainder of this dissertation is organized around the following chapters:

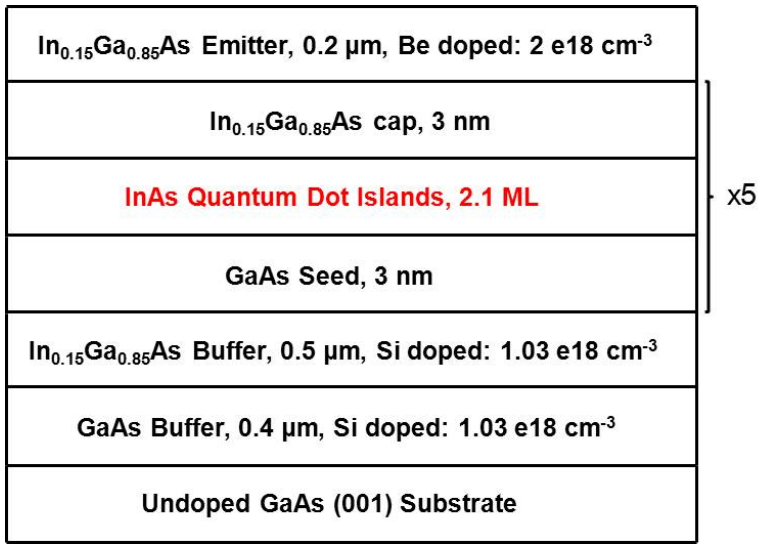

Fig. 1.2 Design of MBE growth structure for InAs quantum-dot based *p-i-n* devices.

Chapter 2 provides background for the quantum physics of nano-sized devices, the epitaxial growth theory and the development of epitaxial strain release theory. We also discuss the diode physics necessary for the *p-i-n* device performance evaluation.

Chapter 3 discusses the experimental techniques of growth and characterization. We employed molecular beam epitaxy for sample growth, optical lithography for *p-i-n* device fabrication, followed by various imaging techniques, spectroscopic techniques, and current-voltage device characterization to measure long wavelength photocurrent behavior.

Chapter 4 addresses issues encountered while optimizing epitaxial growth of *p-i-n* devices along with structural and electronic characterization of the grown layers and islands.

Chapter 5 concentrates on the strain release phenomenon. In this chapter we present analytical data that would amend the method of strain release analysis using the MB model. Our method employs a cumulative strain calculation to explain how an InAs/InGaAs QD device exhibits suppressed generation of dislocations and enhanced device performance as compared to an InGaAs *p-n* homojunction device. We advance that our experimental results and the

resulting analysis of the data expands and deepens the current and general fundamental understanding about how epitaxial strain incorporation and release phenomena operate.

In Chapter 6 we conclude the dissertation with a discussion on the application of epitaxially grown structures formed as solar cell devices. In this chapter we present the device performance under near infrared illumination conditions and the photocurrent contributions from the islands with suggested directions for future work.

CHAPTER 2

BACKGROUND

Thin-film structures have been a center of attraction not only for the IC and various other optoelectronic industries but also for strain engineering research for at least the past three decades. Acting as a unique candidate that presents opportunities for band gap tuning of lattice mismatched devices, thin-film structures especially ones incorporating quantum dots have driven the understanding of dislocation generation phenomenon into a new realm. A constant effort has been made to minimize dislocations within these types of thin-film semiconductor structures by adopting new methods of device growths that would improve the pre-assessment of misfit strain release behavior. In this chapter we present an innovative method of epitaxial growth that suppresses the generation of misfit dislocations in a thin-film quantum-dot device. This chapter is organized into four sections.

- Section 2.1 introduces the concept of misfit strain and the need for a lattice-mismatched device. It is followed by a discussion concerning the evolution of the dislocation generation theory to predict a critical thickness for an epilayer that would release the absorbed strain energy. Also a brief discussion of the thermodynamics of epitaxial growth of uniform films is added followed by some methods attempted previously in the literature to minimize dislocations and their shortcomings.
- Section 2.2 is primarily concerned with the effects of strain on the fabrication of thin-film structures and the corresponding alteration of the optoelectronic properties. A brief discussion outlines the motivation behind semiconductor miniaturization and quantum confinement effects. Also the strain behavior

on the thermodynamics of epitaxial growth and the subsequent efforts in optimizing the kinetics to fabricate dislocation free structures is presented. Experimental evidence indicated a definite set of boundary conditions, as already established in the literature, for epitaxial growth of such structures is outlined.

- Section 2.3 discusses thin-film structure based semiconductor *p-i-n* devices for photovoltaic applications. Recent efforts of a strain compensation method consisting of alternate tensile and compressively strained epilayer growths to match the average lattice constant of the stack to the underlying gallium arsenide substrate are discussed. Although this method has managed to improve the performance in certain aspects, it inherently incorporates dislocations within the intrinsic region that has proven to be detrimental.
- Section 2.4 presents our innovative approach of epitaxial growth that minimizes dislocation generation. Within the course of the project a thin-film device was discovered to perform better than the corresponding control device without an intrinsic region that has led us to an understanding for introducing an innovative growth method. We present a scenario whereby lattice mismatched growth, resembling our device structure, is able to control the strain build-up in a thin-film structure better than previous efforts aimed at reducing dislocation formation in uniform film and intrinsic growth regions.

2.1 Strain in the Epitaxy Layer and Mediation

Fig. 2.1 [2.1] shows a plot of semiconductor band gap, in eV on y-axis, as a function of the lattice constant, in Å on x-axis, for III-V and II-VI semiconductors. Pentagonal and hexagonal features represent primary semiconductors while connecting curves represent ternary and quaternary alloys. The lattice constant of a semiconductor alloy varies linearly with the fraction of the constituents satisfying Vegard's law [2.2] while the band gap of that alloy follows a parabolic relation given by [2.3],

$$E_g = a + bY + cY^2 \tag{2.1}$$

where *a* and *b* are the material properties while *c* is the bowing coefficient that is comprised of a periodic component, c_i, which accounts for changes in the bond length and an aperiodic component, c_e, which addresses the root-mean-square fluctuation in the potential of an atom from its periodic amplitude.

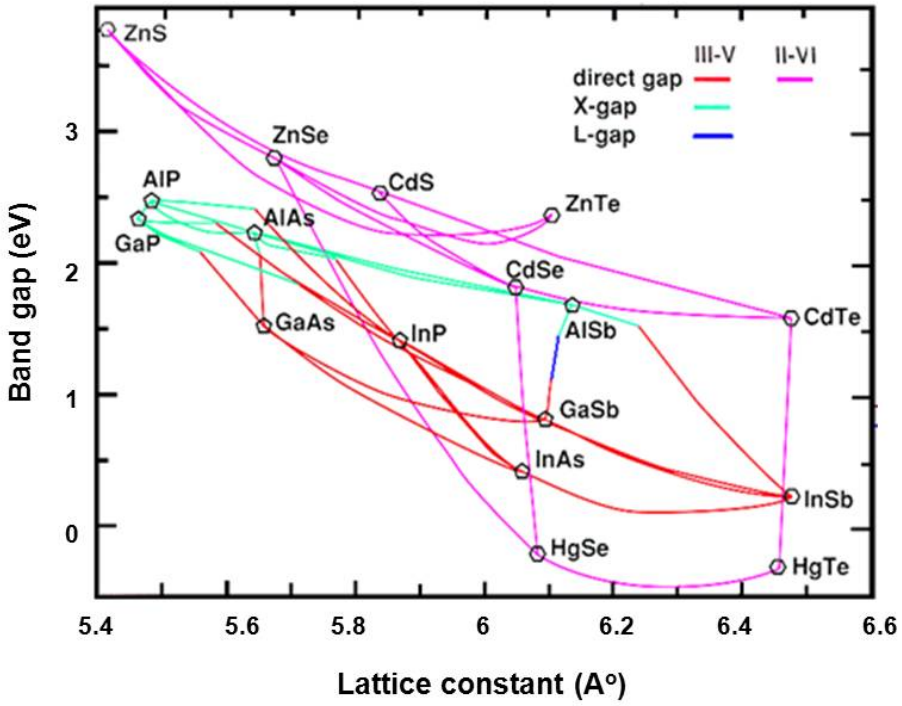

Fig. 2.1 Band gap (eV) vs. Lattice constant (Å) for groups III-V and II-VI semiconductors [2.1]

Now consider epitaxial growth of a ternary alloy $In_{0.53}Ga_{0.47}As$ with a lattice constant (δ_a) 5.8687 Å to be grown on an InP substrate that has a lattice constant (δ_0) 5.8686 Å. The misfit between the two, *f*, is given by Eq. 1.1 as,

$$f = \frac{\delta_a - \delta_0}{\delta_0} \tag{1.1}$$

Substituting δ values for the ternary alloy and the substrate, then *f* is calculated to be $2x10^{-5}$ a.u. For such a small misfit the growth of $In_{0.53}Ga_{0.47}As$ over InP would result in almost

100% atomic registry, *i.e.* atom-to-atom bonding, resulting in coherent growth of a semiconductor device that could exploit optoelectronic performance emerging from band gaps of 0.74 eV and 1.35 eV for InGaAs and InP respectively. However, it should be noted that the optoelectronic performance of this device would be restricted to the aforementioned band gaps, which has limited applications. For alternative optoelectronic applications, band gap engineering would require a selection of different alloy and substrate combinations from Fig. 2.1 even though these combinations would restrict the band gap freedom. In order to achieve a wider band gap selection for a wider range of applications, an alternate option would be to grow devices with ternary and quaternary alloy combinations with mismatched lattice constants. This option introduces misfit strain between the adjacent layers thus creating the core issue of atomic defect generation. For a lattice-mismatched semiconductor device to be grown by an epitaxial method the overlayer is required to absorb *f* at the expense of biaxial straining of the atomic bonds,, which results in the storage of elastic strain energy, E_ε. Once one exceeds the elastic strain energy limits of the epilayer, then E_ε becomes higher than the energy of dislocation generation, E_d, thus favoring the breaking of atomic bonds of the atoms residing at the epilayer-substrate interface, which of course relieves the biaxial strain but on the other hand forms dislocations. These dislocations, however, act as traps for free carriers, which in turn degrade the device performance. Defect generation in the lattice-mismatched systems invites a trade-off between an acceptable amount of misfit and the amount of band gap freedom desired. Theoretical work on the prediction of the elastic strain limit and its demonstration through experimental work has been a topic of interest in the field of crystal growth since the late 1920s and continues to evolve even today. The next section outlines some of the key findings applicable to this early work.

2.1.1 Verhakung *and one dimensional dislocation*

Dehlinger [2.4] first introduced the modern idea of a dislocation proposing that the disturbance of the lattice due to a vacant site, which is the absence of atomic bonding, is

confined within a small region. Within this region the displacement of atoms from the row with a defect is given by a sinusoidal potential curve, see Fig. 2.2 [2.5]. Atoms from a layer above are shown as solid circles lying at various positions while the substrate atoms lie at the troughs of the sine wave. Outside this region the atoms above and below are in perfect registry. Dehlinger called such a disturbance a *Verhakung* (no English translation of this Germanic term exists, but it roughly implies dislocation). Dehlinger's idea indicated that the lattice planes in the neighborhood of a dislocation must be curved. The theoretical basis, however, for the *Verhakung* was realized by Frenkel and Kontorova's (FK) one dimensional atomic chain model. According to FK the potential energy of an atomic chain under displacement at location x is given by [2.6],

$$U(x) = A\sum_n \left(1 - \cos\frac{2\pi x_n}{a}\right) + \frac{1}{2}\alpha\sum_n (x_{n+1} - x_n - a)^2 \qquad (2.2)$$

where n represents the n^{th} atom, a is the lattice constant of the substrate, A is the amplitude of the periodic field and α is the coefficient of the elastic force between the atoms. Dehlinger [2.4] set $x_n = (n + x_n)\cdot a$, where x_n is the displacement (as shown on the y axis of Fig. 2.2), to get,

$$U(\xi) = A\sum_n (1 - \cos 2\pi\xi_n) + \frac{1}{2}\alpha a^2 \sum_n (\xi_{n+1} - \xi_n)^2 \qquad (2.3)$$

Using Dehlinger's approximation that the displacement is accommodated over a short region, the condition for equilibrium for the n^{th} atom is, $\frac{\partial U}{\partial \xi_n} = 0$. A solution to FK's model was given by Frank and van der Merwe (FVM) [2.7]. FVM considered one dimensional epitaxial growth over a solid substrate and replaced $A\cos\frac{2\pi x}{a}$ in Eqn. 2.2 with $A\left(\cos\frac{2\pi x}{a} + r^2\cos\frac{4\pi x}{a}\right)$. In this general form r^2 is the ratio of the amplitude of the second harmonic term, w, to the first harmonic term, W, of the Fourier series. By introducing the second harmonic term FVM model was able to assess the effect of the potential between the two planes of atoms. With an amplitude $W \leq$ ¼

the potential curve exhibited broader maxima and narrower minima, as shown in Fig. 2.3 (a). Significance of this result was that a narrow minima constraints the dislocation formation along a closed packed plane while a broader maxima restricts the displacement of an atom in the vicinity of a dislocation to a narrow range of distance, which would be a reprisal of the *Verhakung*. For $r^2 > ¼$, the potential curve exhibited a subsidiary minima, seen in Fig. 2.3 (b), allowing for the displacement of an atom into a plane other than closed packed plane representing the case for a partial dislocation.

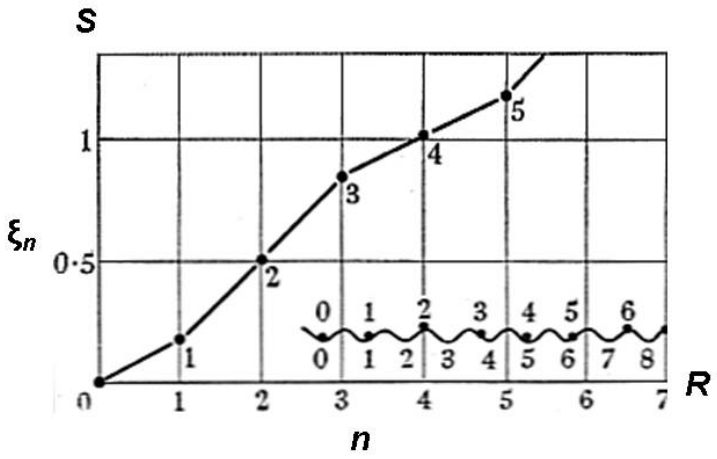

Fig. 2.2 Displacement measured per atom, from [Frank-Van der Merwe, 1949]

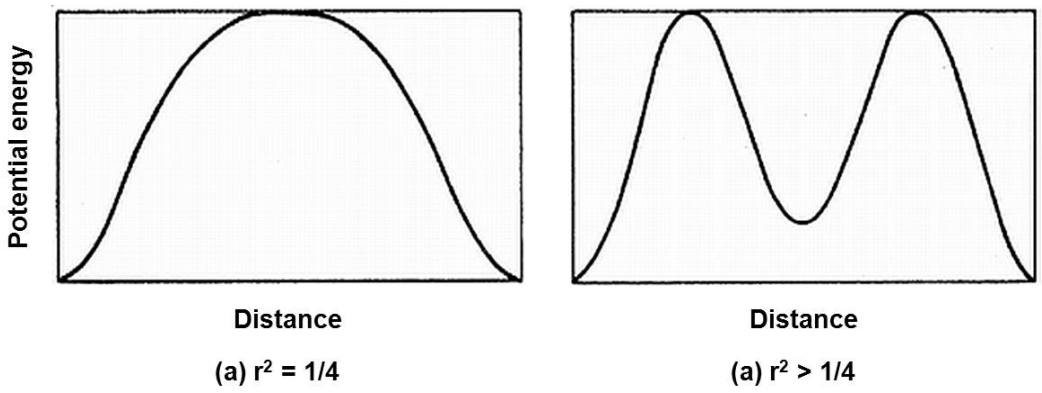

Fig. 2.3 Effect of a second harmonic term on the potential between two atoms [Frank-Van der Merwe, 1949]

Van der Merwe (VM) went on to develop a model for the equilibrium strain within an epitaxially aligned face centered cubic metal film using a strain energy balance approach [2.8],

$$\varepsilon_m = \frac{(1-2\sigma)(2-f)(1+f)\mu_0 a}{8\pi^2(1-\sigma)(2+f)(f\mu_a h)}\beta \ln\left[2\beta\left(1+\beta^2\right)^{1/2} - 2\beta^2\right] \tag{2.4}$$

In Eq. 2.4, ε_m is the equilibrium strain, f is the misfit between the epilayer and the substrate, a is the unstrained lattice constant of the epilayer and h is the thickness of the epilayer. The factor β is given as, $\beta = \frac{8\pi\mu_a f}{(1-\sigma)\left(1+\frac{\mu_a}{\mu_b}\right)(2+f)^2\mu_i}$, in which μ represents the shear modulus of the epilayer (*a*), the substrate (*b*) and the interface (i) and σ is the Poisson's ratio, assumed equal for all of the layers. According to VM, when the epitaxial strain in the grown layer exceeds ε_m, then excessive strain is released by forming dislocations.

Matthews [2.9] compared VM model to the epitaxial deposition of 100 Å gold epilayer on 400 Å of palladium substrate using vapor deposition technique. Electron micrograph analysis revealed a square network of misfit dislocations parallel to [-110] and [-1-10] directions which Matthews noted as a result of the contrast arising from (020) and (220) reflections. Matthews also recorded Moiré fringes as a result of the interference of an un-deviated beam and a beam that experienced (220) and (-2-20) reflections in the gold and palladium layers. Matthew determined the magnitude of Burger's vector components along ±[110] directions by comparing the separation of indexed Moiré fringes with the misfit dislocation spacing. On comparison with the difference between unstrained lattice parameters of gold and palladium Matthew concluded 87% of misfit was accommodated *via* dislocations, within the gold epilayer. On substituting h = 100 Å, a = 4.079 Å, b = 3.89 Å, μ_a = 2.76 x 10^{11} dyn/cm^2, μ_b = 4.03 x 10^{11} dyn/cm^2 and σ = 0.4 into VM model the equilibrium strain ε_m was calculated as 0.065%. For total misfit of 0.046, 100 Å of gold accommodated 1.4% of total misfit elastically while 98.6% was accommodated plastically, *i.e.* by forming misfit dislocations. The VM model clearly

overestimated Matthews' experimental results, thus letting him speculate on three factors that led to this discrepancy.

1. Diffusion between the films led to partial alloying at the interface lowering the total misfit between the epilayer and the substrate.
2. Before depositing gold, palladium was first deposited on a sodium chloride substrate which was later dissolved into water. This altered the total misfit across Au-Pd system as Pd accommodated $1/6^{th}$ while Au absorbed the rest of the misfit.
3. Mechanism of dislocation formation depended on the mode of the epilayer growth. Gold formed nuclei and proceeded via coalescence of those which let dislocation generation at the junction of surface of the substrate and the surface of the overgrown nuclei releasing strain energy, considered first by Cabrera [2.10]. This dislocation generation ceased when nuclei coalesced to form a continuous film. Once a continuous film was formed a new mechanism was needed to further release a misfit. Matthew and Cabrera implied that this led to pseudomorphic straining of the epilayer.

Based on these speculation Matthews went on to develop his own theory of dislocation generation, discussed in the next section, which would address three main topics inherent to the study of dislocations.

- Source of dislocation, which differs according to the mode of epilayer growth
- Strain release mechanism, which is affected not only by crystal structure but also the growth technique
- Accommodation of elastic and plastic strains, which is dictated by the elastic properties of the epilayer

2.1.2 Continuum elasticity theory and critical thickness

Matthews introduced his own theory [2.11] of epilayer strain release by first considering an effective Burger's vector, b_{eff}. His theory is presented through Eqn. 2.9. According to Matthews, if misfit dislocations exist at the interface then the interface dislocation spacing is given by,

$$S = \frac{b_{eff}}{\delta} \tag{2.5}$$

where δ is the lattice constant of the epilayer. Since the generation of dislocations requires a certain amount of energy, then during the initial stages of growth the epilayer will absorb any misfit elastically with 100% registry (coherence). On the account of the elastic properties the strain energy within the epilayer increases. At some thickness, termed critical thickness (h_c), the strain energy is released in the epilayer by forming dislocations. Fig. 2.4 shows (a) strained epitaxial layer and (b) a partially relaxed layer with one interface misfit dislocation.

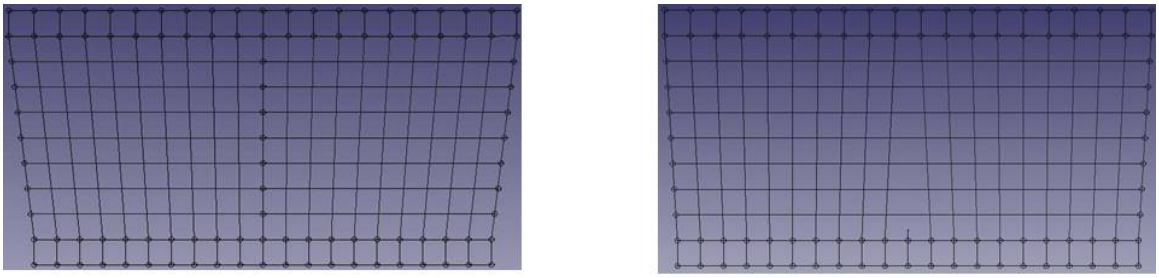

(a) Coherent epilayer (b) Dislocated epilayer

Fig. 2.4 Pseudomorphic epilayers

The strain energy released equals the strain energy required to form a misfit dislocation. FVM model was designed for epitaxial growth of FCC metals using strain energy balance approach while Matthews, on the other hand, developed an expression for critical thickness using continuum elasticity approach. As discussed previously in the Chapter 1 the energy per unit area of the strained overlayer is given by,

$$E_{\varepsilon} = \varepsilon^2 Yh \tag{1.3}$$

where ε is the elastic strain, h is the thickness of the overlayer and Y is the Young's modulus under biaxial stress given as,

$$Y = \frac{1}{2}\left(C_{11} + 2C_{12}\right)\left[3 - \frac{C_{11} + 2C_{12}}{C_{11} + 2\left(2C_{44} - C_{11} + C_{12}\right)\left(l^2m^2 + m^2n^2 + l^2n^2\right)}\right] \tag{1.4}$$

where *l*, *m* and *n* are the directional cosines of the angles between the normal to the interface and the cube axes and C_{ij} corresponds to the elastic constants of the overlayer. Eq. (1.4) is applicable to anisotropic semiconductor systems. Matthews assumed an isotropic system with the Young's modulus given by,

$$Y = 2G\frac{(1+\nu)}{(1-\nu)} \tag{1.5}$$

where *G* and ν are shear modulus and Poisson's ratio, respectively. From (1.3) it is implied that with a thicker overlayer growth the elastic strain energy, E_ε increases. To relieve E_ε dislocations are generated by breaking atomic bonds and the energy per unit area of an epilayer for an array with dislocations is given by,

$$E_d = 2\left(\frac{1}{s}\right)\left[\frac{1}{2}Db\left(1-\nu\cos^2\alpha\right)\right]\left[\ln\left(\frac{R}{b}\right)+1\right] \tag{1.6}$$

where *s* is the spacing between dislocations, *D* is the average shear modulus, is the magnitude of Burger's vector and *R* is the cut-off radius of the dislocations energy. The average shear modulus is given by,

$$D = \frac{G_0 G_s b}{\pi(G_0+G_s)}(1-\nu) \tag{2.6}$$

where G_0 and G_s are the shear modulii of the overlayer and the substrate, respectively. Substituting expressions for a misfit (1.1) and the interface-dislocation spacing (2.5) in Eqn. 1.6 yields,

$$E_d = D\left(\frac{b}{b_{eff}}\right)(1-\nu)(f-\varepsilon)\left[\ln\left(\frac{R}{b}\right)+1\right] \tag{2.7}$$

where ε is the elastic component of the total absorbed misfit, *f*. The total energy of the system is $E_\varepsilon + E_d$. The equilibrium elastic strain, ε, at which the system releases the absorbed strain energy is calculated for the condition, $dE/d\varepsilon = 0$.

$$\varepsilon = \frac{D\left(1-\nu\cos^2\alpha\right)\left(\frac{b}{b_{eff}}\right)\left[\ln\left(\frac{R}{b}\right)+1\right]}{2Yh} \tag{2.8}$$

As h increases, ε decreases up to a critical thickness, h_c, where the epilayer is elastically strained, *i.e.* ε = f leading to an expression for the critical thickness, *viz.*

$$h_c = \frac{D\left(1-\nu\cos^2\alpha\right)\left(\frac{b}{b_{eff}}\right)\left[\ln\left(\frac{h_c}{b}\right)+1\right]}{2Yf} \tag{2.9}$$

For a 60^0 dislocation generated by epitaxial growth of a uniform film on a lattice mismatched substrate α is the angle between the plane of growth and Burger's vector, *i.e.* 60^0 and b/b_{eff} = 2. This expression has led to various experimental work that involved growths of different epilayer-substrate scenarios to verify the validity of Matthews' prediction. Before we go into the details of that work, we first would like to discuss the fundamentals of epitaxial growth.

2.1.3 Thermodynamics of two-dimensional epitaxial growth

The pursuit of Moore's law [1.6] for semiconductor miniaturization has driven researchers to explore innovative methods of incorporation of thin-film structures for enhanced optoelectronic performances. Fabrication of such devices demands the incorporation of a dense array of superior quality and narrowly distributed tiny structures within or on the surface of a host material. This requires fabrication techniques that not only are cost and time effective, but also provides atomic reproducibility. Conventionally lithography was time effective however the damage done by the etching dominated the device performance [2.12]. Controlled precipitation has shown simplicity of manufacturing structures up to 4 nm in size but it is not time effective and is limited to the application of thermoelectric or infrared detectors [2.13]. Colloidal methods have been cost and time effective however atomic reproducibility for incorporation of low dimensional structures within a higher band gap matrix is much to be desired [2.14]. For the last few decades the epitaxial growth method has shown considerable success for the growth of low dimensional devices [2.15]. Even though it is not a cost-effective

technique it has consistently shown atomic reproducibility and has exhibited wide applications. Since this project explores thin-film semiconductor structures we adopt an epitaxial growth method.

Epitaxy is a chemical interaction of atoms to be grown with the surface atoms of a heated single crystal or polycrystalline substrate in an ultra-high vacuum chamber (10^{-10} mbar). The material to be grown is (*e.g.*) radiatively heated from an ultra-pure source, stored in a cell, which effuses as an atomic beam flux travelling to the heated substrate. The atoms in the beam interact with the dangling bonds at the heated surface resulting into a hybridization process of atomic bonding that deposits an epilayer with an ordered array of atoms.

In this project such epitaxial growth was conducted using molecular beam epitaxy (MBE). The key feature of MBE is its ability to control deposition growth rates up to one atomic layer (monolayer) making it advantageous over vapor phase and liquid phase epitaxy methods [2.15]. The theory of epitaxial growth has been developed along both a kinetic [2.16 – 2.20] and a thermodynamic [2.21 - 2.25] basis. A thermodynamic approach assigns the real system as a closed system and assumes that any kinetic processes are fast enough to drive the system to equilibrium. Whereas the kinetic approach assumes that the equilibrium state cannot be reached thereby discarding the closed system approach. Shchukin [2.26] stated that although this distinction is oversimplified, if growth interruption or annealing of grown epilayers is introduced then a kinetic model should provide the same result as would a thermodynamic model. In the pursuit of the semiconductor miniaturization, 1990s witnessed an expansion of a range of materials to be grown using MBE. Although for those studies the kinetic approach provided sufficient information for atomically abrupt interfaces, the understanding of this pathway required knowledge of the thermodynamically favorable states. According to Gibbs phase rule the sum of the number of phases (φ) plus the number of degrees of freedom (F) in a system equals the number of components (K) plus the number of parameters (χ) that govern that system. An expression for Gibb's phase rule is [2.27],

$$\varphi + F = K + \chi \tag{2.10}$$

In the epitaxial growth of a binary system, *e.g.* gallium arsenide (GaAs) using MBE, the solid phase is in equilibrium with the gas phase (2 phases), with 2 components and K = 2. Substituting in Eqn. 2.5 gives degrees of freedom as F = 2, *i.e.*, the state of a GaAs epitaxial growth system can be changed by two parameters, *viz.* (i) the pressure of the system, given by the gaseous atomic beam flux, and (ii) the temperature of the system, set by the substrate temperature. During growth of III-V compounds, like GaAs, it is an established fact that group III elements possess a sticking coefficient to the substrate and group V elements do not stick to the substrate in the absence of group III elements [2.28] implying that the atomic beam pressure of gallium governs the pressure component of the GaAs growth system. During deposition of the first layer GaAs atoms are sp^3 hybridized with the underlying surface atoms leading to epitaxy while generating another array of unfilled dangling bonds increasing the surface free energy of GaAs. Under the given film growth conditions GaAs surface atoms either rehybridize or form non-bonding electronic states [2.29] for long range order with low surface energy states. This phenomenon is defined as surface reconstruction. Däweritz [2.30] plotted a surface phase diagram for GaAs MBE growth, Fig. 2.5, with a ratio of arsenic to gallium beam equivalent pressure (BEP) as a function of substrate temperature. Different sections of the phase diagram depict different surface reconstructions named as 4x4, 4x2, 4x1, 3x1, *etc*. Fig. 2.6 shows a typical array of Ga (empty circles) and As (solid circles) in (a) 4x4 and (b) 2x4 reconstructions [2.31]. These different reconstructions are recorded using an *in situ* reflection high energy electron diffraction (RHEED) tool. RHEED creates an electron beam which strikes the sample surface at a very low angle and the electrons are diffracted off of the periodic array of surface atoms satisfying the Laue diffraction condition [2.32]. An interference pattern from diffracted electron beams results in streaks on a phosphor screen resembling the atomic arrangement of the epilayer if the growth front is occurring in a planar or two-dimensional manner. Depending on the substrate temperature and background pressure a 4x4 reconstruction would form a 4x

streak image on a RHEED phosphor screen due to diffractions of the beam at [110] and [-110] azimuths while for a 2x4 surface reconstruction RHEED beam at [110] would result in a 2x streak image while a four-streak image will be captured at [-110] azimuth.

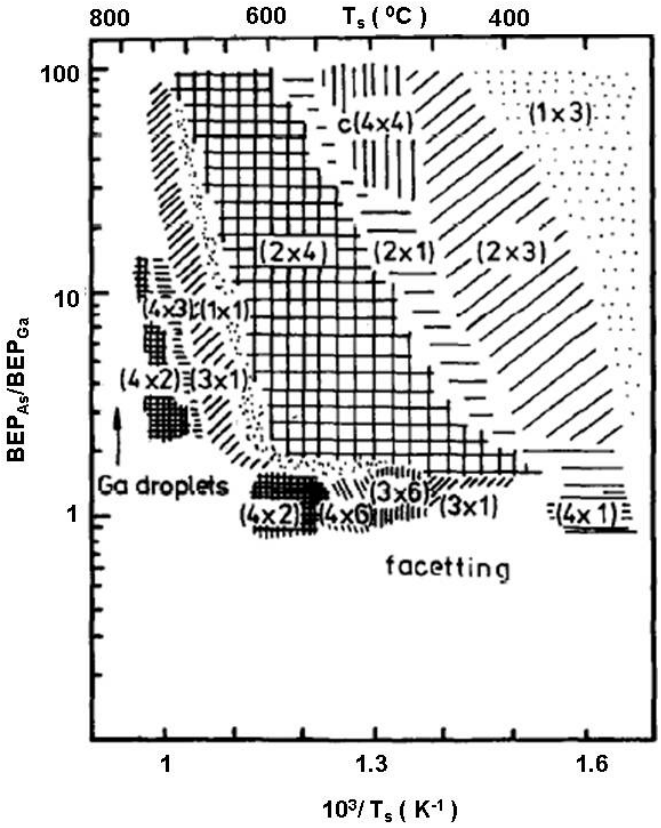

Fig. 2.5 GaAs (001) surface phase diagram [Däweritz, 1990]

Our GaAs buffer layer growths were carried out at substrate temperatures, Ts = 650 ^{0}C and As-Ga BEP ratio of 12, which produced the RHEED images shown in Fig. 2.7. Counting from the center bright spot, the next bright spot appears on the second and the fourth streaks in Fig. 2.7 (a) and (b), respectively. These RHEED images imply a 2x4 epitaxial growth pattern complying with Däweritz' phase diagram for the given combination of flux ratio and the substrate temperature. Streaky RHEED pattern is essential to the growth of uniform epilayers as a proof of uniform surface growths since an uneven surface or an epilayer with a dense array of

dislocations would result in a spotty and/or diffused image. In the event of formation of islands the electron beam will diffract off the island facets, thus forming v-shaped chevron patterns. We discuss these results in Chapter 4.

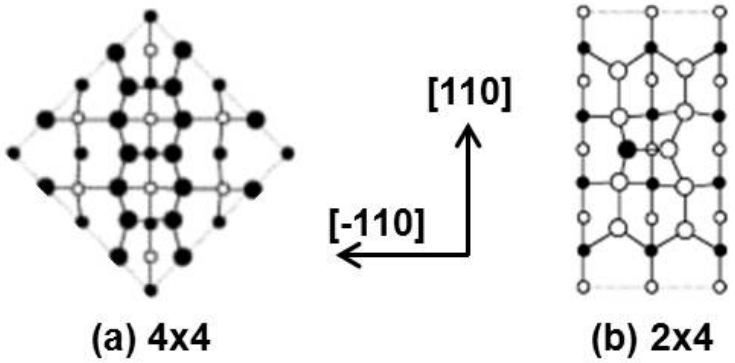

Fig. 2.6 Atomic arrangement of GaAs [Schmidt, 2002]

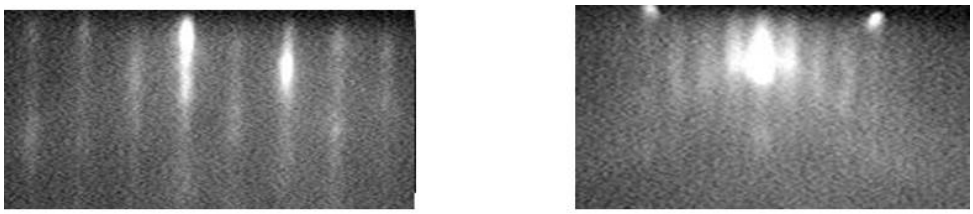

Fig. 2.7 RHEED images captured at 90^0 substrate rotations

2.1.4 Dislocations in semiconductors

Recalling the discussion in Section 2.1.1, Matthews concluded that FVM model overestimated the critical epilayer thickness on the account of strain release mechanism. Matthews theorized [2.9] a four-step mechanism for the generation of dislocations: (1) dislocation already present in the underlying substrate layer overgrows as a threading dislocation in the epilayer, (2) until the thickness of the epilayer (h) is less than certain critical thickness (h_c) threading dislocation continues to grow, (3) once epilayer reaches h_c the dislocation glides because of the force due to strain energy and (4) dislocation glides along the

closed packed plane breaking a series of bonds in the adjacent atoms while forming a misfit dislocation along the interface, see Fig. 2.8 (a). Another mechanism proposed by Matthews called as half-loop nucleation can be seen in Fig. 2.8 (b). Substrate inhomogeneity, such as particulates, impurities and mechanical damage, which exist prior to epitaxial growth, can result in stress concentrations that extend through the epilayer into stress concentration regions at the surface. Matthews proposed [2.33] that a tangle of dislocations forms a half-loop at the surface. The activation energy for the half-loop triggers the loop to break away and glide towards the interface forming a misfit defect. The Ge_xSi_{1-x}/Si systems have been reported with such dislocations nucleation from surface imperfections [2.34]. There has been some visual evidence of gliding of the threading dislocation, in Matthews' first proposed mechanism, but the notion that this mechanism leads into misfit interface dislocation generation is not widely accepted due to lack of evidence. Also this mechanism lacks a theoretical explanation of the strain gradient responsible for gliding towards a specific direction. There is, however, evidence of gliding dislocation interactions [1.2]. Same-sign (with similar group III or group V atom missing in the lattice) 60^0 dislocations with identical Burgers vectors (b_1) may experience repulsion causing the glide mechanism to a halt. Close spacing of two same-sign threading dislocation could form a single etch pit, in etch pit density (EPD) tests [2.35], misleading as a lower EPD than actual, under visible light microscope. On the contrary complementary 60^0 Burgers vectors, b_1 and b_2, can experience strong attraction. This might result in a new threading segment with Burgers vector b_3. In diamond and zinc-blende structure the resulting dislocation is a sessile edge type [2.36, 2.37]. Although this annihilation mechanism reduces the dislocation density by 50%, its sessile nature prevents it from ever exiting the system via glide.

Half-loop nucleation requires pre-requisites such as inhomogeneity, drastic change in the growth mode (roughening instead of smooth 2-dimensional) and cross-contamination in the form of particulates/impurities from the deposition source or the vacuum chamber. Constant evolution of substrate cleaning procedures, purity of sources, slow growth kinetics and

horizontal deposition plane nearly eliminates the possibility of such half-loop nucleation. In summary, both of these dislocation generation mechanisms need stronger theoretical foundations and corresponding evidence. A test of their validity is beyond the scope of this project. Wider acceptance in the literature is for the mechanism of dislocation generation at epi-substrate interface by breaking atomic bonds and we adopt the same as a primary source of dislocations in this project.

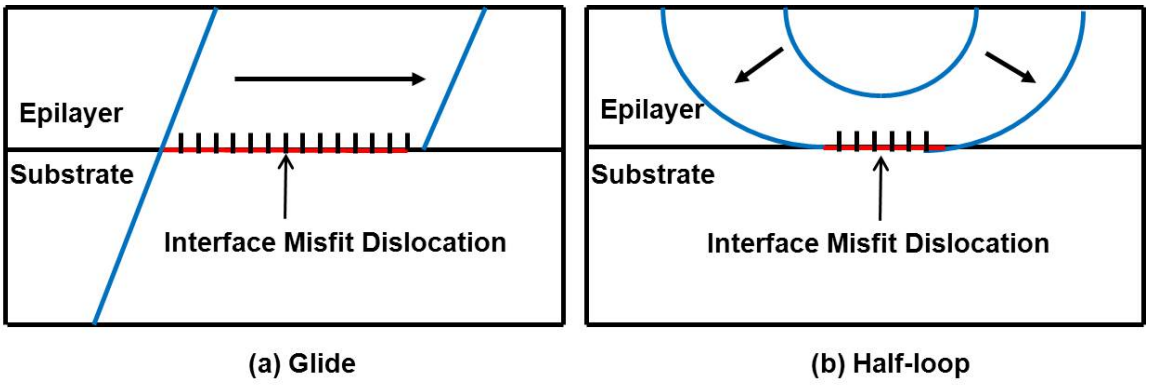

Fig. 2.8 Speculated mechanisms for dislocation generation

2.1.5 Controlling misfit and threading dislocations

It has been noted previously that a lattice-matched system limits the freedom of band gap design for optoelectronic systems while a lattice-mismatched system provides the advantage of the freedom of band gap selection however their epilayer growths are recommended up to the critical thickness proposed by Matthews and Blakeslee's continuum elasticity model. For thicker uniform epilayer growths reduction in the density of dislocations requires special considerations, as follows.

Substrate patterning: This technique requires patterning of the growth substrate to reduce the area of deposition so as to minimize the interactions between gliding dislocations by shortening the length over which a dislocation can glide. Once the threading dislocation continues to glide and reaches the edge of the growth area, it escapes the epilayer and further

release of strain energy becomes harder. Substrate patterning allows for thicker epilayer growths while maintaining low dislocations density [2.38, 2.39]. This technique however suffers from the drawback that patterning reduces the useable area for the desired optoelectronic device.

Strained-layer superlattice (SLS): This method requires deposition of a thin (tens of monolayers) SLS of a semiconductor with a significant lattice mismatch with the underlying substrate. SLS introduces strain to force the glide dislocations already present in the epilayer to the edge of the sample [2.33], thus acting as a dislocation filter. This method suffers from the drawback that induced assistance for gliding invites threading dislocation interactions that unfortunately act as dislocation sources. So far only about a 5-10% reduction in the dislocation density has been reported using the SLS method.

Compositionally-graded structures: This method involves epitaxial deposition of a ternary alloy with compositional grading (CG) at the rate of, say, 10% per μm thickness on a lattice mismatched substrate. Such growths have been reported for Ge_xSi_{1-x} on Si substrates [2.40]. Using CG, thick epilayers can be grown without attaining high residual strain. The epilayer gradually relaxes to the lattice constant of the desired alloy composition providing advantage over abrupt structures. Another advantage is that due to low misfit at each stage of growth only glissile 60^0 dislocations are introduced. However this method isn't devoid of drawbacks either since deposition of thick epilayers with gradually changing band gaps can seriously affect the freedom of optoelectronic design performance. Also thicker layers require long deposition times which degrade fabrication efficiency. Despite these drawbacks it should be noted that compositional grading addresses the core of the issue of dislocation generation, *i.e.*, the amount of lattice misfit. The concept of gradual incorporation of the misfit offers room for improvement for future lattice-mismatched systems, including the experimental work in this project. Before we discuss that issue, we first discuss in the next section the motivation behind using thin-film structures.

2.2 Low Dimensional Semiconductors

2.2.1 Motivation for optoelectronic device research

At absolute zero in temperature a semiconductor has a set of energy bands completely filled called the valence band (VB) and a set of energy bands that are completely empty called the conduction band (CB). The forbidden region of energy levels between the highest occupied and lowest unoccupied bands is referred to as a band gap *Eg* of the semiconductor. Reduction in the size of semiconductors to tens of interatomic spacings significantly changes their electronic properties due to alteration of the density of states (DOS) [2.41]. Density of states is defined as the number of possible electron or hole transition states available per free carrier energy. For a low-dimensional structure a free carrier's de Broglie wavelength competes with the size of the semiconductor introducing a quantum confinement effect. The emergence of this unique physical phenomenon is discussed briefly [2.41].

In solid state physics, for a bulk material the effective-mass model of the quantum mechanical energy of a free electron is given by,

$$E = \frac{\hbar^2 k^2}{2m_e} \tag{2.11}$$

where m_e is the electron effective mass (which is an approximation model of the potential energy environment produced by the surrounding atoms that an electron or hole encounters in a material), k is the wave-vector related to the electron wavelength ($2\pi/\lambda$) and $\hbar$ is the Planck's constant with the quantum mechanical momentum given by $\hbar k$. For a bulk semiconductor the DOS increases as a continuum (parabolic nature) above the band gap, as seen in Fig. 2.9. In the presence of electromagnetic radiation, the absorption of a photon with energy higher than E_g leads to excitation of an electron from the VB to the CB. If the carrier is excited to one of the higher available energy states within the conduction band then it thermalizes to the lowest energy state at the band edge by losing its energy *via* creation of phonons. A similar trend is followed by the hole in the valence band. If the semiconductor is thinned out in one dimension, so much so that the thickness is comparable to the de Broglie wavelength, then the parabolic

nature of the DOS transforms into a step-like trend. This is a result of the reduction in available energy states along the lowest dimension while maintaining a continuum of DOS in the other two dimensions. The process of carrier thermalization is restricted to pre-defined phonon energies available in the thicker dimensions. Due to 1-D confinement the electrons and holes can exist at the same energy sharing a coupling mechanism *viz.* the Coulomb interaction E_{coul}, which binds electrons and holes together forming an exciton. For a thin semiconductor the Coulomb interaction is a maximum at the smallest thickness. Splitting of the DOS continuum into discrete energy bands provides a sharp band-edge followed by continuous available energy states. If the thin semiconductor film is sandwiched between a higher band gap material, then the excited carriers in the film are free to move along the confined regions and are not allowed to leave this region known as a potential energy well. This type of one-dimensional quantum confinement is commonly referred to as a quantum well (QW), see Fig. 2.9, with the corresponding electron energy given by,

$$E_{QW} = \frac{\hbar^2}{2m_e}\left[\pi^2 \frac{{n_x}^2}{{L_x}^2}\right] \tag{2.12}$$

It is evident in Eq. 2.12 that the thickness of a QW, L_x, influences the energy of the free electron excited within. Next, if carriers are confined in two dimensions by forming a semiconductor quantum wire (QWR), then its corresponding DOS is shown in Fig. 2.9. The electron energy with carrier confinement along both x and y directions is given by,

$$E_{QWR} = \frac{\hbar^2}{2m_e}\left[\pi^2 \frac{{n_x}^2}{{L_x}^2} + \pi^2 \frac{{n_y}^2}{{L_y}^2}\right] \tag{2.13}$$

Quantum dots (QD) (nano-sized boxes) exhibit 3 dimensional confinements with discrete energy levels analogous to a single atom with the corresponding electron energy as,

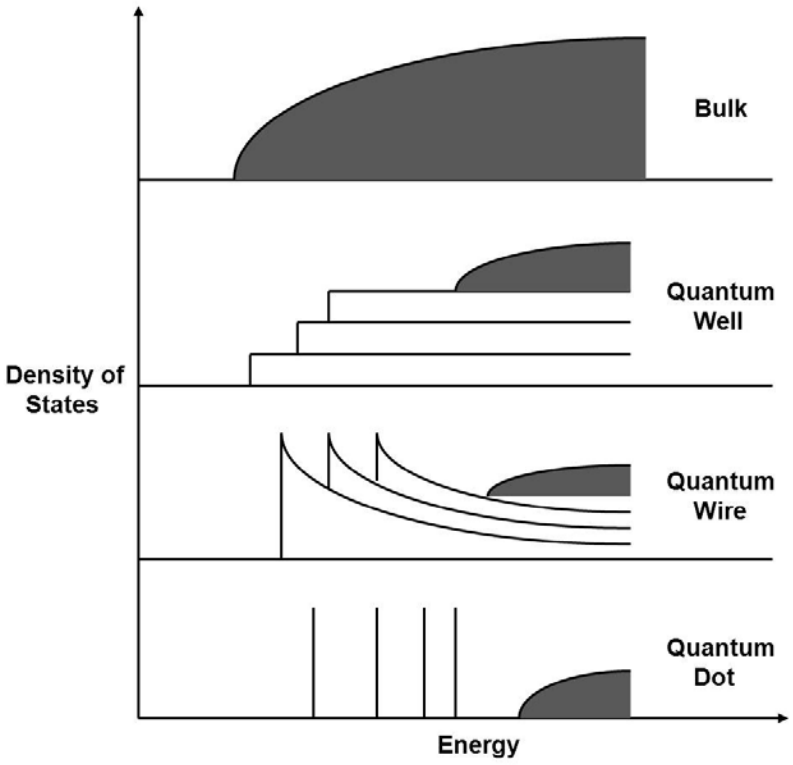

Fig. 2.9 Density of states in 3-D bulk, quantum well, quantum wire, and quantum dot

$$E_{QD} = \frac{\hbar^2}{2m_e}\left[\pi^2 \frac{{n_x}^2}{{L_x}^2} + \pi 2 \frac{{n_y}^2}{{L_y}^2} + \pi^2 \frac{{n_z}^2}{{L_z}^2}\right] \tag{2.14}$$

It is clear from Eqs. 2.12 - 2.14 that by varying the semiconductor dimensions the free electron energy changes. As mentioned before the thermalization of an excited carrier in a QW structure is allowed via a continuum of bands available in 2-dimensions, in a single dimension for a QWR, while within a QD only the phonon-energies matching discrete energy levels are responsible for carrier thermalization. This is called as a phonon-bottleneck effect. Quantum confinement of electrons and holes enhances E_{coul} and stabilize excitons at room temperature; otherwise E_{coul} competes with the thermal energy of the phonons ($k_b \cdot T$) making excitons much more unstable in bulk structures.

Quantum confinement effect has led to the exploitation of low-dimensional semiconductors for various applications with marked improved performance dynamics that otherwise are absent in the bulk semiconductor devices. For example, silver nanometer sized particles incorporated within a telluride glass device improved the second harmonic generation (SHG) for the non-linear optical laser applications [2.42]. Quantum well lasers have exhibited thermal up conversion via anti-stokes phenomena that pertains to emission of higher energy photons than absorbed [2.43]. In a quantum well device the red-shift in the absorption energy as a function of the well width is called the Stark effect and has useful applications in optical fibers [2.44]. Insertion of donor layers within GaAs/AlGaAs quantum well structures in high electron mobility transistors is reported to have reduced the deep donor defects reducing the non-linearity of the device performance at low temperatures [2.45]. Graphene nano ribbons have been manufactured to form a single resonant quantum dot device [2.46]. InGaN/GaN multi quantum well BLUE light emitting diodes have been reported, that show improvement in the internal quantum efficiency *via* low dimensional layer incorporation [2.47]. Single electron transistors with a quantum dot-in-well structure have shown a potential for scalable quantum computing application [2.48]. The band gap tuning ability has led to applications of QDs for infrared photo-detectors [2.49]. Above all, the most interesting works that are pertinent to this project are the application of quantum dots based *p-i-n* diodes as photovoltaic (PV, solar cell) devices by enhancing efficiency *via* wider solar spectrum absorption [2.50].

In spite of the predictions of numerous theoretical proposals, the corresponding experimental results have had difficulty in attaining the expected optoelectronic performances. The difficulties have ranged from aspects of fabrication methods to the reduction of materials defects. In the next section we discuss the thermodynamics of the growth of low-dimensional structures using epitaxial technique and the corresponding strain behavior.

2.2.2 Stranski-Krastanov growth

Stranski-Krastanov (SK) growth is a self-assembly phenomenon employed in the fabrication of nano-meter sized islands by depositing a couple of monolayers of a

semiconductor material with a significant lattice mismatch to the substrate. One such misfit system would involve deposition of InAs (δ_a = 6.058 Å) on GaAs (δ_0 = 5.653 Å) with a total misfit of approx. 7%. The thermodynamics of the island formation are a bit different as compared to uniform film growth with an arsenic background flux, GaAs substrate temperature, and InAs ML content as the primary boundary conditions [2.51], see Fig. 2.10. Due to the high misfit the epilayer lattice undergoes a biaxial strain forming pseudomorphic structure that absorbs strain energy E_ε while the surface energy of the epilayer is denoted as E_{surf}. If E_ε exceeds E_{surf} then

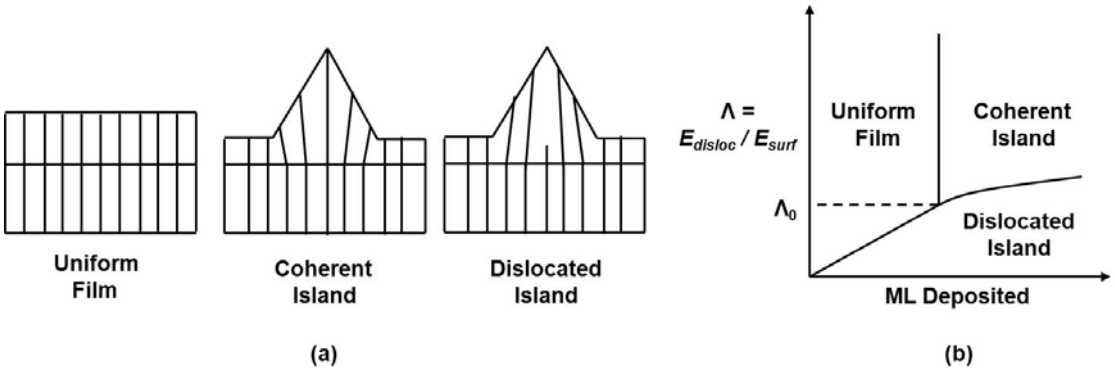

Fig. 2.10 (a) SK mode morphologies, (b) phase diagram for those morphologies [Shchukin, 2004]

the epilayer releases E_ε by relaxation of the peusdomorphic lattice forming an island by self-assembly. This would increase the surface area of the epilayer thereby increasing E_{surf} and hence it competes with the energy of dislocation generation E_{disloc}. A ratio of E_{disloc} to the change in the surface energy ΔE_{surf} defined as Λ is a factor that drives the thermodynamics of 3 different SK growth morphologies, *viz.*, (i) coherent island (CI), (ii) dislocated island (DI), and (iii) uniform film (UF), see Fig. 2.10 (a). A lower Λ ratio results in lower dislocation formation energy, thus favoring dislocated island formation whereas a higher ratio with the deposition of the right amount of material (critical ML thickness) will result in a coherent island. Less than critical ML content will result in uniform film morphology without sufficient strain energy to form islands. A more direct kinetic approach for synthesizing coherent islands with strain decay

within an island as the lattice constant varies from the top of the island to the wetting layer is discussed in the next section.

2.2.3 Strain and the kinetics of coherent island fabrication

Ratsch and Zangwill (RZ) [2.52] theoretically connected the previously mentioned 3 types of morphologies in the SK growth mode to the misfit and the number of atoms deposited using the same one-dimensional atomic chain model proposed by Frenkel and Kontorova (recall Section 2.1.1). In accordance with Niedermayer [2.53] RZ assumed that the lateral strain relief of an atomic chain in the p^{th} layer deposited on a substrate with a lattice constant δ_0 is achieved at the free ends of that chain by arranging atoms in a non-uniform spacing with an average lattice constant δ_p. The atoms in the layer p, eventually, project a rigid sinusoidal potential for the atoms in the next deposition layer, p+1 so that lateral relaxation from the p^{th} layer propagates to the top of the film. Ratsch [2.52] modified the expression (2.3) to account for finite length of an atomic chain as follows,

$$U = W\ell_0^2 \sum_{n=1}^{N-1} \left[\xi(n+1) - \xi(n) - f\right]^2 + \frac{1}{2} W \sum_{n=1}^{N} \left[1 - \cos 2\pi\xi(n)\right] \tag{2.15}$$

where ξ_n is the displacement of the n^{th} atom of the chain, ℓ_0 is a material parameter defined in terms of the spring constant μ and sinusoidal substrate potential, $W/2$, as $\sqrt{\mu a_0^2 / 2W}$. N is the number of atoms in the epilayer and f is the misfit. Ratsch used an average lattice constant of the p^{th} layer as expressed by,

$$\delta_p = \delta_{p-1}\left(1 + \frac{\xi_p(N_p) - \xi_p(1)}{N_p - 1}\right) \tag{2.16}$$

where N_p is the number of atoms in p^{th} layer and the misfit in that layer, $f_p = \dfrac{b - \delta_{p-1}}{\delta_{p-1}}$. Ratsch assumed rectangular morphology for an island by vertically stacking h linear chains with the island sidewalls forming single crystallographic facets without any overhangs. According to Ratsch for such morphology the total relaxed island energy is given by,

$$E_R = \sum_{p=1}^{h} \left(N_p, \delta_{p-1} \right) \tag{2.17}$$

This relaxed island energy counts misfit-induced contributions. To estimate the total energy of a coherent island E_{tot}, Ratsch added $-E_{bond}$ for every saturated bulk bond and a term $-\frac{1}{2} E_{dimer}$ for every exposed surface atom. Hence the total island energy of a coherent island becomes,

$$E_{tot} = E_R - \sum_{p=1}^{h} \left(4N_p + 2 \right) E_{bond} + \frac{1}{2} h E_{dimer} \tag{2.18}$$

where h denotes the total number of double layers (one atom). Using values for a typical semiconductor Ratsch generated a misfit *vs*. number of atoms plot, shown in Fig. 2.11, with congruous results noticed previously in Fig. 2.10 (b). For less than 2% of misfit the epitaxial deposition grows as a uniform film; whereas for a 2 to 6% misfit and a moderate amount of epilayer the deposition forms a coherent island and for large misfits and thicker monolayer depositions the SK mode results into a dislocated island. Although Ratsch and coworkers introduced the kinetics responsible for SK island morphologies, an even more direct kinetic interpretation was given by Pintus [2.55] and later by Snyder [2.56]. They introduced the concept of diffusion length as,

$$L = \sqrt{D\tau} \tag{2.19}$$

where D is the surface diffusivity and τ is the time to deposit monolayer. Atoms with diffusion lengths on the order of tens of nanometers across the surface of the substrate are available to form any of the three SK morphologies so that the total amount of material, in 2 dimensions, is $L \cdot t$, where t is the thickness of the film, and it replaces the term for the number of atoms on the x-axis of Fig. 2.11. Intuitively, small sized islands should possess coherency with the underlying substrate. Experimental evidence supporting this theory was presented by Shchukin and Ledenstov and is briefly discussed in the next section.

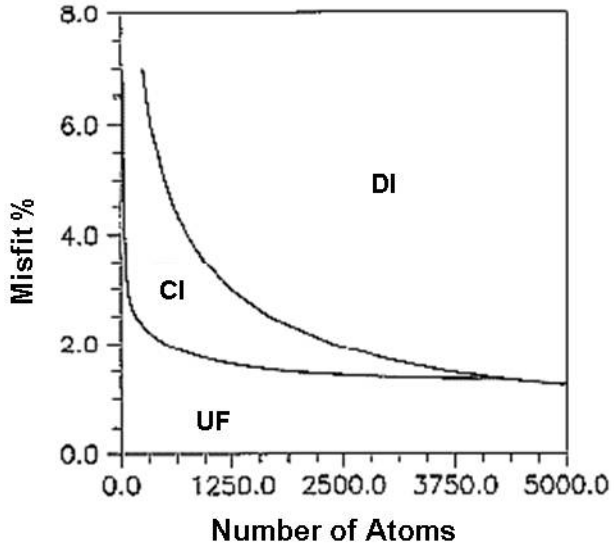

Fig. 2.11 SK morphologies as a function of misfit and epitaxial deposition content [Ratsch, 1993]

2.2.4 Attempts at fabrication of coherent islands

InAs/GaAs low dimensional semiconductor growth systems have been extensively studied for both kinetic and thermodynamic effects in the pursuit of narrowly distributed high density island morphologies. Primarily, four factors have been realized that affect epitaxial island growth.

A. Substrate temperature: Shchukin [2.56] and Ledenstov [2.57] deposited 3 ML of InAs on a semi-insulating GaAs substrate followed by capping the bare islands by deposition of a 10 nm GaAs layer to preserve island shapes. Growths were carried out at various substrate temperatures and the corresponding capped island samples were characterized using TEM. The results revealed a trend in the reduction of the QD density, but an incremental increase in their lateral size as the substrate temperature increased. Both Shchukin and Ledenstov's kinetic models predicted

increased adatom diffusion coefficients, which are responsible for reduced diffusion barriers with increasing temperature.

B. Arsenic background pressure: Ledenstov [2.58] studied the effects of the As flux on the InAs island growths by depositing 4 ML of InAs at a 480 ^{0}C substrate temperature at various As background fluxes. He observed 25 nm sized islands at a density of 5 x 10^{10} cm^{-2} for a 2 x 10^{6} torr As background equivalent pressure (BEP). An increase in the As BEP by a factor of 3 reduced the density of the 25 nm sized islands; however, a larger density of 50 to 100 nm sized islands was produced. A further increase in the As BEP by a factor of 5 nearly suppressed the formation of any islands. A dense array of 3-D islands underwent a reversible transformation into a planar morphology when the As BEP was reduced to 1/6th of the optimum growth condition. The higher As BEP accelerated the migration of the adatoms to deliver material over a distance of more than 0.2 nm forming dislocated islands by a process called Ostwald ripening; whereas for a low As BEP there was insufficient flux to form the InAs dimers, which reduced the ML deposition, and hence resulted in uniform film growth. On the other hand and optimum As BEP maintained the adatom diffusion length at just the right value to allow growth of narrowly distributed high density InAs QDs.

C. Monolayer content: In all of the previously mentioned work of Ledenstov and Shchukin they noted a morphological transition from uniform film to coherent island formation by the SK mode strain release mechanism at a deposition of 1.7 ML of InAs. Further increases in depositions, up to 4 ML, increased the island sizes, however the density was reduced. Even further increase in ML deposition eventually led to coalescence of the large islands into a dislocated uniform film.

D. Growth interruption: This stage is marked by the deposition of the islands followed by a short period of growth interruption, *i.e.* holding the sample at the growth temperature for some time under As flux alone. Ledenstov and Shchukin identified an interplay between the ML content and the growth interruption when 14 nm sized InAs islands were fabricated in three ways: (a) 3 ML of deposition followed by 10 sec of growth interruption, (b) 40 sec growth interruption after 2.5 ML deposition and (c) combination of 2 ML deposition and 100 sec interruption. Too long of an interruption led to an evaporation of the In atoms from the substrate, an In/Ga interdiffusion, which formed ternary alloys within the islands as a wetting layer, and finally it caused defects to migrate from the interface to the epilayer surface.

Epitaxial kinetics of narrowly distributed, high density, coherent InAs islands have been established in the literature, and we also in our own work have observed similar trends in the kinetic factors that affect island growths, which will be discussed in detail in Chapter 4. In the next section, we briefly outline the strain decay phenomenon within low-dimensional structures and its effects on optoelectronic performance.

2.2.5 Strain decay within quantum dots

Strain profiling of the InAs QDs deposited on a GaAs substrate has been performed by Lin *et al.* [2.59] for a system consisting of pyramidal shaped islands, a wetting layer, and a capping layer as shown in Fig. 2.12. Lin adopted a valence force field model [2.60, 2.61] to describe the microscopic elastic energy of the atoms in the islands [2.59] as given by,

$$U = \frac{1}{4}\sum_i \left[\sum_j \frac{3}{4}\alpha_{ij} \frac{\left(r_{ij}.r_{ij} - d_{ij}^2\right)^2}{} \right] + \frac{1}{2}\sum_i \left[\sum_j \sum_{k\neq j} \frac{3}{4}\beta_{ijk} \frac{\left(r_{ij}.r_{ik} + \frac{d_{ij}.d_{ik}}{3} \right)^2}{d_{ij}d_{ik}} \right] \qquad (2.20)$$

where i represents the i^{th} atomic site with j and k as the nearest neighbor sites; r_{ij} and d_{ij} denote a vector and the atomic bond length, respectively, from the i^{th} atom to its j^{th} neighbor and α_{ij} and β_{ijk} are the bond stretching and bending constants, respectively.

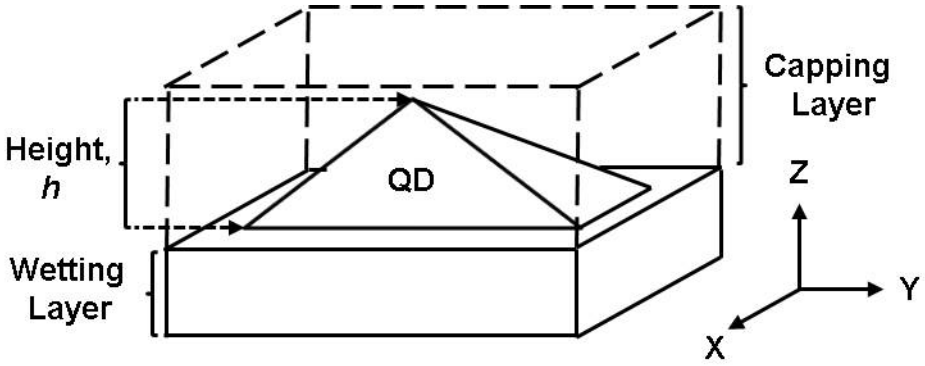

Fig. 2.12 Schematic representation of a quantum dot with wetting and capping layers.

Substituting bond stretching constants for GaAs and InAs as 41.19 N/m and 35.18 N/m, respectively, while bond bending constants as 8.95 N/m and 5.5 N/m for GaAs and InAs, respectively into Eq. 2.20; Lin plotted strain energy per atom of an uncapped InAs QD grown on the GaAs substrate as a function of the dot height, see Fig. 2.13. It is evident from Fig 2.13 that the strain energy per atom reduces as the dot height increases from 50 to 60 Å, but it increases with further increase in the height, thus showing a minimum in strain energy at a dot height of 59 Å, as verified experimentally by Krishna [2.62]. Fig 2.13 also shows that the electron-heavy hole transition energies, $E_1^e - E_1^{hh}$, as calculated using the eight-band k·p model, suggests a narrowing of the electron-hole wave function with taller islands. These results also suggested that a dot height of ~ 60 Å formed relaxed islands; however, no claim regarding coherency or dislocated morphology were made.

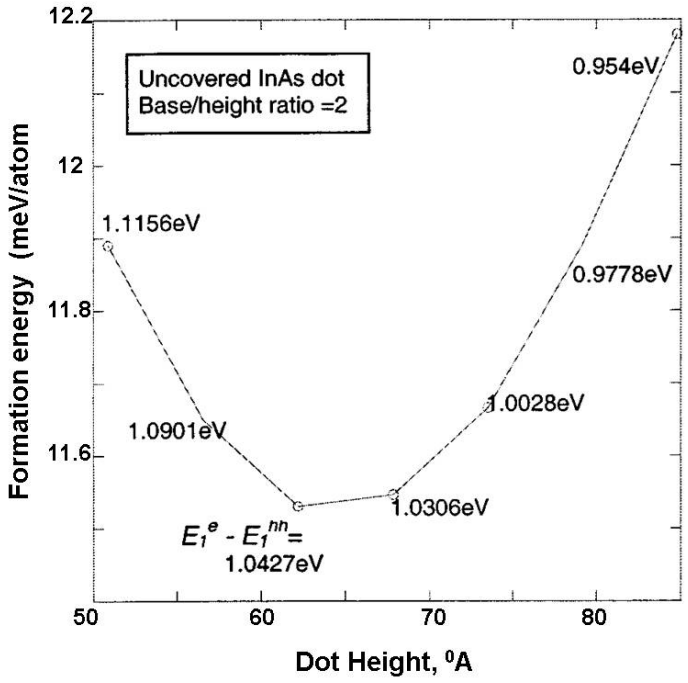

Fig. 2.13 Strain energy per atom as a function of the dot height along with the intersubband optical transition energies [Lin, 2002]

The effect of a capping layer on the strain decay within a quantum dot was assessed by Tomić by utilizing a strain tensor component [2.63] expressed as,

$$\varepsilon_{ij}(r) = \frac{(2\pi)^3}{L_x L_y L_z} \sum_{n_x,n_y,n_z} \varepsilon_{ij}(\xi_n) \exp(i\xi_n r) \tag{2.21}$$

where L_x, L_y, *and* L_z *are* the dimension of the island, in the *x*, *y*, and *z* directions respectively, *and n* is the summation index, while ξ_n represents the plane wave basis in real space (*r*). According to Tomić, the strain state of a system consisting of a QD and a capping layer grown on a substrate is affected by three main components of the strain tensor, *viz*. (i) biaxial strain, $\varepsilon_{bx} = \varepsilon_{zz} - \frac{\varepsilon_{xx} + \varepsilon_{yy}}{2}$, (ii) hydrostatic strain, $\varepsilon_{hy} = \varepsilon_{xx} + \varepsilon_{yy} + \varepsilon_{zz}$, and (iii) a strain component in the x-direction, ε_{xx}, in (101) plane. A graphical representation of all of the three components as a function of the dot size is shown in Fig. 2.14. The hydrostatic strain is

confined within the QDs and the wetting layer with slightly lower penetration depth compared to ε_{xx} into the surrounding matrix. The biaxial strain is positive inside the islands while the matrix exhibits a negative strain, suggesting a higher strain component in the *x* and *y* directions compared to the *z* direction. This biaxial strain gradient between the island and the matrix is highest at the top of the QD and is responsible for material intermixing to form a truncated pyramid, as suggested by Lin. Moreover the wetting layer and the QDs lose any sharp edges due to the lattice mismatch and the differences in the bond strengths between GaAs and InAs. Tomić' further simulated a second ML deposition step on top of the first GaAs cap showing a vertical stacking of islands, which suggested a strain driven placement of the islands in the second layer directly on top of the first. This theory has been verified experimentally in another work [2.64] that showed cross-sectional TEM images of a systematic stacking of QDs. Such vertical stacking has motivated low dimensional semiconductor devices to be fabricated as quantized structures sandwiched between layers of a higher band gap matrix for various optoelectronic applications. One of those applications is a photovoltaic device to achieve more photon absorption over a wider portion of the solar spectrum for enhanced power conversion efficiency. In the next section we will briefly discuss the physics of a solar cell and will briefly introduce the issue of strain and dislocations formed in thin-film devices.

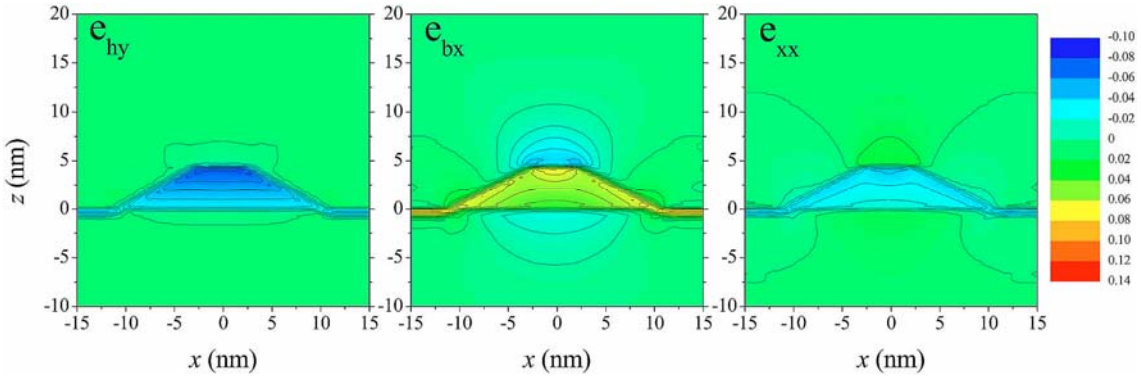

Fig. 2.14 Graphical representation of the hydrostatic, biaxial and a strain component in the *x*-direction for an *x*-*z* plane at *y* = 0 [Tomić, 2006]

2.3 The *p-i-n* Diode Structure for Photovoltaic Applications

2.3.1 Junction behavior

One of a semiconductors' primary property is its band gap energy E_g, which is the absence of electron energy levels between a top-most electron filled band and the bottom-most of an empty band, called valence and conduction bands respectively. A *p*-doped semiconductor has an added impurity that provides extra holes as the majority carriers making the semiconductor as an acceptor while an *n*-doped semiconductor consists of a donor impurity that has extra electrons as the majority carries. If *p*- and *n*-doped semiconductors are brought into physical contact atomically then there will be an exchange of carriers from each side until an equilibrium point is reached where the total carrier movement from the *p* side equals the *n* side forming a *p-n* junction with a depletion layer of no carriers formed between the *n* and *p* sides. If in addition, another layer of intentionally un-doped semiconductor (intrinsic) is sandwiched between the *p* and *n*-regions, then it forms a *p-i-n* diode, see Fig. 2.15, which is a slightly more complex but modified version of the standard *p-n* diode junction.

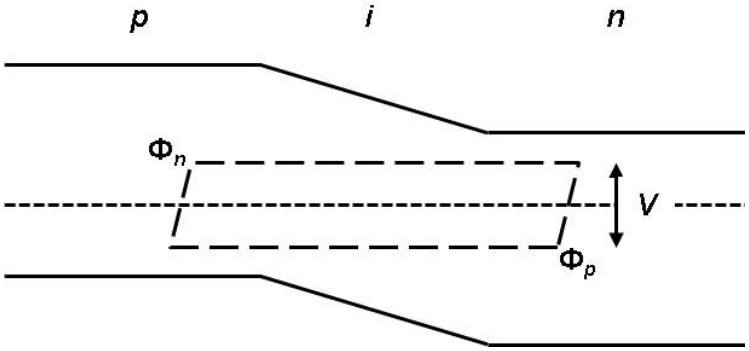

Fig. 2.15, Band diagram of a *p-i-n* diode shown with an applied voltage *V* that separates the quasi-Fermi levels ϕ_n and ϕ_p.

The solid lines show the valence and conduction bands, forming a junction in the middle, with a dotted straight line in the middle as the intrinsic potential (Ψ) of the diode, being constant at equilibrium. With zero bias between the *p* and *n* terminals the net generation of the current is equal to the net recombination, which is zero. The application of a forward bias will

inject carriers into the junction diffusing electrons and holes to *p* and *n* region respectively as applied bias splits the quasi-Fermi levels of electrons (ϕ_n) and holes (ϕ_p). This causes a net recombination across the junction producing a forward current. Under ideal conditions, the separation between the quasi-Fermi levels is equal to the applied bias *V*. The electron (*n*) and hole (*p*) carrier densities are given by,

$$n = n_i e^{q\frac{(\psi-\phi_n)}{kT}} \tag{2.22}$$

$$p = n_i e^{q\frac{(\phi_p-\psi)}{kT}} \tag{2.23}$$

where n_i is the intrinsic carrier density [2.65, 2.66]. Under ideal condition the applied bias induces radiative recombination across the junction which equates the current driven into the diode. If *B* is the radiative recombination coefficient then the rate of the radiative recombination, U_{rad}, is given by,

$$U_{rad} = B \cdot n \cdot p \tag{2.24}$$

Eq. 2.24 leads to the Shockley equation [2.67] for the radiative current J_{rad}, *viz.*

$$J_{rad} = J_0\left[e^{\frac{qV}{kT}} - 1\right] \tag{2.25}$$

where J_0 is the reverse saturation current. Impurity states such as a dislocation can trap carriers, resulting in the non-radiative Shockley-Hall-Read recombination (SHR) process. The trap-assisted net recombination rate U_{SHR} for the SHR process is given by Eq. 2.26, in which τ_n and τ_p are the electron and hole lifetimes respectively, and n_t and p_t are equilibrium populations of the occupied electron and hole trap states respectively.

$$U_{SHR} = \frac{np - n_i^2}{\tau_n(p + p_t) + \tau_p(n + n_t)} \tag{2.26}$$

U_{SHR} leads to the following current relation [2.68],

$$J_{SHR} = \frac{qn_i W}{\sqrt{\tau_n \tau_p}} \left(e^{\frac{qV}{2kT}} - 1 \right) \tag{2.27}$$

where W is the space charge width. J_{SHR} and J_{rad} together form the dark current (current under applied bias without any illumination on the device) as given by,

$$J_{dark} = J_0 e^{\frac{qV}{nkT}} \tag{2.28}$$

where n is the ideality factor for a device. For n values close to 1, a device is radiatively dominated while a device that is non-radiatively dominated results in higher values of n. Under illumination conditions photons are absorbed in the junction by exciting carriers across the band gap. The equilibrium values of the n and p carriers are raised and the quasi-Fermi levels split. The electric field across the junction splits e-h pairs by driving minority carriers across the junction creating a reverse current in the cell. The overall current-voltage response is approximated as the sum of the short-circuit photocurrent J_{sc}, and J_{dark}. J_{sc} is the current induced by an illuminated cell voltage. If a forward bias is applied on the illuminated device, which causes J_{dark} to equal J_{sc}, then the net current is zero and the applied voltage is called the open circuit voltage V_{oc}. This is called the superposition approximation as given by Eq. 2.29 [2.69]. In this project the superposition is assumed to hold true and is used to estimate the V_{oc} of the p-i-n devices we fabricated using thin-film structures with the intrinsic embedded regions. Details of these results are outlined in Chapter 6.

$$J_{dark}(V_{oc}) = J_{sc} \tag{2.29}$$

2.3.2 Strain behavior in the intrinsic region

Low-dimensional structures that are lattice mismatched to a matrix/substrate have been explored extensively for photovoltaic applications within the last two decades [2.50, 2.70]. In the pursuit of obtaining more absorption of the solar spectrum so as to surpass the Shockley-Queisser single band gap efficiency limit [2.71], two prominent theories have been introduced for devices with quantum confined structures, *viz.* (a) sub-band gap photon absorption using an

intermediate band-gap [2.72] and (b) multi-exciton generation [2.73]. These theories suggest that a *p-i-n* diode design that incorporates low-dimensional structures within a higher band gap matrix would allow the low-dimensional structures to absorb lower energy photons while the higher band gap material absorbs higher energy photons. The theoretical advantage of such structures is to allow an added contribution to the current being generated by lower energy photons, which are generally absent in single band gap structures, to the total photocurrent emanating from the device. From previous discussions it could be deduced that the lattice mismatched intrinsic regions will store the misfit strain up to a critical thickness and will release it once the strain energy E_ε exceeds the dislocation generation energy E_d. The generation of dislocations within the intrinsic region would be detrimental since they will act as non-radiative traps for the excited electrons and holes and thereby increase the dark current.

Recently a method, called as strain balancing (SB) or strain compensation (SC), has been introduced as a means of controlling the build-up of strain energy within the intrinsic region [2.74]. SB consists of epitaxial growth of a stack of alternate layers of higher and lower lattice constant semiconductors that would exhibit an average lattice constant <δ> similar to the underlying substrate. Ekins-Daukes formulated an expression [2.75] for <δ> using the zero-stress method, which is given by,

$$\langle\delta\rangle = \frac{A_1 t_1 \delta_1 \delta_2^2 + A_2 t_{21} \delta_2 \delta_1^2}{A_1 t_1 \delta_2^2 + A_1 t_1 \delta_2^2} \tag{2.30}$$

where suffixes 1 and 2 belong to each alternate layers, t is the thickness of the layer, A is an elastic parameter = $C_{11} + C_{12} - \frac{2C_{12}^2}{C_{11}}$ and δ is the lattice constant. By selecting a lattice constant with a corresponding thickness, the average lattice constant of the intrinsic region can effectively match the substrate lattice constant and thus in principle reduce dislocations. This method has been shown to be successful [2.76] to the extent of generating higher J_{sc} compared to a *p-n* control device without any intrinsic layers. However, the growth of SB stacks

unfortunately generated dislocations that increased the dark current as shown in Fig. 2.16. This result subsequently lowered the V_{oc} when compared to a control device. Fig. 2.16 depicts the I-V characteristics under dark conditions for (a) an InGaAs QW based *p-i-n* structure [2.74] and (b) an InAs QD based *p-i-n* diode [2.76], grown epitaxially on a GaAs substrate. In both of the plots, the curves at highest bias with lower dark current belong to the GaAs *p-n* control device and the curves at lowest bias belong to the *p-i-n* structures without any strain compensated intrinsic regions. We note that with the minimization of the average lattice constant by depositing strain balanced layers, the SB device in both cases exhibited reduced dark current as compared to the relaxed devices, but they also produce a higher dark current than the control device, as shown by curves at intermediate bias. Strain balancing, as mentioned previously, has been effective to the extent of enhancing J_{sc}, but unfortunately V_{oc} and consequently the solar cell power efficiency wind up being reduced in the final outcome. Even with the introduction of zero-stress criteria and the extension of the continuum elasticity theory in formulating the thickness of the SB layer [2.77], the central point of uncertainty brought about by the strain balancing approach is that the anisotropy of the quantum dot island shapes and sizes remain an unsolved problem. Also, the QDs are separated by strained wetting layers with a lattice constant that imposes some misfit in the SB layers. In addition, the threading of a dislocation from the substrate into an epilayer alters the strain profile around a dislocation site and thus further enhances the anisotropy. On the other hand a very important aspect to note about the strain within a QD is the decay of its strain to a strain free lattice at the top of the island. This aspect therefore serves a source for a unique strain gradient between the island and the surrounding capping layer that drives the In-Ga interdiffusion to form a truncated pyramid [2.59]. We will elaborate further on this observation in later chapters, and show how we have used it to improve device performance. The strain balanced layers mentioned in the above publications consisted of alloys like GaP [2.76] or GaAsN [2.78] that had a lower lattice constant than the GaAs substrate to compensate for the higher lattice constant of InAs. Unfortunately GaP or GaAsN layers further increase a strain gradient that is responsible for the

In-Ga inter-diffusion phenomenon. Pre-assessment of all of these factors prior to the deposition of SB layers is very difficult and brings about much uncertainty in using the SB method effectively. In this project we report an improved method for controlling the strain built-up within a *p-i-n* diode structure, as discussed in the next section.

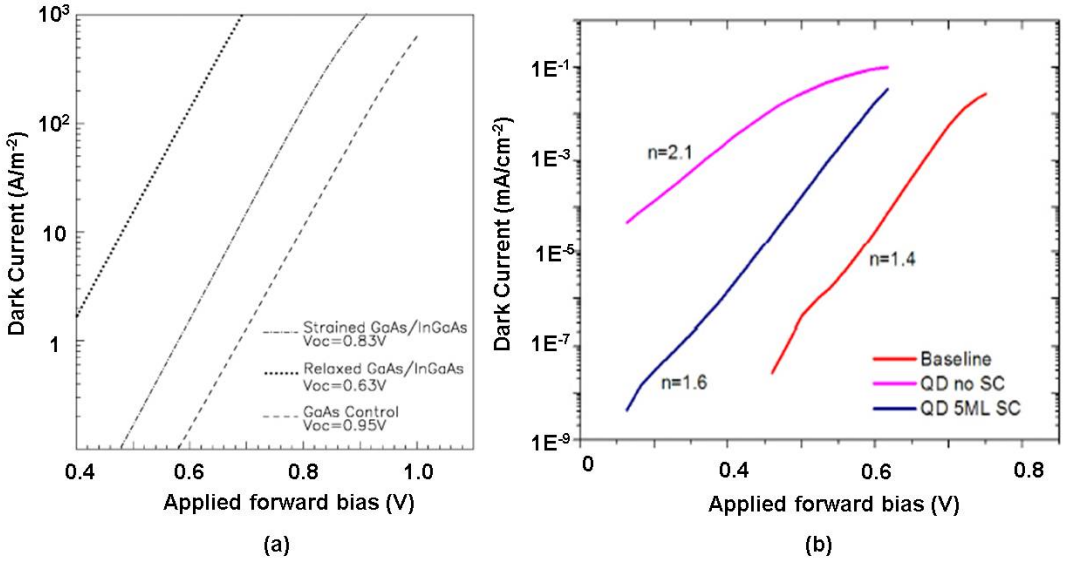

Fig. 2.16 Dark current reduction by inclusion of strained intrinsic region of lattice mismatched (a) quantum wells [Ekins-Daukes, 2001] and (b) quantum dots [Hubbard, 2008]

2.4 An Innovative Epitaxial Growth Approach to Minimize Dislocations in Lattice Mismatched Devices

Recalling discussions in 2.1.5, the method of patterning the substrates to reduce the distance over which a gliding dislocation can travel before it escapes at the device edge minimizes the possibility of dislocation interactions, and thereby reduces defects. However this method restricts the active device area, and hence makes it unsuitable for solar cell applications where the goal is to employ maximum possible operable area to generate the highest possible free carrier density. As mentioned previously strained layer superlattices incorporate high misfit strain at an early stage of the device growth, and thereby assist threading dislocation to escape via a glide mechanism; however, this method invites added dislocation interactions that can and most likely will generate sessile edge-type defects. Strain compensation by deposition of

alternate tensile-compressive layer deposition seems, at this point of time, to have reached an end [2.79]. Compositional grading of a buffer layer gradually decreases the strain between the substrate and the intrinsic region; however, this method suffers from thick buffer layer growths, which are usually unsuitable for many band gap engineering applications. On the other hand, it does deal with the issue of dislocation formation at a fundamental level, which is accommodating the amount of misfit. Our innovation, however, is to incorporate a buffer layer with an intermediate lattice constant between the substrate and an intrinsic quantum-dot region to reduce the total misfit between the two regions without any compositional grading. Although this seems to be counter intuitive, our results show something quite the contrary!

Consider a scenario of epitaxial growth of an InAs QD layer on a GaAs substrate. Let us assume that 2 ML of InAs is deposited so that it releases the interfacial strain by forming self-assembled islands and is later capped by a GaAs layer. These two steps can be repeated as many times as needed depending on the targeted structure. Also assume all of the islands possess a coherent morphology with a uniform height of 50 Å (where the effective thickness t_1 of the island is 25 Å due to the pyramidal shape) with a lattice constant of the unstrained bulk InAs (δ_1 = 6.0533 Å) and a wetting layer that is 30 Å thick (t_2) with lattice constant, δ_2 = 5.8533 Å (average of InAs and GaAs). The GaAs capping layer will be strained to the same lattice constant δ_2 as the wetting layer with a thickness t_3 = 50 Å. After capping, each intrinsic layer becomes 80 Å thick with no truncation of the islands. Using the average lattice method [2.74] the average lattice constant of one intrinsic layer will be,

$$\langle \delta \rangle = \frac{\delta_1 t_1 + \delta_2 t_2 + \delta_2 t_3}{t_1 + t_2 + t_3} = \frac{(6.0533 \times 25) + 5.8533(50 + 30)}{50 + 30 + 25} = 5.91 \text{ Å}$$

The average indium fraction for this lattice is 0.65 and the total misfit f between this intrinsic layer and the GaAs substrate is 0.045. Matthews altered the elastic fraction expression, Eq. 2.8, to suit multilayer growth as,

$$\varepsilon = \frac{b(1 - \nu \cos^2 \alpha)}{\pi h (1 + \nu) \cos \lambda} \left(\ln \frac{h}{b} + 1 \right) \tag{2.31}$$

From Adachi [2.3] we find for the $In_{0.65}Ga_{0.35}As$ ternary alloy that v = 0.34, cosα = cosλ = ½, and b = 4 Å. The elastic strain decay within the intrinsic region can be plotted as a function of the epilayer thickness, see the solid curve in Fig. 2.17. Up to an elastic fraction of 1 the stored strain energy E_ε does not exceed the dislocation formation energy E_d, thus absorbing the entire misfit elastically, *i.e.* $f = \varepsilon$. Beyond the critical thickness h_c of 190 Å (less than 3 intrinsic layers of the GaAs/InAs deposition on the GaAs substrate) the value of ε falls below 1. When E_ε exceeds E_d, dislocations form. Up to ε = 1 the strain decays rapidly while beyond h_c the rate of the strain decay is slower since breaking of one atomic bond (when an atom residing at the interface absorbs the maximum elastic strain) and reduces E_ε by a certain amount and creates a new threshold E_ε for the cessation of the next atomic bond. To a certain extent, this semi-periodic strain release mechanism mode slows down the strain decay as is evident in Fig. 2.17. Beyond h_c the total misfit in the system is absorbed both elastically and plastically forming biaxially strained pseudomophic layers (Fig. 2.4) with higher and lower lattice constants, respectively. Now consider the incorporation of a buffer layer of $In_{0.25}Ga_{0.75}As$ with a lattice constant of 5.755 Å sandwiched between the intrinsic region and the GaAs substrate. The total misfit between the buffer layer and the intrinsic layer will now be 0.027. The elastic strain decay curve for this arrangement is the dotted curve in Fig. 2.17, which shows a higher critical thickness of 360 Å for the intrinsic region. It is evident that the incorporation of a buffer layer in between the GaAs substrate and the intrinsic region will not trigger dislocation generation until the deposition of the 5th intrinsic layer which previously was the 3rd layer if it had grown directly on top of the GaAs substrate.

At this point the obvious question to ask is wouldn't the incorporation of an intrinsic layer increase the total misfit between the tandem intrinsic-buffer epilayer combination and the GaAs substrate, as compared to a buffer layer-GaAs substrate combination only?

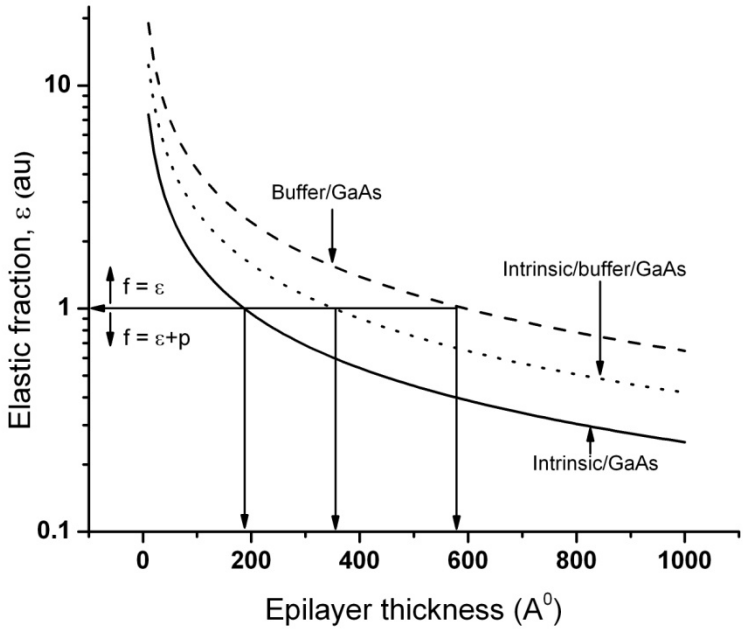

Fig. 2.17 Elastic strain decay *vs.* epilayer thickness showing the critical thickness h_c, using the Matthews-Blakeslee model for different epilayer-substrate combinations.

Theoretically, the answer would be yes. Which leads to the next question, which is would this not generate more dislocations because of the greater misfit? Surprisingly, our results indicate that the lattice mismatched buffer layer releases the misfit strain only if it exceeds the critical thickness (dashed line in Fig. 2.17) during deposition. Once the growth kinetics are adjusted for the intrinsic layer deposition then the buffer layer itself acts as a new effective substrate in which the misfit between the intrinsic region and the buffer layer, not the GaAs substrate, sets a new threshold for the generation of dislocations within the intrinsic region. The realization that a new growth mechanism might be possible began when we analyzed experimental evidence that showed a lower dark current in a *p-i-n* device with an intrinsic region as compared to a control homojunction cell without an intrinsic region. This unexpected behavior was discovered during the course of this work and led us to analyze the two different devices using x-ray diffraction, high-resolution transmission electron microscopy, and current-voltage measurements to extend

our understanding of the strain control and release mechanism, and to conceive a new growth method that minimizes the generation of dislocations. These results and the analysis will be discussed in greater detail in Chapter 5.

CHAPTER 3

MATERIALS SYNTHESIS, DEVICE FABRICATION AND CHARACTERIZATION TECHNIQUES

The goal of this research work was to produce strain engineered indium arsenide quantum dot based *p-i-n* diode structures. In order to produce as dislocation free devices as possible with reduced leakage current density and improved optoelectronic performance in the near-to-long infrared region, a series of materials synthesis by deposition, device fabrication and characterization techniques were employed. For a better understanding all of the tools described in this Chapter they are categorized into three sections, *viz*: Materials Synthesis (Section 3.1), Device Fabrication (Section 3.2), and Materials and Device Characterization (Section 3.3).

Figs. 3.1 (a) and (b) show the schematic structure of the target devices synthesized in this study: (a) quantum dot (*p-i-n*) and (b) homojunction (*p-n*) diode structures.

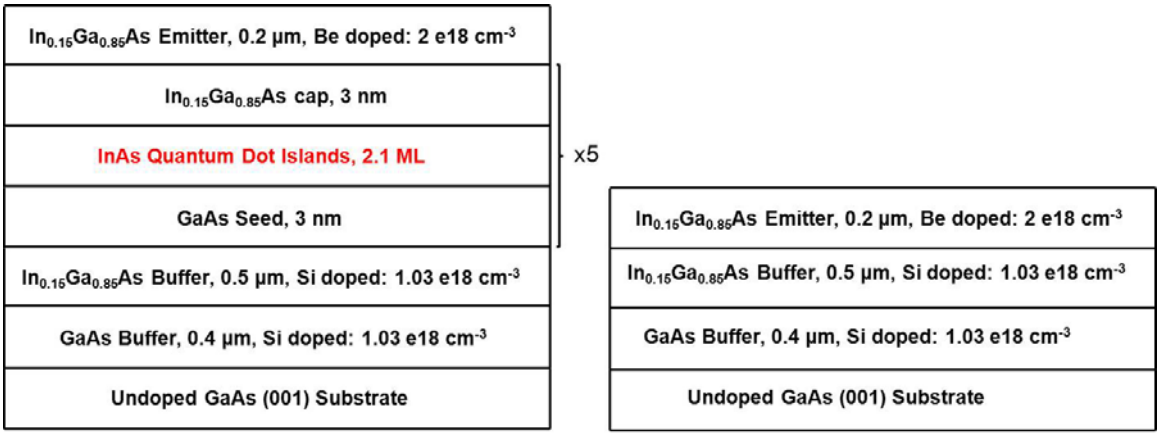

Fig. 3.1 (a) Quantum dot device, (b) Homojunction device

Each device layer shown in Fig. 3.1 was grown using the molecular beam epitaxy (MBE) method in Professor Wiley Kirk's laboratory to gain maximum possible reproducibility of the film quality, which was especially critical for the intrinsic quantum dot (QD) region growths. Intrinsic QD region consisted of the gallium arsenide (GaAs) seed layer, indium arsenide (InAs) quantum dot layer and indium gallium arsenide (InGaAs) cap layer, sandwiched between *p* and *n* doped InGaAs emitter and base layers, respectively. The homojunction device was same as the QD device except for the absence of the intrinsic QD region.

Two types of layer structures were grown for the purpose of establishing a characterization baseline:

1. InGaAs base layer growths with varying indium arsenide fractions were grown on top of GaAs substrates to provide lattice constant and defect generation mechanism analysis
2. Single layer uncapped indium arsenide layers were deposited on top of InGaAs base layers to analyze the kinetics of QD formation

Samples with the 1st type of layer structures were characterized using reflection high energy electron diffraction (RHEED), x-ray diffraction (XRD), secondary electron microscopy (SEM), and profilometry; whereas samples synthesized as the 2nd type of layer growths were primarily characterized using atomic force microscopy (AFM). Those two types of initial growths and their corresponding characterization results provided data for optimized growth of the intended *p-i-n* diode structures which were further characterized using high-resolution transmission electron microscopy (HRTEM), to record visual evidence of dislocations, if any, as a result of lattice strain, and photoluminescence (PL) to record band gap and other optoelectronic properties of the base, emitter and intrinsic regions. Additional, diode structures were fabricated into 500 μm x 500 μm MESA structures using photolithographic and semiconducting processing techniques, followed by platinum deposition as metal contacts for current-voltage measurements. More details about all of the device fabrication and characterization techniques utilized in this research will be explained in the next two sections.

3.1 Materials Synthesis

3.1.1 Substrate cleaning

All the devices used in this work were grown on 2" gallium arsenide (GaAs) wafers with (100) orientation, 0^0 offcut (± 0.5^0), undoped (resistivity ~ 3 to 4 x 10^7 ohm·cm) and etch pit density ~ 2000 to 3000 cm^{-2}. Each wafer was cleaved into 4 equal pieces using a wafer scribe. The wafer cleaning process, as described and patented by Cho [3.1, 3.2] and later discussed by Contour [3.3], was adopted as the pre-cleaning step for the cleaved samples. The first cleaning step involved degreasing by submerging the cleaved pieces in boiling trichloroethylene (TCE) for 1 min followed by methanol and de-ionized (DI) water rinsing for 30 sec each, repeated three times. The next step involved etching the wafer by submerging it in boiling 20% hydrochloric acid (HCl) solution for 1 min, followed by a DI rinse. The following step consisted of etching the wafer in a H_2SO_4 solution (H_2SO_4:H_2O_2:H_2O :: 8:1:1) carried out at 48 ^{0}C for 1 min followed by rinsing in DI. The final step was a repeat of the HCl cleaning step. Both the HCl cleaning and H_2SO_4 etching steps were done to remove native oxides, however no other passivation method was used before deposition. The reason behind this procedure was that the final deoxidation step was carried out *in situ* in the growth chamber of theMBE reactor by heating the substrate and blowing off any remaining oxides and thus leaving the surface as pristine as possible with bare dangling bonds.

3.1.2 Molecular beam epitaxy

As discussed in chapter 2, MBE is a technique for growing atomic layers of inorganic semiconductors on a heated substrate using atomic/molecular gas flux beams. Fig. 3.2 shows a schematic arrangement of the basic components of a MBE system, which in our case was a VG80H MBE commercial reactor apparatus. The MBE tool employed for our growths used condensed phase, solid, sources for deposition of III-V materials. The ultra-high vacuum (UHV), chamber was maintained at 10^{-10} mbar to minimize the influence of residual gases, *viz.* adsorbed on interior surfaces during air exposure, dissolved gases within the MBE construction materials and high vapor pressure materials with poor thermal and/or chemical stability. To

maintain UHV conditions a combination of vacuum pumping systems was employed. The primary pumping system consisted of an ion pump and a Ti sublimation pump to achieve UHV conditions and a cryo pump to achieve and maintain growth conditions. Starting at atmospheric pressure a series of three different pumping stages was used to achieve UHV conditions. First a cryo-absorber pump collected residual gases via a gettering mechanism that trapped gases on cold Zeolite surfaces inside the pump. The next stage involved removing gases at sub atmospheric pressures using an oil free turbo molecular pump that was backed at 10^{-3} mbar using a mechanical rotatory pump. To achieve a high quality vacuum under growth conditions and to minimize cross contamination from reflection of gas molecules from interior walls when multiple K-cell fluxes where in operation a set of liquid nitrogen cryopanels were employed inside the main growth chamber. The N_2 cryopanels lined the growth chamber with suitable apertures to allow access of components and substrate holders, etc. Deposition was achieved using high purity solid source materials located in Knudsen effusion cells (K-cells). The K-cells were constructed of tantalum and ceramic materials with the resistive wire heating elements powered by Eurotherm model 905 heater controllers configured in a PID temperature controlled feedback circuit using thermocouple K-type temperature sensors mounted at the base of a crucible holding a charge of a very pure element (99.99995 % purity) such as Ga, In, or As. The crucible was the central component of the K-cells and in the case of these experiments it was made of pyrolytic boron nitride shaped in a long conical configuration with the wide mouth pointing at the sample substrate and rounded narrow end of the cone in contact with the thermocouple temperature sensor. The entire K-cell was surrounded with a water cooling jacket to help block any radiative heat load on the liquid nitrogen shrouds in the MBE growth chamber and also to help stabilize the temperature. The tantalum heating elements provided radiative heating of the deposition materials, over an operating temperature range of 200-1400 ^{0}C, suitable for III-V materials. Beam fluxes from the K-cells were controlled by solenoid operated shutters which along with slow deposition rates rendered atomic reproducibility and rapid changes of composition and doping requirements. A Bayard-Alpert type ion gauge was

installed to allow monitoring the beam equivalent pressure (BEP) of the effusion cells. To minimize stray deposition from chamber walls and shutters, the deposition plane was constructed horizontally such that the growth front remained nearly vertical to the K-cell openings. The substrate holder was connected to a vacuum feedthrough drive shaft and motor assembly that allowed rotation of the substrate to help ensure uniform film growth thicknesses. Radiant heating was used to heat the substrate which also included a radiation reflector to maintain uniform heating. However due to substrate installation and rotation requirements the radiant filament was not in direct contact with the substrate and hence limited the substrate temperature accuracy to within ± 25 ^{0}C of the intended temperature. An important characterization device of the MBE system was a Reflection High Energy Electron Diffraction (RHEED) tool for *in situ* growth monitoring. Details of this instrument are discussed in section *3.3.1*. The deposition chamber was connected via in-line gate valve to a sample preparation chamber (not shown in the figure) for substrate loading, storage, and for maintaining higher quality UHV conditions in the growth chamber.

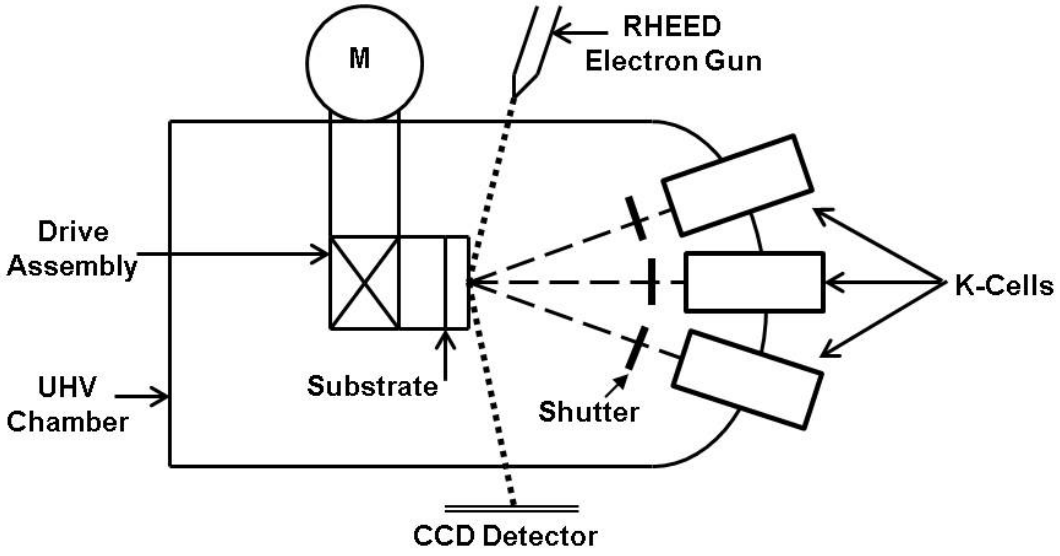

Fig. 3.2 Schematic of primary components of an MBE

3.1.3 Preliminary growths

The first few growth attempts were limited to GaAs buffer layers and InGaAs base layers on GaAs substrates to analyze and optimize the deposition kinetics. InGaAs base layer growths were varied for indium content by changing the In/Ga BEP ratio. Following each InGaAs base layer growth the corresponding In BEP was kept constant in order to deposit a single layer of InAs for island formation, which were left uncapped for characterization. At the end of these preliminary growths certain aspects of intended epitaxy were accomplished, which were as follows.

- The maintaining of high arsenic background pressure at all times to replenish As atoms being desorbed from the substrate surface. A III-V BEP ratio (As:In+Ga) of more than 10 resulted in smooth growth patterns, which were recorded as streaks on the RHEED screen, while a smaller ratio resulted in a spotty pattern, suggesting an uneven or non-planar growth process.
- As a result of lower sticking coefficient for indium atoms as compared to gallium atoms the In-Ga BEP ratio of approx. 0.2 (samples: Z665, Z680) resulted in an indium fraction of 0.15 for the InGaAs base layer, as indicated by x-ray diffraction measurements and the Bragg diffraction condition. X-ray results along with thickness measurements using profilometry were used to calculate deposition rates of the InAs and GaAs layers.
- The InGaAs buffer layer growths were usually followed by the deposition of a single InAs monolayer (ML), (Z665, Z669, Z677-Z680, Z690). A large lattice misfit (>7%) between the InAs ML and the GaAs seed layer was sufficient to initiate the Stranski-Krastanov strain release mechanism to form InAs islands that were recorded as triangular shaped or chevron RHEED patterns.
- A III-V BEP ratio of 17 (Z680) was found to be optimum for the deposition of high density (2.52×10^{10} per cm^2) InAs QDs with a narrow size distribution (32-

39 nm, Bohr atomic radius = 38 nm) and narrow height variation (7 ± 1 nm). This was attributed to reduction in the indium adatom diffusion length, hence producing a uniformly thick epilayer. With a uniform epilayer the misfit strain expanded evenly and initiated the SK mode mechanism within a very narrow time span over the entire surface. This effect helped reduce structural inconsistency among the islands and thus resulted in a narrow distribution of dot sizes.

- A III-V BEP ratio of 17, and a InAs ML deposition growth rate of about 0.05 ML/sec (total 2.1 ML) proved to be the best growth condition for the synthesis of high-density, narrowly distributed islands (Z677-Z680). The characteristic RHEED chevrons appeared at approx. 1.8 ML for the InAs deposition and became sharper for rest of the growth. At higher deposition rates (0.12 ML/sec) the RHEED chevrons were absent probably because of insufficient time for atom rearrangement during the SK growth process. Also more than 4 ML of InAs deposition resulted in streaky RHEED patterns, suggesting that uniform two-dimensional (2D) film growth took place as a result of coalescence of large islands into a continuous film.

All of these results are discussed in greater detail in Chapter 4 using data provided by RHEED, AFM, SEM, TEM and profilometer characterization measurements. The aforementioned preliminary growths served as a basis for the final *p-i-n* diode growths that will be discussed in the next section.

3.1.4 Diode structure growths

After pre-cleaning using the method described in *3.1.1 a* cleaved GaAs substrate was loaded onto the MBE sample holder. Using radiative heating the substrate was heated to 300 ^{0}C to carry out a water desorption step for 15 min followed by deoxidation step at 660 ^{0}C for 15 min. During deoxidation the As K-cell shutter was opened to replenish the substrate surface with As atoms marking the emergence of 2x4 surface reconstructions, as observed from the

RHEED patterns. First, the *n*-doped (silicon) GaAs buffer layer was deposited at a substrate temperature of 600 ^{0}C with the silicon doping K-cell at 1050^0 C. This resulted in a doping concentration of approximately 1.03 × 10^{18} per cm^{-3} as determined by post growth Hall measurements. Next a 0.4 μm thick GaAs buffer layer was deposited at a rate of 1.25 Å per sec. Next, the substrate temperature was reduced to 450^0 C to grow an $In_{0.14}Ga_{0.86}As$ (*n*-doped, silicon K-cell temperature unchanged) base layer by opening the In K-cell shutter along with the Ga source to deposit 0.5 μm of InGaAs at the rate of 1.55 Å per sec.

The intrinsic QD layers were grown in 3 steps with the substrate held at 530 ^{0}C, *viz.*: (1) 3 nm of un-doped GaAs as the seed growth layer, (2) a 2.1 ML of un-doped InAs growth at the rate of 0.05 ML/sec and finally (3) a 3 nm growth of un-doped $In_{0.14}Ga_{0.86}As$ as the cap layer. The first and third steps above were followed by 5 min of annealing; whereas the QDs formed during step 2 via Stranski-Krastanov growth mode were annealed for 2 minutes to provide sufficient time for adatom surface diffusion and atomic rearrangement. The final step of the *p-i-n* diode growth was the deposition of a 0.2 μm thick $In_{0.14}Ga_{0.86}As$ top emitter layer, the *p*-doping was done using a beryllium K-cell at 750^0 C and at a substrate of 450^0 C for a duration of 30 minutes. The As K-cell shutter was kept open throughout the entire growth process.

3.2 Device Fabrication

Photolithography was conducted in the NanoFAB facility at UTA, to fabricate *p*-i-*n* devices from the epitaxially grown samples that were characterized by current-voltage measurements. First, the epitaxially grown samples were cut into approximately 1 cm x 1 cm size pieces and cleaned using methanol and de-ionized water, and finally blow dried using nitrogen gas. Photoresist AZ 5214 was spun on the sample surface using a PWM32-PS-R790 spinneret, at 3000 rpm for 30 sec, see Fig 3.3 (a). The coated sample was pre-baked at 90 ^{0}C for 60 sec on Signatone hotplate. Next, an OAI-Model 860 aligner was used to perform ultraviolet (UV) exposure of the spin coated sample to transfer a MESA pattern of pre-designed mask. The printed on glass photo-mask MESA pattern consisted of square and rectangular features with sizes from 100 μm to up to 1 mm in which 500 x 500 μm^2 features were selected

as device sizes for photovoltaic applications. The UV exposure was carried out for 9 seconds followed by a 45 sec developer step by submerging the coated/exposed sample in a 300 MIF developer solution. Once the pattern was formed the sample was post-baked for 15 seconds at 140 ^{0}C using a hotplate. The thickness of the resist was measured using a KLA-Tencor Alpha-Step IQ profilometer. Patterned samples were then etched using a H_3PO_4:H_2O_2:H_2O :: 3:1:25 solution at the rate of 0.1 μm/min for about 5 minutes to form MESAs, as shown in Fig. 3.3 (b). The resist layer left at the top of the etched MESAs was cleaned using acetone, methanol and DI water. The height of the etched MESAs was measured by profilometry and recorded in the lab notebook.

To form square openings for the metal contact depositions on the etched MESA structures a negative lithography step was used. First, the etched sample was spin coated with AZ 5214 at 4000 rpm for 30 seconds followed by a pre-bake step at 90^0 C for 60 sec on a hotplate. The etched MESAs were then aligned with a METAL mask. The METAL mask had solid square features printed onto a glass plate, which when aligned with the etched MESAs provided openings for the metal deposition. Following the METAL mask alignment was a 6 sec UV exposure. This lithography procedure would usually require a negative resist but the AZ 5214 was little more versatile. After the 6 sec exposure, cross-linking of the exposed AZ 5214, which was the entire resist layer except the unexposed METAL pattern, was executed by post-baking at 115 ^{0}C for 60 sec. Then the sample was flood exposed to UV light for 96 sec causing the previously unexposed METAL pattern to be soluble in 300 MIF [3.4]. Once the sample was developed using the 300 MIF solution, the soluble METAL pattern was washed away leaving behind small openings on the top and square rings around the MESAs while the rest of the sample was covered with AZ 5214, see Fig. 3.3 (c). Next platinum metal deposition using a standard sputtering technique was conducted, which covered the entire sample. The final procedure was a lift-off step to remove unneeded Pt by submerging the sample in acetone which dissolved the AZ 5214 with the unneeded Pt on its top surface and left behind the Pt contacts in the desired locations on top and around the MESAs, as shown in Fig. 3.3 (d). The

samples were then annealed at 150 ^{0}C for 30 sec using a JetFirst 150 Rapid Thermal Anneal system to ensure that ohmic contacts were formed.

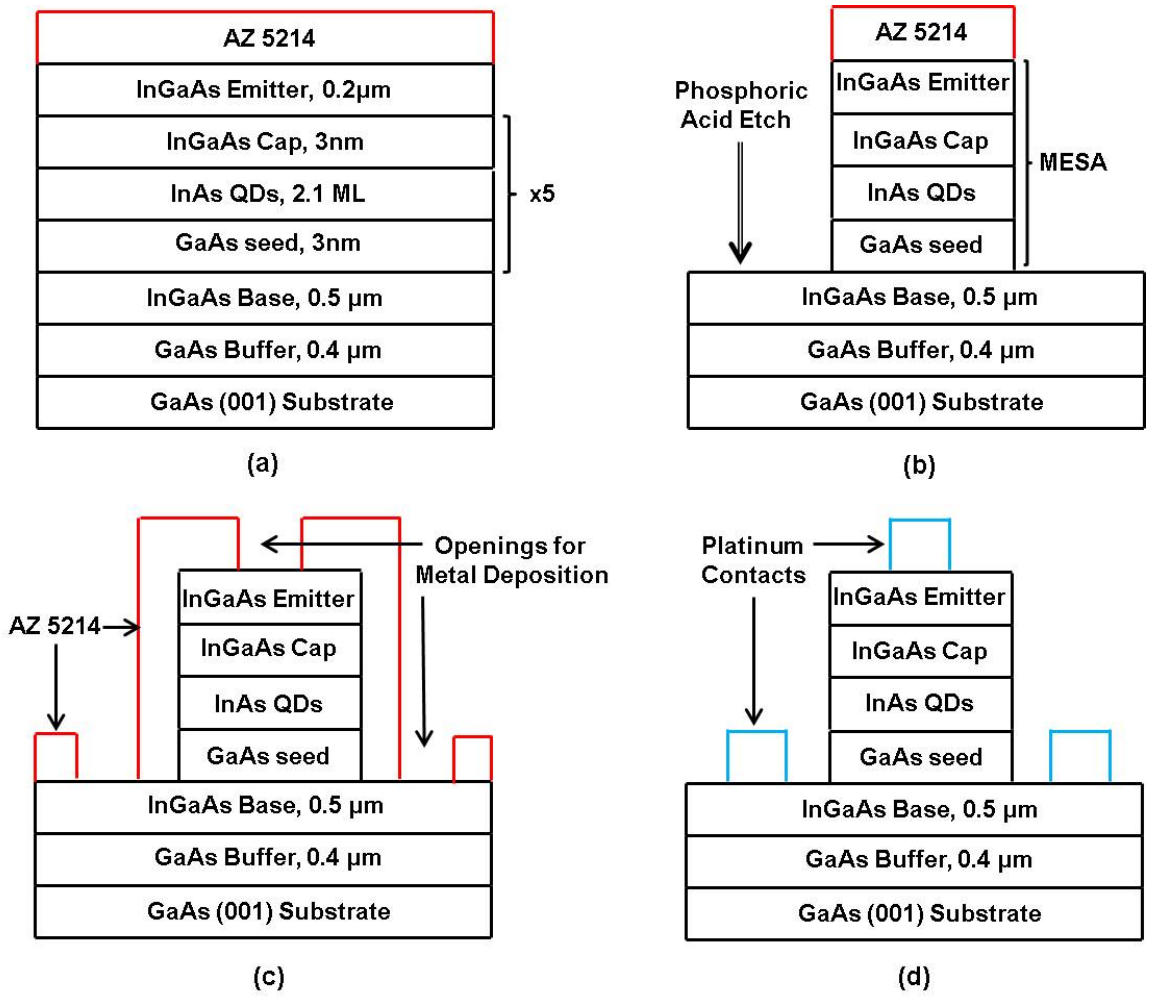

Fig. 3.3 Device fabrication, (a) spin coating AZ 5214 for MESA patterning, (b) etched MESAs using phosphoric acid, (c) the AZ 5214 negative lithographic step, (d) after platinum deposition by sputtering and the lift-off step.

3.3 Materials and Device Characterization

3.3.1. Reflection high energy electron diffraction (RHEED)

Fig. 3.4 shows a schematic of the RHEED analysis tool, which was used *in situ* during epitaxial growths. A tungsten filament based electron gun with a high-voltage bias was used to generate an electron beam with a 10 keV potential that impinged onto the growth front at a

small grazing angle. Because of the very low incident angle the electron beam penetrated only a few angstroms at most into the growth layer.

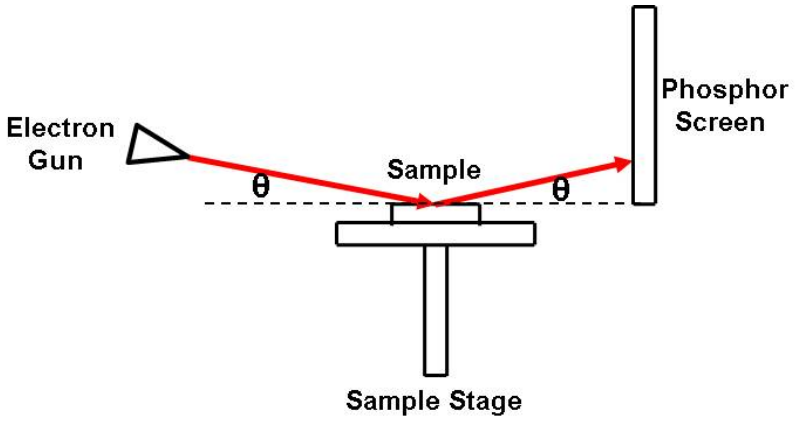

Fig. 3.4. RHEED apparatus

The periodic arrangement of the atoms at the growth front generated a Laue diffraction condition so that the reflected electron beam underwent constructive and destructive wave interference effects in the form of streaky and spotty patterns on a phosphor screen fluorescing as green light. These patterns were recorded using a CCD camera. Although bright streaks were a result of a smooth, two-dimensional growth front, triangular shaped chevron streaks were also observed as a result of diffraction effects from the uncapped InAs islands formed during the SK growth mode as discussed in detail in Chapter 4.

3.3.2. X-ray diffraction

X-ray diffraction characterization was carried out on grown samples using a Siemens D500 x-ray diffractometer residing in UTA's Characterization Center for Materials and Biology. The setup of the diffractometer is shown in Fig. 3.5. The sample was mounted using play-doh onto a sample holder, which was then placed on a sample spinner. The X-ray source (Cu-K) generated a monochromatic beam which scattered off the periodic array of atoms and satisfied the Bragg diffraction condition for the (004) set of planes [3.5].

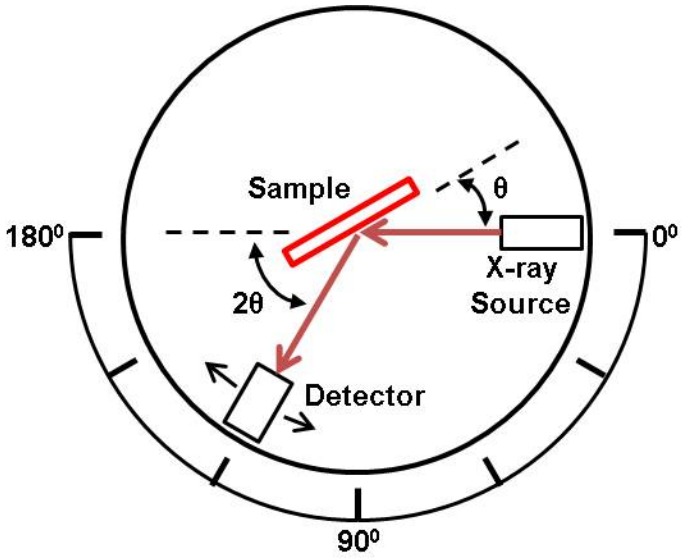

Fig. 3.5, X-ray diffractometer at the θ-2θ Bragg condition

Constructive and destructive wave interference of the diffracted beams was measured with a detector satisfying the θ-2θ Bragg condition as shown in Fig. 3.5. Depending on the indium content in the base and emitter layers of the InGaAs, the lattice constant was altered and this caused the corresponding 2θ reading of the detector to change. The Siemens D500 tool was computer controlled using a Windows based multiple document interface (MDI) software that allowed easy accessibility for executing tasks ranging from experimental setup to data plotting and analysis. It also included a database comprised of the structural properties of a wide variety of materials, which could be compared with measured 2θ vs. intensity plots.

3.3.3. Secondary electron microscopy (SEM) and energy dispersive x-ray (EDX)

The SEM tool, model ZEISS Supra 55 VP, is located in the NanoFAB center at UTA. As a non-destructive imaging technique it was used to do high resolution surface characterization of the grown samples. The SEM setup consisted of an electron gun to generate a beam by thermionic emission, which scattered inelastically with the sample's surface atoms to generate secondary electrons. Depending on the atomic constituents making up the surface, the secondary electrons were emitted over a range of energies and thus served as a

source of different energy charges that were picked up by an electron detector to create contrast images of the surface. About 5 to 10 kV of electron acceleration potential was sufficient to provide up to 10 nm of resolution. However the SEM did not create sufficient contrast to image the uncapped InAs quantum dot samples we grew because the secondary electron energies generated by the InAs islands were to close in energy with the surrounding InAs wetting layer. Hence, the main purpose of the SEM characterization was to display any surface defects undetected by optical microscopy. The ZEISS Supra 55 VP was also equipped with a Genesis 4000 XMS detector which allowed energy dispersive elemental analysis of the uncapped quantum dot layers. This analysis formed the basis for determining the extent of any In-Ga inter-diffusion observed in our samples, [3.6] as discussed in Chapter 4.

3.3.4. Atomic Force Microscopy (AFM)

Fig. 3.6 shows a typical AFM setup. The one employed for this project was a Digital Instruments Dimension 5000 scanning probe microscope located in the NanoFAB Center at UTA. This AFM tool consisted of a silicon nitride cantilever beam, with a sharp tip at the end that had curvature on the order of few nanometers. It was designed to oscillate close to its natural mechanical resonance frequency. A beam from a solid state laser diode reflected off of the oscillating cantilever beam and was detected by a position sensitive split photodiode detector. Depending on the vertical displacement of the cantilever, when probing an uneven sample surface, the photodiode sensors detected a difference in the output signal thus serving as a contrasting source to create an image. For the characterization of the uncapped InAs quantum dot samples we used a scan size of 500 x 500 nm, a height detection limit of 10 nm, an integral gain of 0.4, and a proportional gain of 0.6 to produc acceptable AFM images. The AFM's resolution was comparable to the SEM but the AFM's tapping mode technique provided far better contrast for the QD imaging.

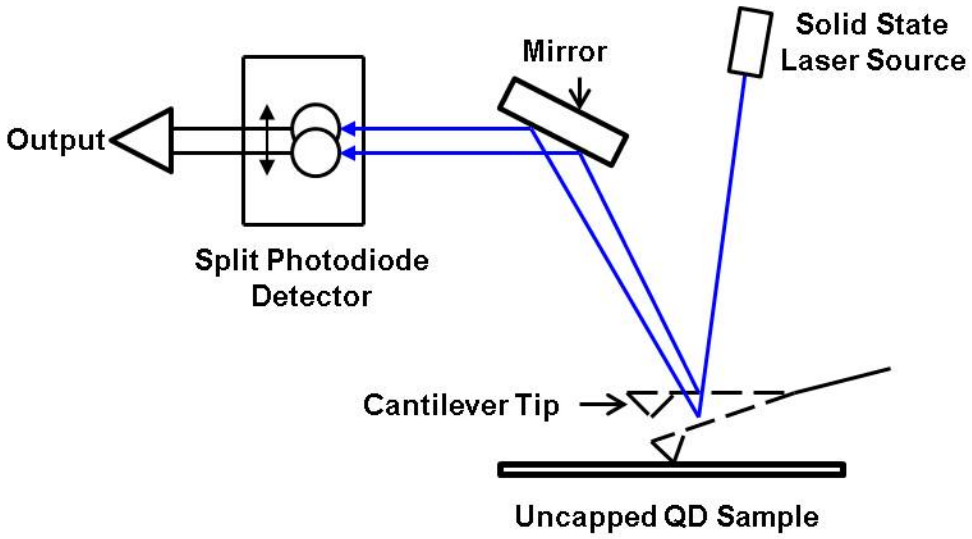

Fig. 3.6 Atomic force microscopy

3.3.5 Photoluminescence (PL) spectroscopy

PL experiments were carried out in the Department of Physics at UT Dallas under the supervision of Dr. Anton Malko and his Research Associates. The samples were cooled to 6K using liquid helium in a cryogenic chamber to slow down phonon contributions to the PL spectra. An Ar^+ laser set at a frequency of about 735 nm was used to excite carrier electrons out of the InGaAs and GaAs valence bands. A 0.22 m grating monochromator utilizing a 1200 grooves/mm diffraction grating was used to select different photon energies emitted from the excited carriers in the samples. Both a germanium detector with a wavelength detection range up to 1100 nm and an InAs detector with a detection range between 1100 and 1600 nm were employed to characterize photons generated by radiative recombination of the excited carriers. The typical setup for the low temperature PL instrumentation is shown in Fig. 3.7.

3.3.6 High-resolution transmission electron microscopy (HRTEM)

HRTEM sample preparation and imaging were carried out by Dr. Choong-un Kim and Dr. Cheolwoong Yang at the Department of Advanced Materials Science and Engineering, Sungkyunkwan University, Republic of Korea. The HRTEM sample was first mechanically

polished down to a thickness of about 50 μm and then mounted horizontally on a half-grid and later inserted into a focused ion beam (FIB) milling machine. Top-down milling was then carried out to form a 'H-block' sample with the electron transparent region perpendicular to epitaxial growth direction. The milled sample was then mounted in the HRTEM sample holder that was then inserted in the column of the HRTEM, which used a field-emission gun and accelerating electrodes to generate an electron beam of 200 keV. As a result of Laue diffraction conditions, the electrons scattered off of the atomic planes to form cross-sectional bright field and dark field images of the *p-i-n* diode structures thus producing visual data to undertake strain analysis and to assess defect generation mechanisms as discussed in Chapters 4 and 5.

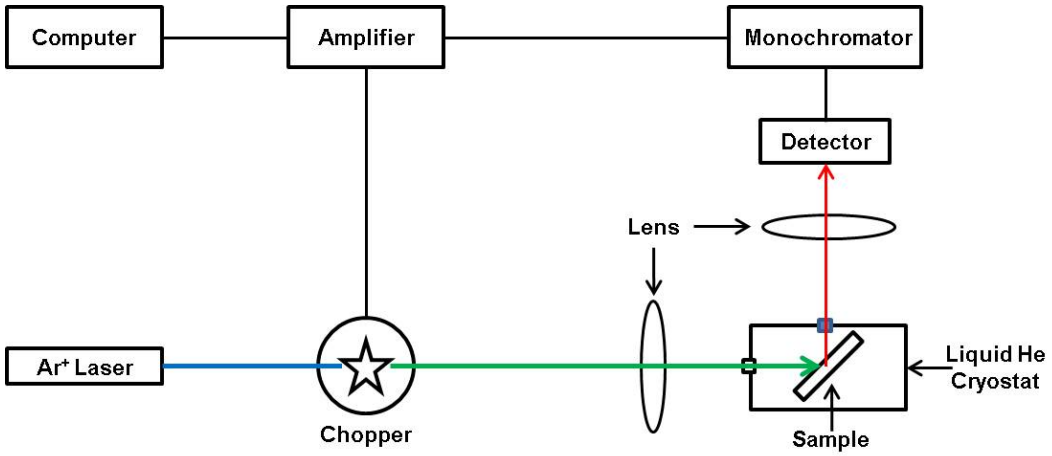

Fig. 3.7 Low temperature PL characterization setup

3.3.7 Current-Voltage (I-V) measurements

For I-V measurements a four-probe apparatus located in Dr. Michael Jin's Photovoltaic Materials Laboratory at UTA was employed. The characterization probes were manual 3-axis type micromanipulators with a magnetic base that sat on a metal chuck. The probe tips allowed contacting metal contact pads with sizes as small as 10 microns square. The four-probe system provided separate probes for current and voltage measurements thereby minimizing lead resistances and contact resistance between the platinum pads and the InGaAs base and emitter surfaces [3.7]. An air mass zero (AM0) equivalent light source was used to illuminate

the diode samples to determine the photoconductivity and photovoltaic properties of the diodes. These samples were mounted on a vacuum pump hold-down chuck. The entire assembly was enclosed in a black box in order to exclude outside light interference. A modification was made to this setup to characterize the light current behavior in the near to long infrared wavelength ranges, see Fig. 3.8. This modification consisted of a cardboard sleeve that was used to surround the AM0 light source with an opening at the bottom of the sleeve in which an infrared (IR) filter was taped to filter out visible light.

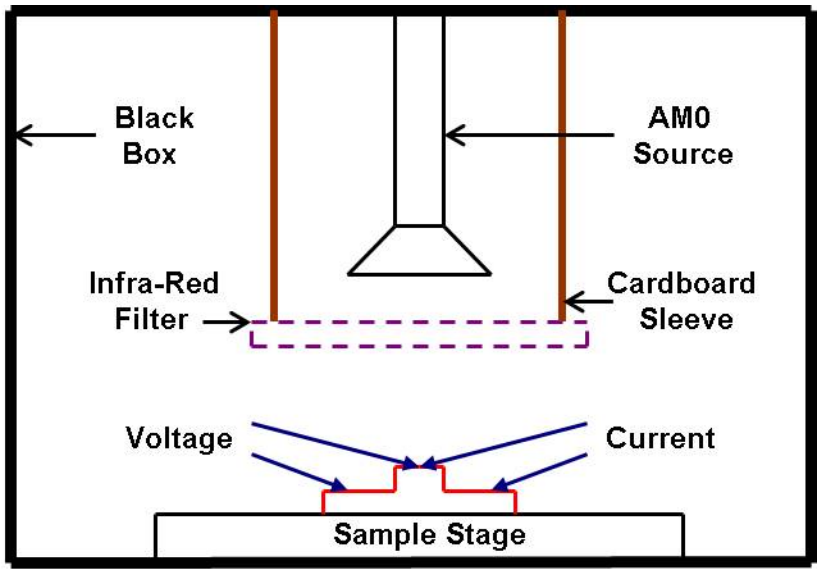

Fig. 3.8 Current-Voltage characterization setup using IR filter

Three types of filters were used, *viz.* 850 nm, 950 nm and 1300 nm, these blocked photons up to the wavelengths they were designed for. The 850 and 950 nm filters were about the size of a typical photography lens, *i.e*. 52 mm in diameter, while the 1300 nm filter was about 25 mm in diameter. It was designed to pass only long IR wavelengths. The long-pass IR wavelength filter was manufactured by Electrophysics Scientific Imaging. This filter exhibited ≤ 1% transmission for short-UV wavelengths up to approximately 1280 nm, and then rose within a span of 40 nm to at least 90% transmission for all longer wavelengths greater than the cutoff wavelength λ_c = 1300 nm ± 10 nm established at 50 % of the peak transmission. The use of the

850 nm, 950 nm, and 1300 nm filters therefore restricted the generation of any photocurrents from the intrinsic quantum dot region of the *p-i-n* devices arising from optical wavelengths shorter than the respective cutoff values of the filters. The discussion and analysis of the results of the photo current generation in the *p-i-n* devices are explained in more detail in Chapter 6.

CHAPTER 4

EPITAXIAL GROWTH CHARACTERIZATION

This chapter studies the epitaxial growth of InGaAs (*p*) / InAs / InGaAs (*n*) semiconductor diode structures, grown using a molecular beam epitaxy (MBE) tool. Section 4.1 outlines the analysis of epitaxial growths of the buffer and intrinsic regions. This section uses *in situ* reflection high energy electron diffraction (RHEED) method to analyze surface reconstruction while X-ray diffraction (XRD) results were analyzed to calculate alloy compositions and the band gap of the epilayers. Section 4.2 discusses the analysis of epitaxial growth of InAs quantum dots using RHEED, XRD, and photoluminescence (PL) data. It should be noted that the realization of the optimized kinetics of epitaxial growths, in Sections 4.1 and 4.2, have already been established in the literature and we analyze the observed structural and morphological growth trends based solely on those reports. Section 4.3 briefly discusses a high resolution transmission electron microscopy (HRTEM) image of the stacked QD device captured using the bright field method. Section 4.4 outlines the optoelectronic performance of InAs islands by correlating the PL data at long infrared wavelengths with previously reported work. This chapter outlines the structural and optical properties of the grown layers and the InAs quantum dots that formed a basis for the strain analysis and photocurrent behavior discussed in Chapters 5 and 6 respectively.

4.1 Buffer Layer Growth

4.1.1 Effect of arsenic background pressure on buffer layer growth

Any epitaxial growth analysis requires a combination of both thermodynamic [2.16 - 2.20] and kinetic [2.21 – 2.25] point of views. The thermodynamic approach provides a basis for energetically favorable states that are approached by the given kinetic conditions [4.1]. In case of InGaAs buffer layer growths, a thermodynamically favorable state is defined by the final

stoichiometry which is affected by kinetic factors such as the substrate temperature and the arsenic/gallium-indium background pressure ratio. The stoichiometry of an InGaAs buffer layer is dictated by the differences in sticking coefficients and the ratio of partial pressures between arsenic (group V) and indium-gallium (group III) elements [4.2]. During the targeted epitaxial growth of $In_{15}Ga_{85}As$ buffer layers atop a GaAs substrate, three samples, Z653, Z655 and Z665 (see Appendix A), exhibited an interplay between the thermodynamic and kinetic aspects of growth. Z653 and Z655 were grown at a substrate temperature of 550 ^{0}C while Z665 was grown at 600 ^{0}C with a V to III beam equivalent pressure (BEP) ratio of approximately 20, and a BEP = 9 and 15 was employed for Z653 and Z655, respectively. The difference in substrate temperatures is fairly close enough to be considered a 2x4 growth pattern (Fig. 2.5) suggesting a gallium rich growth front [2.31]. An *in situ* reflection high energy electron diffraction (RHEED) tool captured the surface reconstructions at (100) azimuth, seen in Fig. 4.1. Z653 and Z665 showed streaky RHEED patterns while Z655 showed a spotty pattern. A streaky RHEED pattern is a result of a smooth surface growth while a spotty pattern as seen in the Z655 RHEED pattern resembles reciprocal lattice rods formed as a result of the electron beam interacting with an uneven surface [4.3]. This observation was corroborated in secondary electron microscopy (SEM) images shown in Fig. 4.2. It was clear that a V-III BEP ratio lower than 10 was insufficient for arsenic chemisorption, hence resulting in forming droplets of group III elements on the surface during deposition. The Z665 growth was an indication to maintain a minimum BEP ratio of 15 for the rest of the growths.

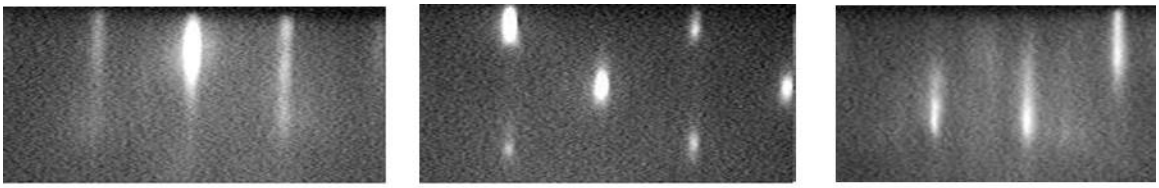

(a) (b) (c)

Fig. 4.1 In-situ RHEED patterns of (a) Z653, (b) Z655 and (c) Z665

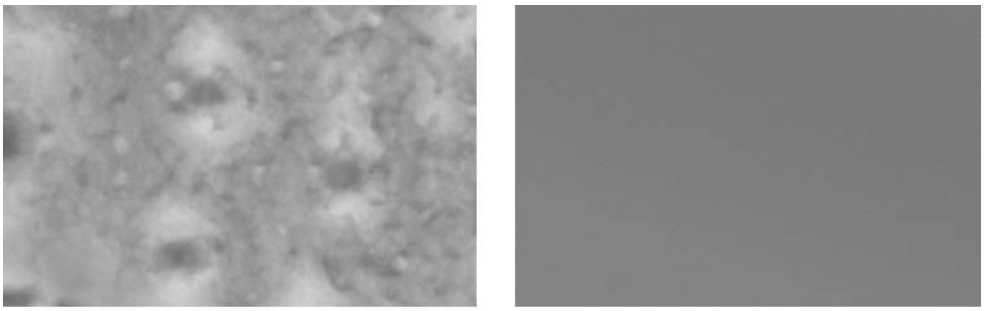

(a) (b)

Fig. 4.2 SEM images of (a) Z655 and (b) Z665

4.1.2 Effect of indium-to-gallium flux ratio

Samples Z653, Z655 and Z665 were grown using an indium to gallium BEP ratio of 0.38 for Z653 while 0.22 for Z655 and Z665, respectively. These three samples were tested using the D500 x-ray apparatus that produced counts-per-second (CPS) vs. 2θ curves, as shown in Fig. 4.3. A set of twin peaks at 66.02˚ and 66.2˚ are the characteristic $K_{\alpha 1}$ and $K_{\alpha 2}$ Bragg diffractions resulting from (004) GaAs planes [4.4], whereas diffractions from (004) planes of InGaAs buffer layers were recorded at lower 2θ values. InGaAs peaks for In-Ga ratio 0.38 and 0.22 appeared at 64.8 and 65.3 degrees, respectively; while a III/V BEP ratio of 9 for Z655 did not yield evidence of the twin peaks, as was deduced in the previous section, for InGaAs growth. The indium fractions in the buffer layers of Z653 and Z665 were calculated using the Bragg diffraction equation [3.5],

$$\delta = \lambda \frac{\sqrt{\left(h^2 + k^2 + l^2\right)}}{\left(2\sin\theta\right)} \tag{4.1}$$

where δ is the lattice constant, *h*, *k* and *l* are the Miller indices (004) of the diffraction plane, θ is the Bragg diffraction angle and λ is the wavelength of the Cu-K x-ray source, which is 1.5405 Å. GaAs peak at 66.02˚ translated into 5.6533 Å for the GaAs lattice constant [4.4] and the peaks at 64.8˚ and 65.3˚ correspond to lattice constants of 5.748 and 5.709 Å respectively. InGaAs being an alloy follows Vegard law [2.2] which states that at a constant temperature there exists

a linear relationship between the lattice constant and the fractional constituents of the alloy. Now GaAs lattice constant is 5.653 Å while InAs lattice constant is 6.0584 Å [4.4]. Vegard's law for InGaAs buffer layer alloy can be written as,

$$\delta[In_xGa_{1-x}As] = x\,(\delta[InAs]) + (1-x)\cdot(\,\delta[GaAs]) \qquad (4.2)$$

Using Eq., 4.2 we can calculate the In content in Z653 as, 5.748 = x (6.0584) + (1-x)(5.653), giving, x = 0.23; while for Z665, 5.709 = x (6.0584) + (1-x)(5.653), gives indium fraction x = 0.14.

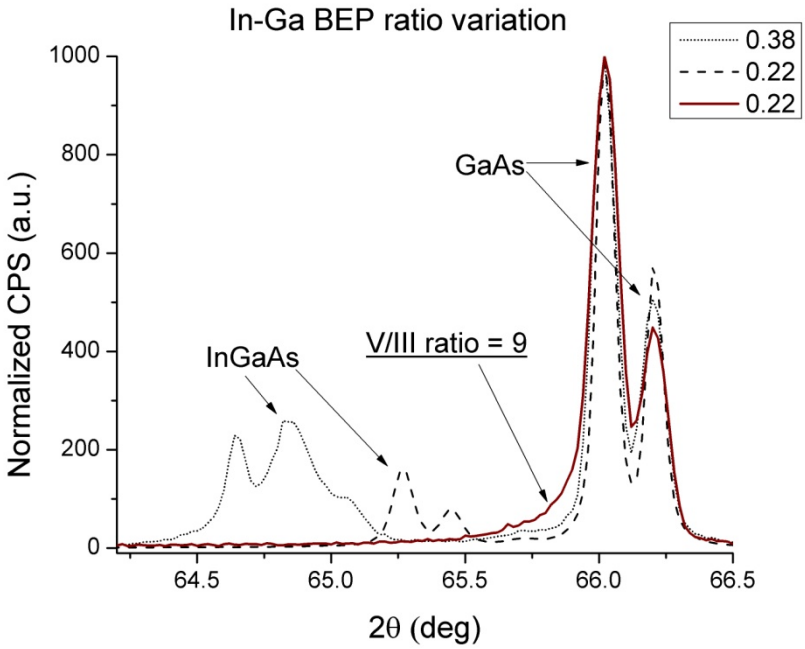

Fig. 4.3 X-ray diffraction curves as a result of V to III BEP ratio and In-Ga BEP ratio

The In-Ga BEP ratio of 0.38 resulted in $In_{0.23}Ga_{0.72}As$ buffer layer while a BEP ratio of 0.22 resulted in an $In_{0.14}Ga_{0.86}As$ buffer layer composition. The mismatch between the final thermodynamically favorable stoichiometry and the kinetic aspect of the In-Ga ratio is a result of difference in the sticking coefficients between the indium and gallium. The thermodynamics of the growth conditions dictates the buffer layer stoichiometry, rendering less control by the kinetic factors. Similar trend were observed during the growth of microstructures and will be

discussed in Section 4.2. Any sample growths after Z665 were designed to grow a buffer layer with InAs molar fraction of $x \approx 0.14$.

Growth rates for individual molecules in Z665 were calculated using the KLA-Tencor Alpha-Step IQ profilometer for epitaxial thickness measurements across a tab formed on the edge of the sample as result of the design of the MBE substrate holder clips that blocked any deposition beneath the clip holders. Using the profilometer the step height across the tab step gave the total epilayer thickness which when divided by the growth time gave the epilayer growth rate. Using this method the individual growth rates were recorded as, GaAs = 1.11 Å/sec, InGaAs = 1.37 Å/sec and InAs = 0.16 Å/sec or 0.053 monolayer (ML)/sec. These values were used for later microstructure growths of deposited epitaxial layers with a required monolayer precision.

InGaAs buffer layer in Z665 and any subsequent growths were *n*-doped using silicon. Van der Pauw measurements were performed by Dr. Kevin Clark and the doping concentration was calculated to be 1.03×10^{18} per cm^3. For both the *p*-*n* andi *p*-*i*-*n* diode structure growths the InGaAs top (emitter) layers was *p*-doped using beryllium with a doping concentration of 2×10^{18} per cm^3.

4.2 Epitaxial Growth of InAs Quantum Dots

As previously mentioned in Section 2.2.2, the Stranski-Krastanov (SK) mode of epitaxial growth is a result of interfacial strain release by an epilayer that has a significant lattice mismatch (heteroepitaxy) with an underlying substrate [1.10]. Fig. 4.4 shows different epilayer morphologies encountered during SK growth. Although a lattice mismatch is a pre-requisite, the amount of deposited material and the energy equilibrium dictate if the epilayer forms a uniform film with a lattice constant bi-axially strained to the underlying substrate (UF), a coherent island without any dislocation generation (CI) or a dislocated island (DI). By interfacial strain relaxation ($\Delta E_{elast} < 0$) islands are formed that increases the surface area of the epi-layer ($\Delta A > 0$) and so does the surface energy ($\Delta E_{surf} > 0$). This change in the surface energy competes with the energy of dislocation formation (E_{disl}). Fig 4.4 (b) shows the phase diagram as a

function of ratio of $E_{disl}/\Delta E_{surf}$ (defined as Λ) vs. the amount of monolayer deposited. Small Λ ratio results in lower dislocation formation energy favoring DI formation whereas large ratio with the right amount of monolayer (ML) thickness results in CI formation. Less than critical ML content will result in a uniform film without sufficient interfacial strain energy to form islands. Just as in InGaAs buffer layer growth, even in InAs quantum dot (QD) growth there is an interplay between the thermodynamically preferred states and the kinetic factors of the MBE growth. For SK growth mode the thermodynamics of the favored state are a result of energy equilibrium and the kinetic factors that can be controlled are the amount of InAs ML deposition, As BEP, substrate temperature and ML growth rate. Next sub-sections outline the effects of all of those boundary conditions to fabricate narrowly distributed, high density InAs islands that would exhibit strong to intermediate 3 dimensional quantum confinements.

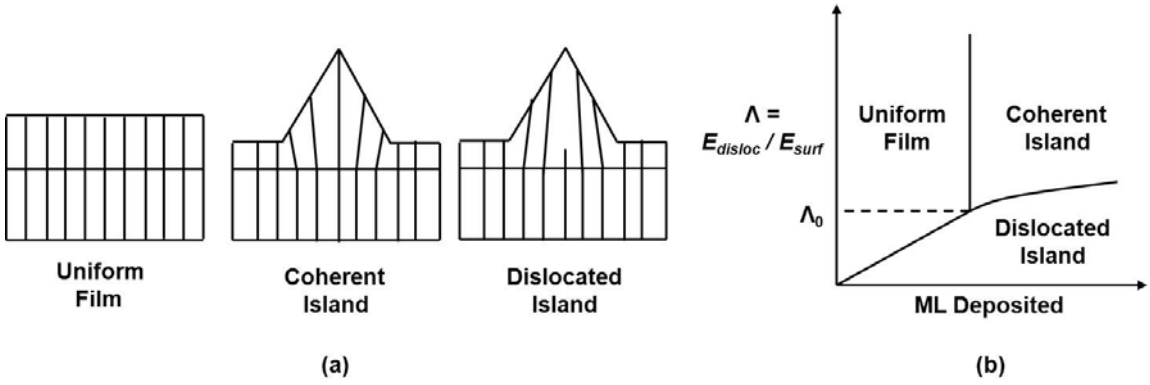

Fig. 4.4 Stranski-Krastanov (SK) growth [Shchukin, 2004]

4.2.1 Effect of InAs ML content and the substrate temperature

Our QD growths began with a substrate temperature of 530^0C, influenced by some recent successful attempts in the recent literature [4.5]. Formation of InAs quantum dots was recorded in RHEED images, Fig. 4.5 (a), captured during Z665 growth. For this growth the InGaAs buffer layer deposition step was followed by 30 Å of un-doped GaAs seed layer that provided sufficient misfit for InAs ML deposition. 2.9 ML of InAs (using growth rates calculated in Section 4.1.2) was deposited by opening the indium k-cell shutter for about 40 seconds while

Ga shutter was closed. Up to approx. 25th second RHEED exhibited a streaky pattern implying uniform film growth of biaxially strained InAs and after 25th second the streaks transformed into V shaped patterns (chevrons). From kinematical theory of electron diffraction [4.6] when an electron beam is incident at low angles to a periodic array of atoms then it interacts with the atoms within a few nanometers of the growth front resulting in a reciprocal lattice image with dimensions inversely proportional to the actual lattice, *e.g.* a low incident electron beam interaction with a thin foil results in a needle shaped reciprocal lattice image. This phenomenon is duplicated in plate-like precipitates formed during thermal processes of alloys [4.9]. If the plane of the plates is inclined to the plane of the electron beam then the reciprocal lattice image is seen as a tilted needle and is precisely the case as recorded in our RHEED images with chevrons indicating beam diffraction off of island facets. Feltrin *et al* simulated RHEED patterns for epitaxially grown islands and correlated the plane of the island facet with the angle formed by chevrons [4.8]. According to Feltrin, for a facet plane (11x) x is inversely proportional to the tangent of the semi-chevron angle, (α) in Fig. 4.5 (a), which in our case is around 40^0 and tan^{-1} of 20 is 1.2, so from 4.5 (b) the facet of the grown InAs island lies in the plane (112). The effect of ML content on the SK morphologies was recorded as RHEED images formed during the growth of Z686, see Fig. 4.6. This sample was grown as a test to recalibrate k-cells during the

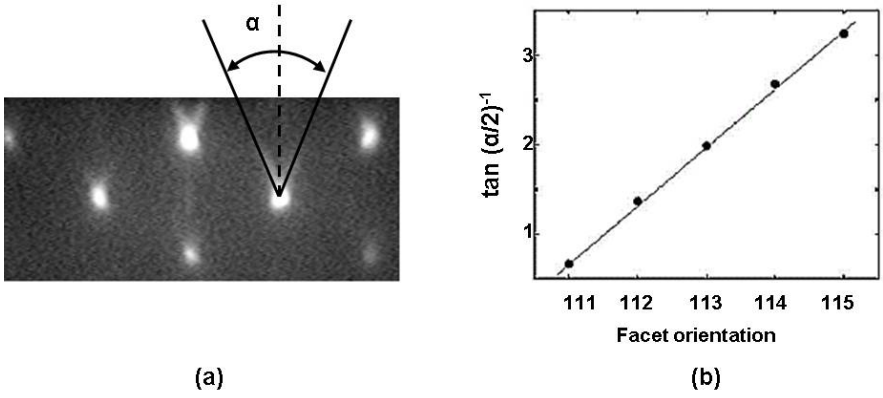

Fig. 4.5 (a) Z665 RHEED image after depositing 2ML InAs, (b) correlation between chevron angle and facet orientation [Feltrin, 2007]

course of several growths. Fig 4.6 shows RHEED images produced after deposition of (a) 2.1 ML, (b) 3.5 ML and (c) 4 ML of InAs. A striking difference is witnessed as chevron streaks, after 2.1 ML of InAs deposition, transformed into spotty/needle like streaks with 3.5 ML of InAs. This is attributed to transformation from pyramid/dome shaped islands to disc shaped islands [2.56]. Higher ML content further roughened the growth front resulting in diffused/spotty RHEED image, Fig. 4.6 (c). The formation of islands with about 2.5 was an indication to practice further growths with 2.5 ML of InAs deposition.

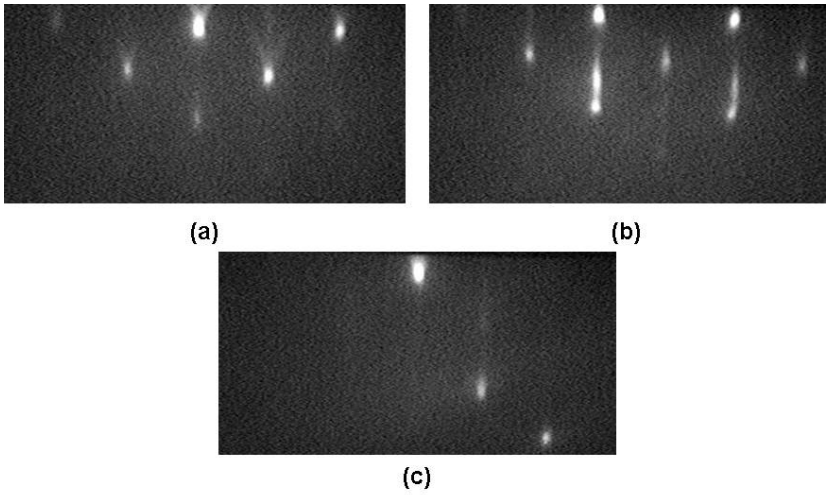

Fig. 4.6 RHEED images after deposition of (a) 2.1 ML, (b) 3.5 ML and (c) more than 4 ML of InAs

4.2.2 Effect of ML growth rate

Fig. 4.7 consists of RHEED images recorded for growths of samples (a) Z680, (b) Z677, (c) Z678 and (d) Z679 conducted at identical substrate temperature of 530 ^{0}C. The growth rates for InAs deposition were 0.05, 0.07, 0.12 and 0.16 ML/sec for Z680, Z677, Z678 and Z679, respectively. What can be noticed is the departure from v shaped chevrons (growth rate of 0.05 and 0.07 ML/sec) to streaky and faint chevrons (0.12 ML/sec) to a complete disappearance of chevrons (0.16 ML/sec). From earlier discussions and related reports the first inference will be that pyramid/dome shaped islands transformed to disc shaped islands to a film

morphology as increasing growth rate reduced the time needed for the interfacial strain release phenomenon and preferred film growth [2.57].

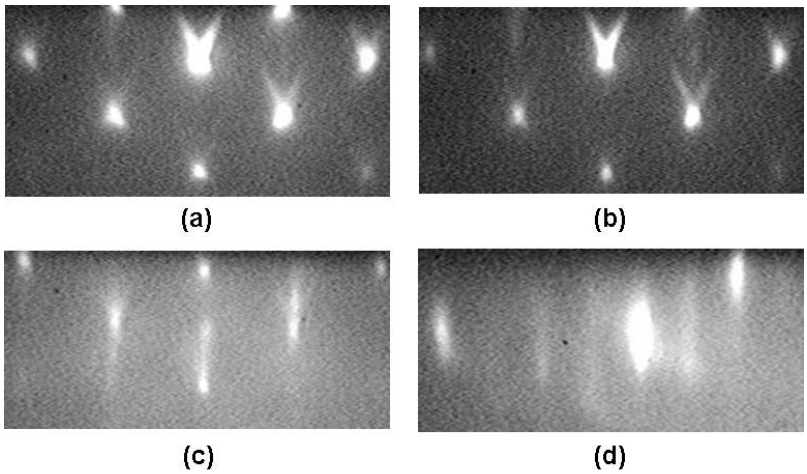

Fig. 4.7 RHEED images after deposition of about 2.7 ML of InAs at growth rates of (a) 0.05 ML/sec, (b) 0.07 ML/sec, (c) 0.12 ML/sec and (d) 0.16 ML/sec

Da Silva [4.9] and Ilahi [4.10] have reported increased island size with reducing InAs growth rate up to 0.001 ML/sec that resulted into 50 nm sized islands with weak quantum confinement effects since the de Broglie wavelength for InAs is 38 nm. Da Silva and Ilahi attributed the low density, large size island formation to the In atom desorption and subsequent suppression of nucleation of relaxed structures. Those reports and our RHEED images indicated InAs Ml growth rate of 0.05 ML/sec for further growths.

4.2.3 Effect of Arsenic background pressure on InAs quantum dot growth

Figs. 4.8 (a) Z669, (d) Z690 and (g) Z680 show AFM images of the topography of InAs islands formed under arsenic beam pressures of 5.7 e-06 (Z669), 7.9 e-06 (Z690) and 8.9 e-06 mBar (Z680), respectively, with the corresponding lateral views in Figs. 4.8 (c) Z669, (f) Z690 and (i) Z680. 2.9, 3.2 and 2.1 ML of InAs was deposited for Z669, Z690 and Z680 samples, respectively with the corresponding QD size distribution as shown in graphs 4.8 (b), (e) and (h). It is evident from AFM images that with increasing arsenic flux the QD density increased while the size distribution was narrowed down. This is attributed to the reduction of the In adatom

diffusion length [2.58, 4.11]. To summarize this phenomenon when an indium atom from the K-cell beam gets chemisorbed onto a heated surface then the probability of the chemisorbed ad atom to encounter an arsenic atom increases with a higher As flux. Due to which the ad atom has to diffuse to a relatively shorter distance to form InAs molecules than it would with a comparatively lower As flux plus a reduced possibility of desorption of the adatom results in to a

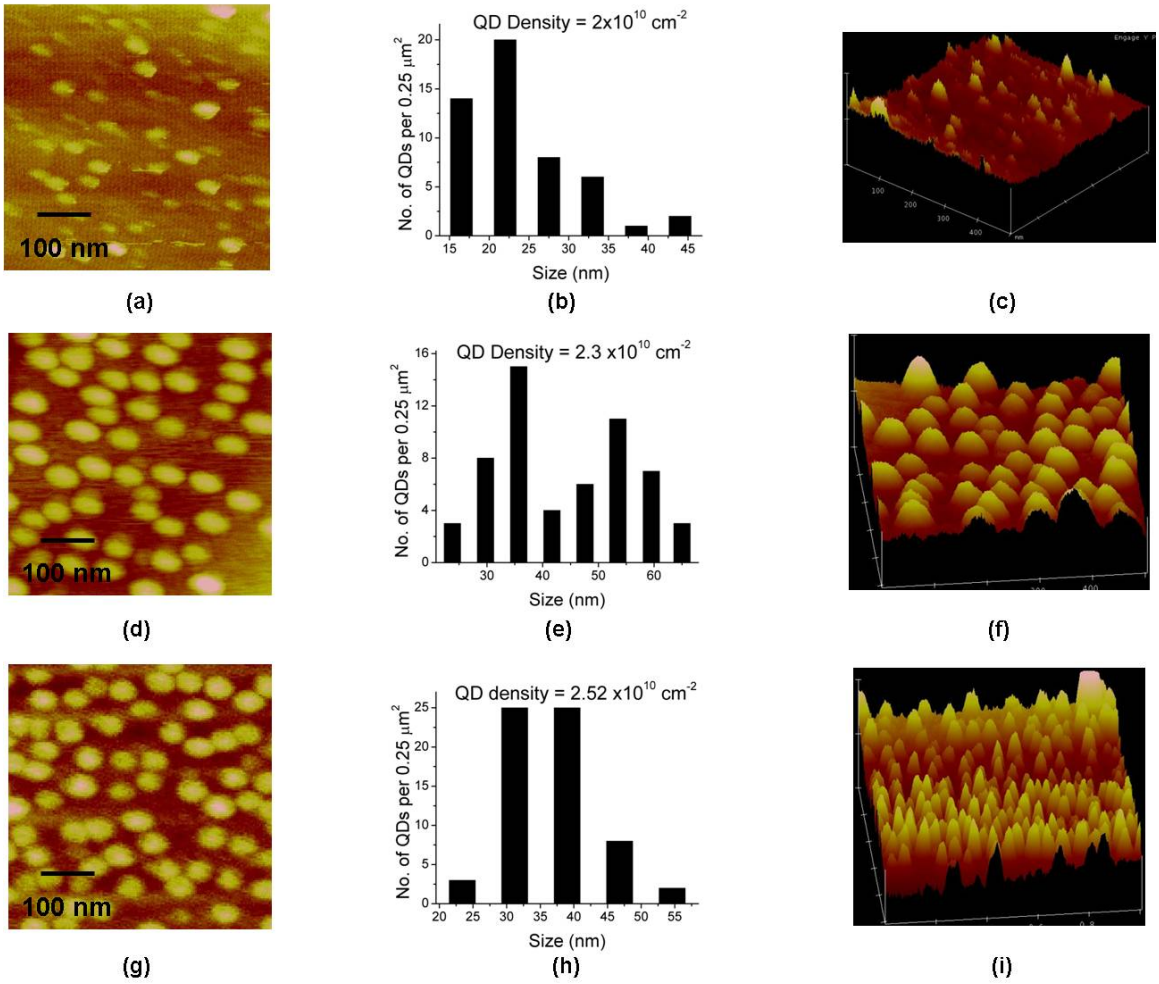

Fig. 4.8 Effect of arsenic background pressure on the density, size distribution and shape of InAs QDs. (a) – (c) As BEP = 5.7x 10^{-9} mbar, (d) – (f) As BEP = 7.9 x 10^{-9} mbar and (g) – (i) As BEP = 8.9 x 10^{-9} mbar

uniform film. With a uniform epilayer the misfit strain expands evenly and initiates the SK mode mechanism within a very narrow time span over the entire surface. This effect helped reduce

the structural inconsistency among the islands and the epilayer growth resulted in a narrow distribution of dot sizes that continued past SK initiation phase as the ad atoms for rest of the growth time were evenly deposited atop the islands. Fig. 4.8 shows that the QD density increased from 1.8 x10^{10} (b) to 2.3 x10^{10} (e) per cm^2 with an increase in the As flux from 5.7 to 7.9 e-06 mbar that resulted in narrowing of the InAs island size distribution from 16 to 40 nm to 30 to 55 nm. Reduction in ML deposition from 3.2 to 2.1 formed QDs with narrowest distribution of 32 to 38 nm with a density of 2.5 e10 per cm^2. . Lateral AFM images show that the height of the QDs increased from Fig. 4.8 (c) 3 ± 1 nm to (f) 7 ± 2 and (i) 7 ± 1 nm as the arsenic pressure was increased. It should be noted that the scan size for Fig 4.8 (i) is 1μm x 1μm while that for Figs. (c) and (f) is 0.25 μm x 0.25 μm. Although the tendency to form pyramidal shaped islands is enhanced in SK mode, the visual result in dome shapes could be attributed to the radius of the AFM tip that limited the feature contrast to few angstroms. As a future work scanning tunneling microscopy (STM) could serve as a better tool for morphological characterization of grown dots.

4.2.4 Misfit strain and coherent islands

The misfit strain drives the thermodynamics of Stranski-Krastanov epitaxial growth that results in three different growth morphologies, *viz.*, (a) uniform film (UF), (b) coherent island (CI) and (c) dislocated island (DI). Recalling the discussion in Section 2.2.3, Ratsch and Zangwill [2.52] proposed that a moderate to low monolayer deposition of a lattice mismatched material with more than, approx., 2% of misfit strain produces coherent islands. A kinetic extension to their work was provided by Pintus [2.55] and Snyder [2.56] when the amount of monolayer deposition was correlated with the adatom diffusion length, given by Eqn. 2.19 as, $L = \sqrt{D\tau}$; where D is the surface diffusivity and τ is the time of deposition. By reducing the adatom diffusion length the amount of monolayer to be deposited is restricted in the moderate to low regime as predicted by Ratsch. Although Pintus and Snyder provided a useful kinetic insight however an exact measurement of adatom diffusion length is very difficult because surface

diffusivity is a function of substrate temperature and, as previously mentioned in Chapter 3, due to substrate installation and rotation requirements in the MBE tool the radiant filament for substrate heating was not in direct contact with the substrate thereby increasing the substrate temperature accuracy up to ± 25 ^{0}C of the intended temperature. Nevertheless the adatom diffusion length phenomenon provides sufficient qualitative insight to fabricate coherent islands. Shchukin *et al* stepped further by comparing probability of dislocated island formation (P_d) and the distribution of island volume (P_d), see Fig. 4.9 [4.12]. Shchukin stated that if the average volume of islands on a growth front is moderate then only a small fraction of islands contains defects but for a comparatively higher average volume a larger fraction of islands is defective.

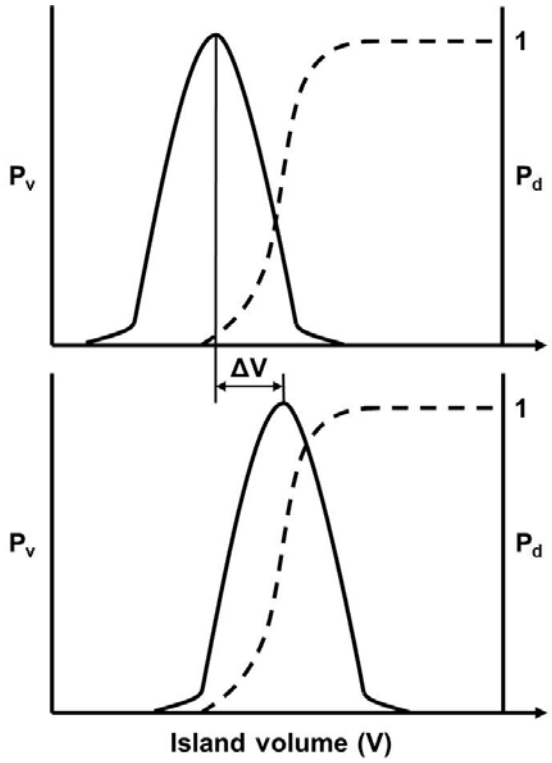

Fig. 4.9 Distribution function of island volume (P_v) and probability of dislocated islands (P_d) [redrawn from Shchukin, 2004]

By this rationale when sample Z680 was grown by reducing adatom diffusion length for InAs ML deposition the average volume distribution resembled the QD size distribution, seen previously in Fig. 4.8 (h) suggesting lower fraction of dislocated islands compared to sample Z690, Fig. 4.8

(e) that shows a higher average volume of islands. Direct evidence of dislocated islands was recorded by Guha [4.13] using a cross sectional transmission electron microscopy (TEM) imaging technique for a sample with 7 ML of InAs epitaxially deposited on a GaAs substrate and later capped by epoxy, Fig. 4.10. Dislocations are marked by arrows while arrow '1' points to a stacking fault at the island edge. Guha concluded that island sizes more than 40 nm incorporated dislocations while smaller islands remained relatively coherent. In this work we rely on TEM imaging, discussed in the next section, to record any evidence of dislocated island formation.

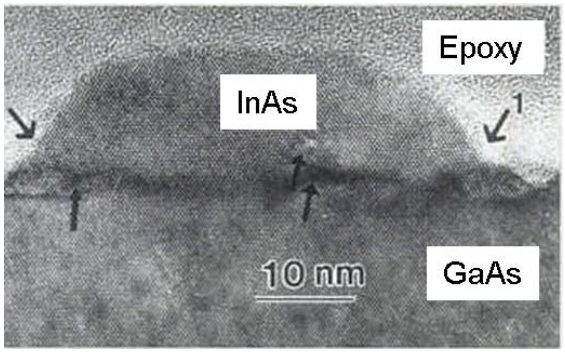

Fig. 4.10 Transmission electron microscope image showing a large InAs island with dislocations at the interface [Guha, 1990]

4.3 InAs Quantum Dot Characterization

Growth parameters for sample Z665 (InGaAs buffer layer) and Z680 (narrowly distributed high density InAs QDs) were adopted to grow an InGaAs (*p*) / InGaAs (*n*) homojunction device, Z673 (HOM) and an InGaAs (*p*) / InAs (*i*) / InGaAs (*n*) quantum dot device, Z682 (QD device) with 5 InAs QD layers incorporated within the intrinsic region, respectively. To reminisce from Section 3.1.4, the intrinsic layers were grown in 3 steps, with the substrate held at 530 ^{0}C, *viz*.: (a) 3 nm of un-doped GaAs seed layer growth, (b) 2.1 ML of un-doped InAs growth at the rate of 0.054 ML/sec, (c) 3 nm of un-doped $In_{0.14}Ga_{0.86}As$ cap growth. Steps (a) and (c) were followed by 5 min annealing under As flux alone while 2 minutes. of annealing was performed for self-assembled InAs QDs. QD device was further fabricated into a focused ion beam sample and

tested using high-resolution transmission electron microscopy (HRTEM) to capture a bright field image, see Fig. 4.11. The triangular image in the center is an InAs QD with the InAs wetting layer (WL), which is a uniform film bi-axially strained to the underlying GaAs seed layer, extending from the base of the triangle. From the HRTEM image the height of the QD is seen as approximately 5 nm which is a slight departure from 7 nm, as was measured previously using AFM. We note that the top of the island that has sufficiently released the strain consists of a significantly different lattice constant than the surround InGaAs cap producing diffraction contrast while the base of the island has lattice constant closer to GaAs seed layer and blends in with the GaAs seed layer image forming comparatively lower contrast. Besides biaxial straining and the strain decay within the island two other phenomena diminished HRTEM contrast, *viz.*, (i) indium-gallium inter-diffusion as a result of strain gradient between relaxed top of the island and the surround InGaAs cap [4.14 - 4.16] and (ii) segregation of group III atoms at the epilayer surface [4.17 - 4.19]. Interdiffusion drags Ga atoms from the capping layer into the island truncating the pyramid that possibly resulted into the height measurement discrepancy between AFM and TEM tools. This phenomenon reduced the indium fraction within the islands and also a weak bonding of the adatoms resulted in the surface segregation of indium. Both of these phenomena have been reported in the literature that employed annealing via growth interruption after deposition of both InAs ML and InGaAs cap alloy, departing the composition of each layer from the intended growth parameters [4.16, 4.19]. Although annealing of islands remains a vital step for > 2 ML of InAs deposition [2.56 - 2.58] a random composition distribution, cladding of the islands by InGaAs capping layer and bi-axial lattice straining of the intrinsic layers generated insufficient contrast making TEM imaging difficult. Hence we relied on AFM results to characterize the electronic properties of the islands in section 4.5, but nevertheless HRTEM characterization presented visual evidence of an InAs island.

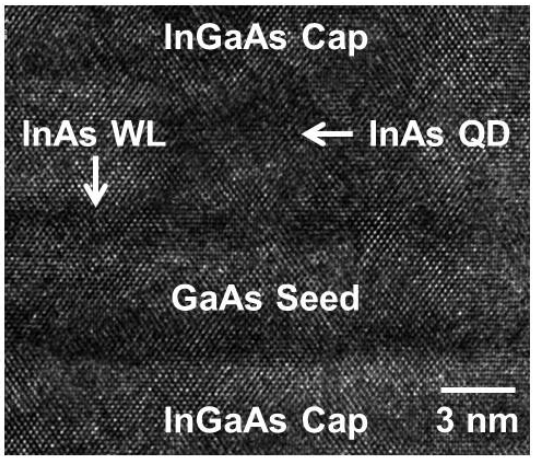

Fig. 4.11 Cross sectional HRTEM image of 5 layered QD device

4.4 QD and HOM Epitaxial Growth Comparison

A comparison of structural, compositional and electronic properties between QD and HOM samples was performed using x-ray (XRD), Fig. 4.10, and photoluminescence (PL) spectroscopy, Fig. 4.11. In Fig. 4.12 two sets of twin peaks at approx. 65.3 degrees belong to Kα diffraction emerging from (004) InGaAs base (*n*-doped) and emitter (*p*-doped) layers while the twin peaks at 66 degrees belong to (004) GaAs buffer layer and substrate. A shoulder at approx. 65 degrees for the QD sample is attributed to the randomly formed InGaAs alloy within the intrinsic quantum dot region as a result of inter-diffusion [4.14 - 4.16] and surface segregation [4.16, 4.19] phenomena. Another evidence of intrinsic layers was seen under PL spectra generated by cooling down the samples to 6 K, see Fig. 4.13. QD and HOM samples exhibited an InGaAs peaks at 920 nm (1.35 eV) and 934 nm (1.32 eV), respectively with a very close full width at half maximums (FWHM) (~60 meV). The indium content within the base and emitter layers was calculated from XRD plots using the same method discussed previously in Section 4.1.2 that used Vegard with the results noted in Table 4.1. The alloy band gap, on the contrary, followed a parabolic relation [2.3],

$$E_g = a + bY + cY^2 \tag{2.1}$$

where *a* and *b* are determined by materials of the alloy while *c* is the bowing co-efficient which measures the deviation from the linearity. This coefficient comprises of a periodic component, c_i, that recognizes the change in bond length and an aperiodic component, c_e, which is a root-mean-square fluctuation in the electron potential from its periodic amplitude. Madelung has formed a relation for an InGaAs alloy band gap as [4.21],

$$E_g = 0.324 + 0.7(1-x) + 0.4(1-x)^2 \tag{4.3}$$

Results are outlined in Table 4.1. XRD data predicted smaller InGaAs band gap than PL data. This is attributed to the cryo conditions of PL testing that slowed down the lattice vibrations [4.22] predicting higher *Eg* while XRD testing was carried out at the room temperature. Although, evidently, both XRD and PL data recorded slightly lower *Eg* in the HOM sample on an account of higher InAs fraction compared to the QD sample. What is also noticeable in both the plots is the existence of intrinsic region, especially in the PL spectrum that recorded photon activity starting from around 970 up to 1200 nm. The characterization of individual intrinsic layers by any quantitative means was extremely difficult since the thicknesses of each layers were within a range of 5 to 10 nm (detailed cross sectional TEM and corresponding PL discussion are presented in Chapter 5) plus the added effects of material interdiffusion phenomena. But qualitatively both PL and XRD confirmed the existence of an intrinsic region in the QD sample which was not present in the HOM device.

Table 4.1 QD and HOM buffer layer comparison

Sample	2 θ (deg)	Lattice constant (Å)	InAs fraction	Band gap, E_g, from XRD (eV)	Band gap, E_g, from PL (eV)
QD	65.25	5.712	0.145	1.215	1.35
HOM	65.22	5.715	0.152	1.205	1.32

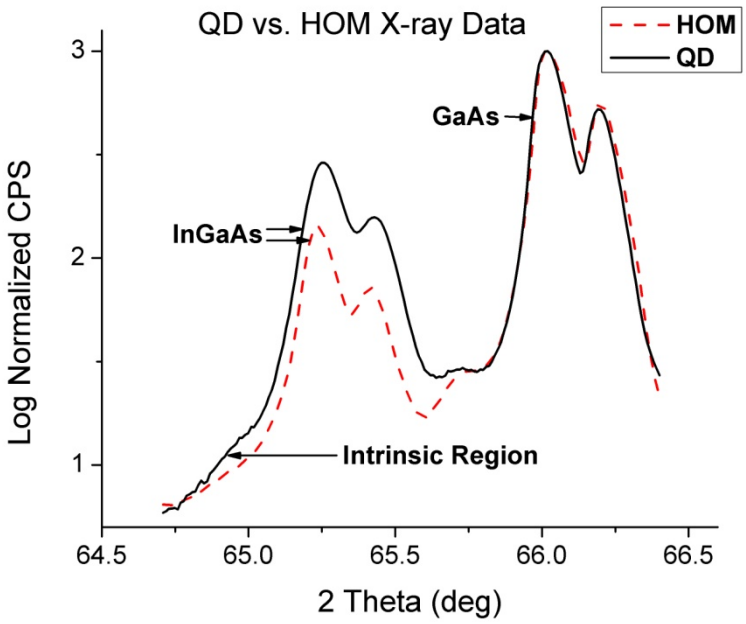

Fig. 4.12 Epitaxial growth comparison using XRD

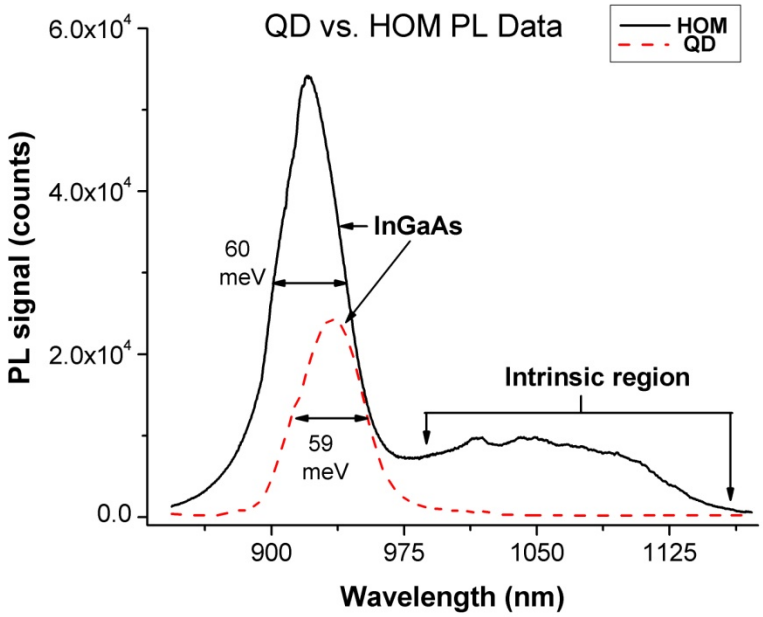

Fig. 4.13 PL comparison

4.5 Electronic Properties of InAs Quantum Dots

An entire plot of the PL activity recorded from 800 nm to around 1600 nm wavelength range for the QD sample is seen Fig. 4.14. As mentioned in the previous section the PL activity in the near IR range belonged to intrinsic region of the QD sample however in the full range plot some photon activity was recorded in the long IR range of around 1400 nm. We speculate this photon activity to be arising from strain released part of the InAs QDs that exhibits 3 dimensional quantum confinements. In this section we attempt to correlate an InAs quantum dot band gap calculated, by Ghanad-Tavakoli *et al* (GT) [4.23], from the separation of the density of states as a function of misfit strain between the island and the seed layer. GT attempted InAs QD band gap calculation for islands epitaxially grown over different $In_xGa_{1-x}As$ substrates with varying InAs fraction. Fig. 4.15 shows the band diagrams of (a) our QD device and (b) GT's quantum dot (GT-QD) structure. Both the diagrams are not drawn to scale but the apparent difference between the two structures is the buffer layer grown on the GaAs substrates and the seed and capping layers.

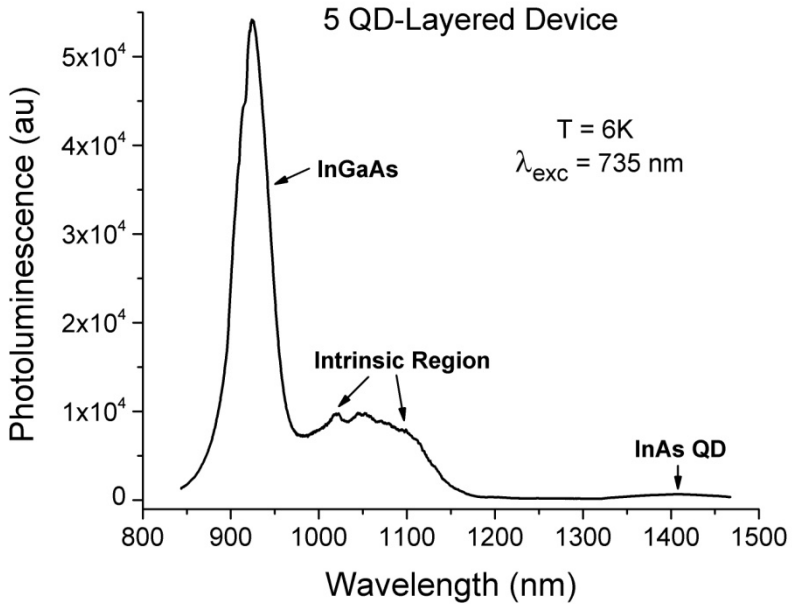

Fig. 4.14 Photon activity at 1400 nm

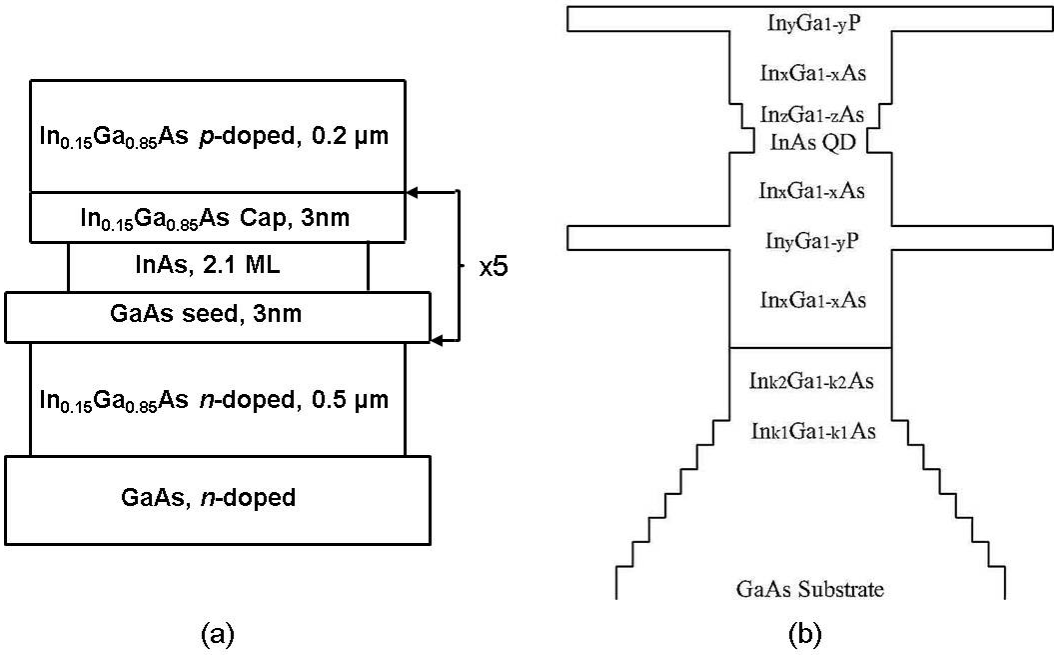

Fig. 4.15 Band diagrams for (a) QD device and (b) GT-QD structure [Ghanad-Tavakoli, 2009]

GT used an InGaAs buffer compositionally graded at the rate of 0.02 InAs fraction per 100 nm epilayer growth with the final InGaAs alloy had $0.2 \leq x \leq 0.3$, while our QD sample consisted of $In_{0.15}Ga_{0.85}As$ buffer layer without any compositional grading. The GT-QD sample consisted of a two-step seed layer growth with deposition of a 25 nm InGaP and a 150 nm InGaAs epilayers followed by InAs island formation which were capped by the same two layers, except in a reverse order of seed layer stack. The QD sample, on the other hand used a single GaAs seed layer (3 nm) and an InGaAs capping layer (3 nm). One of the GT-QD structures consisted of an InGaAs seed layer with $x = 0$, *i.e.* a GaAs seed layer, similar to our QD device. AFM data for QD and GT-QD structures is compared in fig 4.16 (a) and (b) respectively. GT-QD structure had island diameters close to 28 nm while our QD device islands were on an average 35 nm in size but both the samples exhibited an island height of 7 nm. GT considered a cylindrical section of an intrinsic layer that consisted of seed, island and the aping layer. Using the Green's function and the Hamiltonian operator for cylindrical co-ordinates GT

formulated an expression for the density of states within an InAs island that incorporated lattice strain as a result of the misfit between that island and a base layer, as [4.23],

$$D(E) = \frac{1}{2\pi}\int 2\pi r dr dz A(r, z; E) \qquad (4.4)$$

In Eqn. 4.4 $A(r, z; E)$ represents the diagonal elements related to the Green's function, with r representing the position of an atom within a hypothetical cylindrical island with respect to the center of the cylinder and z represents the vertical dimension. From Eqn. 4.4 GT simulated hole and electron density of states for InAs islands of 28 nm size and 7 nm height grown on GaAs buffer layer (misfit ε = 7.16%), see Fig. 4.17. As a result of 3 dimensional carrier confinement atomic-like discrete wave-function were generated with the first electron density of state at 0.34 eV and the first hole density of state at 0.065 eV which together when added to the strained InAs bulk band gap (0.48 eV) translated into the first electron-heavy hole transition to be at 0.885 eV, (1393 nm). Their room temperature PL data confirmed this transition. Given the close similarity of our QD sample with the GT-QD structure, GT's DOS calculations were adopted for our PL data that showed a peak around 1400 nm. However our islands are 35 nm on an average and the PL testing was carried out at substrate temperature of 6K. Even though a definite estimate of e^1-hh^1 transition energy for our sample is unavailable but a qualitative resemblance with GT's data could be made on a basis that the increased island size in QD sample red-shifted the DOS separation while liquid helium temperatures slowed down the lattice vibrations that blue-shifted the DOS separation. We can reasonably infer that the peak at 1400 nm in our PL data belonged to e^1-hh^1 optical transition within the InAs islands. A curve fitting procedure was performed using Origin 8.5.1 (student version) for the peak recorded at 1400 nm wavelength which separated that peak into 5 separate Gaussian peaks, see Fig. 4.18. Those peaks had maxims occurring at 1350 (I), 1372 (II), 1408 (III), 1437 (IV) and 1456 (V) nm wavelengths. Previously in Fig. 4.16 (a) we have seen that the QD sample had some islands of about 25 and 42 nm size while majority of the islands were narrowly distributed around 35 nm ± 3nm size. Photon transitions within the small and large islands could be attributed to peaks I, II

and IV,V; respectively while the photon activity of peak III is attributed to the narrowly distributed islands. The overall low PL intensity of the 1400 nm peak compared to the InGaAs buffer and intrinsic peaks is attributed to the fact that the top section of islands consisted of strain released pure InAs, that exhibited 3D confinements, and this section of the islands had a relatively very small volume fraction and eventually the absorption coefficient compared to rest of the sample.

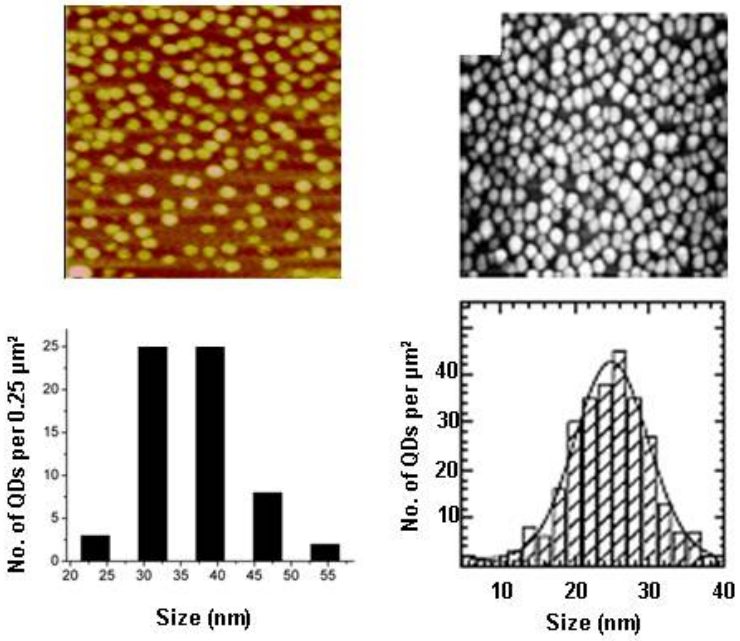

Fig. 4.16 AFM images for (a) QD and (b) GT-QD [Ghanad-Tavakoli, 2009]

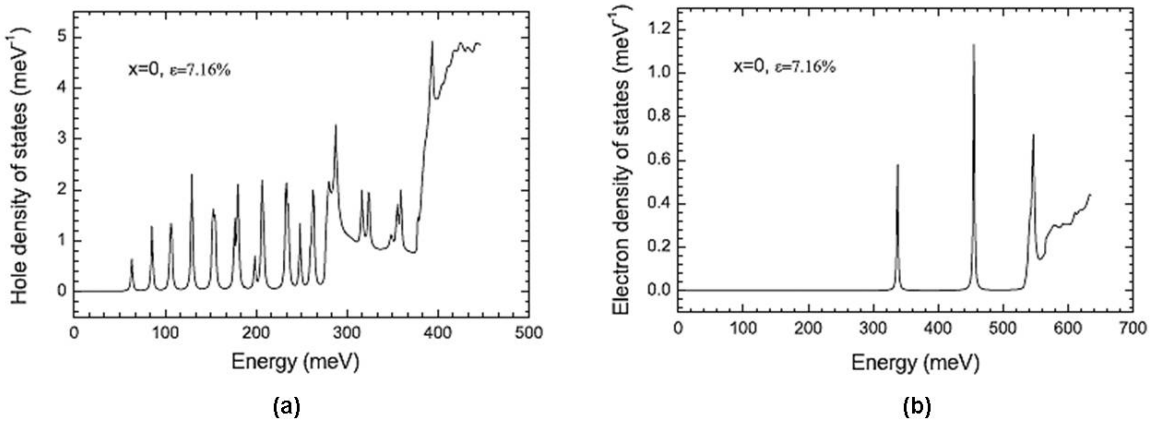

Fig. 4.17 (a) Electron and (b) hole density of states [Ghanad-Tavakoli, 2009]

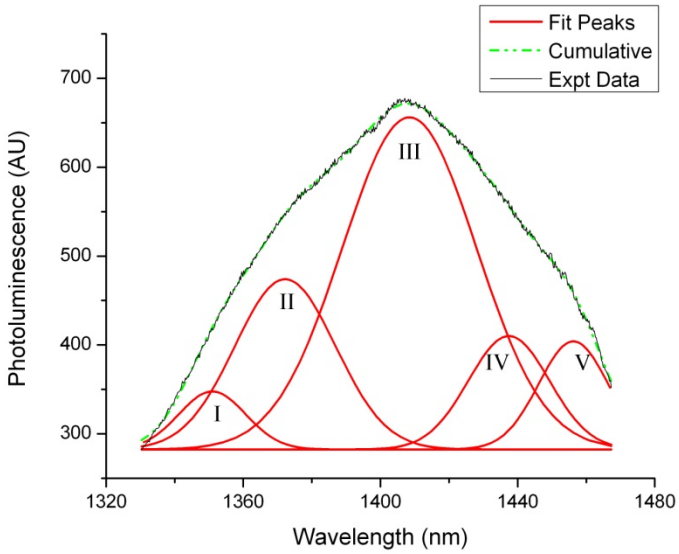

Fig. 4.18 Photoluminescence at 1400 nm from QD sample

In summary, this chapter has outlined the kinetic factors responsible for optimal epitaxial growth conditions of QD and HOM samples. The X-ray results provided lattice constants of the buffer and intrinsic layers which were used to calculate the buffer and emitter layer alloy compositions. AFM results recorded structural properties of the islands. Photoluminescence spectroscopy corroborated analysis of X-ray results along with a long IR PL peak, which when correlated with a previously published report, was reasonably assigned to a photon activity restricted to InAs islands. The structural and electronic properties realized after the analysis of QD and HOM devices have been used as a basis for the epitaxial strain analysis and photocurrent behavior discussions in Chapters 5 and 6 respectively.

CHAPTER 5

ANALYSIS OF SUPPRESSION OF DISLOCATIONS

This chapter primarily concerns with the phenomenon of dislocation generation in the lattice mis-matched semiconductor devices. Using the elastic strain release theory, discussed previously in Section 2.1.2, an analysis is presented that studies enhanced misfit strain absorption within the QD device (Z682, see Appendix A) without the generation of dislocations. In Section 5.1 the theory behind critical epilayer thickness is briefly presented with its application to InGaAs buffer layer in the QD device. Section 5.2 outlines a calculation of the intrinsic region thickness and average lattice constant using cross-sectional high resolution transmission electron microscopy images, x-ray diffraction curves and photoluminescence data. These results are used to calculate the critical thickness and compared with the actual experimental evidence along with a strain comparison between HOM (Z673, see Appendix A) and QD samples. Section 5.3 presents an analysis of strain release as a function of the misfit using x-ray diffraction data. A signature of the elastic and plastic regions of a biaxially strained epilayer that is captured in the x-ray characterizations is discussed. Section 5.4 uses the understanding of strain release mechanism from Section 5.3 to compare the strain build-up within the QD and HOM samples. Section 5.5 outlines a dark current comparison between QD and HOM samples. Section 5.6 compares the buffer layer growth method, employed in this work, with the previous attempts at strain reduction in the lattice mismatched semiconductor systems.

5.1 Critical Epilayer Thickness

The epitaxial growth of lattice mismatched layers, called heteroepitaxy, is defined by the misfit strain (f) between the two layers as,

$$f = \frac{\delta_a - \delta_0}{\delta_0} \tag{1.1}$$

where 'δ_a' and 'δ_0' are the lattice constants of the epilayer and substrate, respectively. On an account of the elastic properties of the atomic bonds in a semiconductor this misfit is absorbed by the epilayer atoms by undergoing stretching and bending thereby increasing the strain energy, E_ε, of that epilayer. This phenomenon of biaxial straining continues for the lattice mismatched growth until epilayer reaches a critical thickness, h_c, at which E_ε becomes higher than the energy to generate one dislocation, E_d. At this critical point the thermodynamics of the system favor the generation of a dislocation by breaking one of the atomic bonds at the epilayer-substrate interface since a section of the epilayer in the vicinity of interface undergoes higher biaxial straining compared to the rest of the epilayer. Up to h_c the elastic fraction, ε, of the epilayer strain energy matches the entire misfit, *f*, but for an epilayer thickness ≥ h_c a part of the misfit is absorbed elastically while the rest is absorbed plastically, *p,* by forming misfit dislocations.

$$f = \varepsilon, \left(h < h_c\right) \tag{5.1}$$

$$f = \varepsilon + p, \left(h \geq h_c\right) \tag{5.2}$$

Recalling a discussion from Section 2.1.2, the first attempt to calculate the critical thickness for a heteroepitaxial growth of face centered cubic metals was performed by Frank and Van der Merwe (FVM) [2.5, 5.1, 2.7, 5.2] based on a one dimensional dislocation model proposed earlier by Frenkel and Kontorova [2.6]. Later Matthews grew gold on top of a palladium substrate by vapor deposition method and he reported dislocation free epilayer growths thicker than FVM model [2.9]. Matthews speculated effects of (a) diffusion between layers forming an alloy, (b) strain energy within the palladium substrate since it was initially grown on a sodium chloride crystal and (c) the departure of the mechanism of dislocation generation from FVM model. Using continuum elasticity theory Matthews and Blakeslee (MB) proposed their own model of critical thickness for the semiconductor epitaxial growths that

incorporated 60^0 dislocations [2.11]. Another attempt to formulate critical thickness came from People and Bean (PB) for germanium-silicon systems using energy balance criteria [5.3]. Based on their experimental data PB generated an expression for critical thickness and compared it to the MB and FVM models, see Fig. 5.1. For less than 1.5% of misfit PB recorded higher critical thicknesses than both FVM and MB, for 1.5% ≤ *f* ≤ 2.5% PB recorded higher critical thickness than FM prediction but lower than MB's prediction while for more than 3% misfit PB's experimental data showed lower critical thickness than both FVM and MB predictions. MB had previously proposed that at critical thickness the line tension in a threading dislocation, overgrown from a substrate into the epilayer, increases thereby bowing and extending that dislocation to form an interface dislocation via glide mechanism, which according to PB was not possible for less than 2% misfit systems. PB proposed a half-loop surface nucleation phenomenon which glides from the surface to interface forming a misfit dislocation. In response to this mechanism Fitzgerald noted that a set of pre-requisites for the half-loop mechanism, such as inhomogeneity, drastic change in the growth mode (roughening instead of smooth 2-dimensional) and cross-contamination in the form of particulates/impurities from the deposition source or the vacuum chamber in an ultra-high vacuum epitaxial growth tool; are becoming obsolete due to a constant evolution of the substrate cleaning procedures, purity of sources, slow growth kinetics and horizontal deposition plane of the growth tool [1.2]. In this project our growth systems had less than 2% of lattice mismatch so we presume misfit strain release *via* breaking of atomic bonds at the epilayer-substrate interface, but we do adopt Matthews-Blakeslee critical thickness model for the prediction of defect generation in an epitaxial multi-layer system, given as [5.4],

$$\varepsilon = \frac{b\left(1-\nu\cos^2\alpha\right)}{\pi h\left(1+\nu\right)\cos\lambda}\left(\ln\frac{h}{b}+1\right) \tag{5.3}$$

In Eqn. 5.3 ε is the strain fraction of the total misfit that is absorbed elastically, *b* is the Burger's vector (4 Å for 60^0 dislocations in III-V semiconductors), ν is Poisson's ratio of the epilayer, λ is

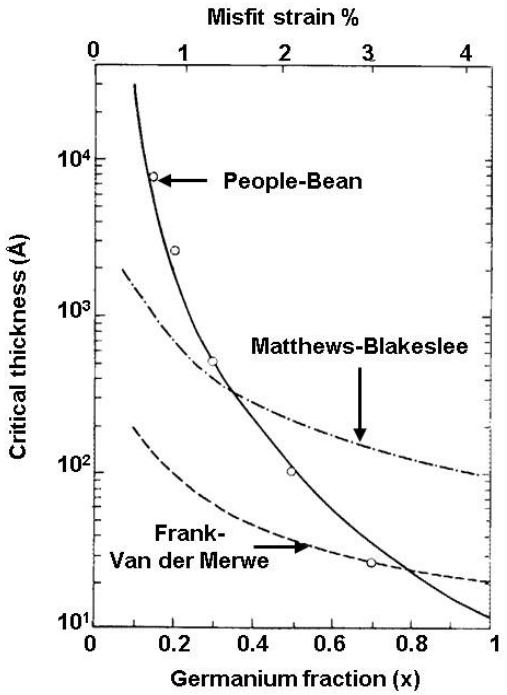

Fig. 5.1 A comparison of critical thickness models [People-Bean, 1985]

the angle between the slip direction and that direction in the film plane which is perpendicular to the line of intersection of slip plane and the interface, α is the angle between the dislocation line and its Burgers vector (cos α = cos λ = ½, for III-V semiconductor systems) and *h* is the thickness of the epilayer. For $h < h_c$ $\frac{\varepsilon}{f} > 1$, but for $h \geq h_c$ $\frac{\varepsilon}{f} \leq 1$. Using Eqn. 5.3 we can calculate the critical thickness for our $In_{0.15}Ga_{0.85}As$/GaAs system. For an $In_{0.15}Ga_{0.85}As$ (δ_a = 5.714 Å) alloy to be grown on a GaAs substrate (δ_0 = 5.653 Å) the misfit (*f*) is 0.011. $In_{0.15}Ga_{0.85}As$ and GaAs are zinc-blende structures that generate 60^0 interface dislocations with a Burger's vector b = 4 Å and the Poisson's ratio for the $In_{0.15}Ga_{0.85}As$ buffer layer v = 0.316 (all of the values are taken and calculated from Adachi [2.3]). Elastic strain fraction (ε) decay with the increasing thickness of $In_{0.15}Ga_{0.85}As$ epilayer is shown in Fig. 5.2. At ε = 1 the critical thickness is 1070 Å. However MB's model is applicable to multi-layer growths and assumes strain generation via glide mechanism which, as mentioned previously, does not apply to less

than 2% misfit systems and MB noted [5.4] that Eqn. 5.3 predicts 4 times smaller thickness in single layer growths, so it is expected that the $In_{0.15}Ga_{0.85}As/GaAs$ system should allow thicker epilayer growths than 1070 Å. In the next section we analyze the structural and optical properties of the 5-layered intrinsic region of our *p-i-n* QD device.

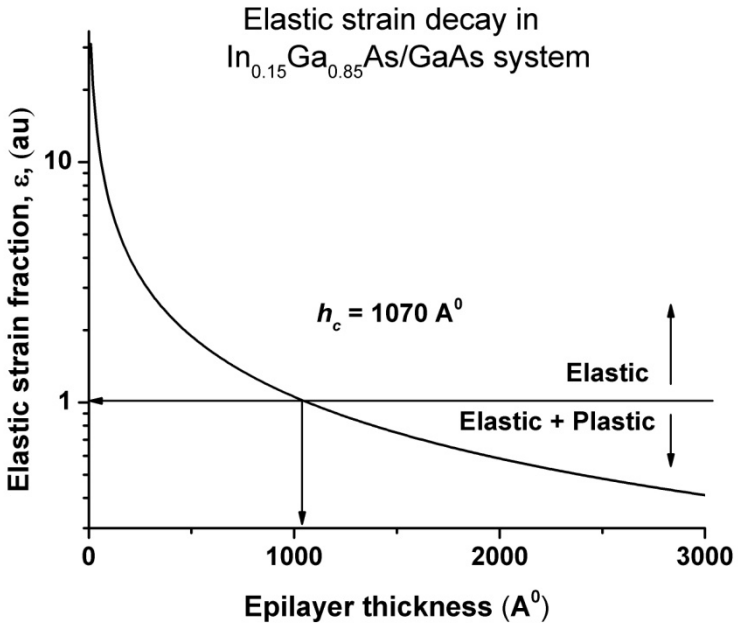

Fig. 5.2 Critical thickness for $In_{0.15}Ga_{0.85}As/GaAs$ system

5.2 Microstructure

5.2.1 Average lattice constant

Epitaxially grown $In_{0.15}Ga_{0.85}As$ (*p*)/InAs(*i*)/$In_{0.15}Ga_{0.85}As$(*n*) quantum dot (QD) device consisted of an intrinsic region with 5 InAs QD layers (single QD layer = 2.1 ML) with each InAs layer grown on an undoped GaAs seed (3 nm) and capped by un-doped $In_{0.15}Ga_{0.85}As$ layer (3 nm). 2.1 ML of un-doped InAs would translate into 6.4 Å, or 0.64 nm however the AFM studies previously have indicated quantum dot heights of 7 ± 1 nm as a result of the Stranski-Krastanov strain release growth mode. Using AFM results the total thickness of one intrinsic layer, *i.e.* seed, island and capping layer together, will measure 13 nm and hence a 5 layered stack will be

65 nm thick. Cross-sectional high resolution transmission electron microscopy measurements (HRTEM), on the other hand, suggested a bit different case for the thickness of intrinsic region, see Fig. 5.3. Each intrinsic region, consisting of a seed, island and capping layer, is marked by arrows along with the direction of growth. It is evident from the HRTEM image that each individual intrinsic layer had a different thickness than the other in spite of the manual efforts to grow as even layers as possible. The variation of layer thicknesses is attributed to (a) manual operation and the related human error and (b) the malfunction of the solenoid operated gallium k-cell shutter which, sometimes, did not close at the first actuation command and had to be re-attempted. Using cross-sectional HRTEM image the stack layers thicknesses were measured with the details outlined in Table 5.1, indicating the total stack thickness as 145 nm. QD *p-i-n* sample was also tested using x-ray diffraction (XRD) method and photoluminescence (PL) spectroscopy as you may recall from Section 4.4 and Figs. 4.12 and 4.13 that noted the existence of intrinsic region. The x-ray data within the 2θ range of $64.4^0 – 65.2^0$ (from Fig. 4.12) and the PL data within 900 – 1200 nm wavelength range (from Fig. 4.13) were curve fitted for Gaussian peak separation using Origin 8.5.1 (student version) and the corresponding results are seen Fig. 5.4. Table 5.2 outlines properties of each individual Gauss peak and the corresponding indium fractions calculated using Vegard's law [2.2] and Madelung's expression for InGaAs band gap [4.21]. Multiple XRD and PL Gaussian peaks are attributed to (1) the phenomenon of interdiffusion between gallium and indium layers to form ternary alloys with elemental compositions other than the intended target structure and (2) biaxial straining of the atoms at each individual interface that changed their lattice constant. Lower indium fraction PL-I peak ($x = 0.14$) is believed to arise from GaAs seed layers that is likely to have some diffused indium content while PL peaks with a higher indium fraction ($x \geq 0.19$) are thought to arise from the top part of an island and the surrounding InGaAs capping layer. A blue-shift of the PL peaks and shifting of the XRD peaks towards $In_{0.15}Ga_{0.85}As$ buffer layer due to lattice straining would predict a lower indium fraction for In-rich InGaAs layers but a higher indium fraction for Ga-rich GaAs layers.

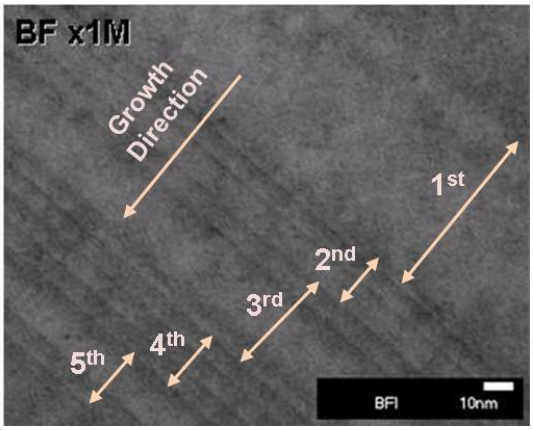

Fig. 5.3 Cross-sectional bright-field HRTEM image showing the intrinsic region of QD device

Table 5.1 Intrinsic layer thicknesses

Intrinsic layer	GaAs (nm)	InAs (nm)	$In_{15}Ga_{85}As$ Cap (nm)
1st	3	10	45
2nd	3	5	10
3rd	6	20	4
4th	5	5	6
5th	15	5	3

In summary we assign indium fractions to individual layers as,

GaAs seed layer = 0.1, δ_1 = 5.694 Å

InAs layer (Island + WL) = 0.4, δ_2 = 5.815 Å

InGaAs cap = 0.2, δ_3 = 5.734 Å

Using this set of layers and the layer thicknesses from Table 5.1, we can calculate the average lattice constant of the intrinsic region using following relation [2.74],

$$\delta_{avg} = \frac{\sum t_i \times \delta_i}{\sum t_i} \tag{5.4}$$

δ_{avg} for the intrinsic region turns out to be 5.75 Å and using Vegard's law the corresponding indium fraction for intrinsic region is 0.24.

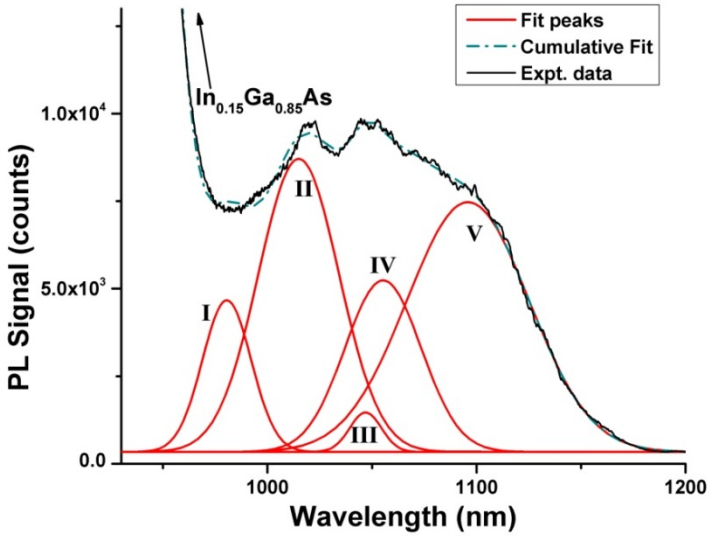

(a)

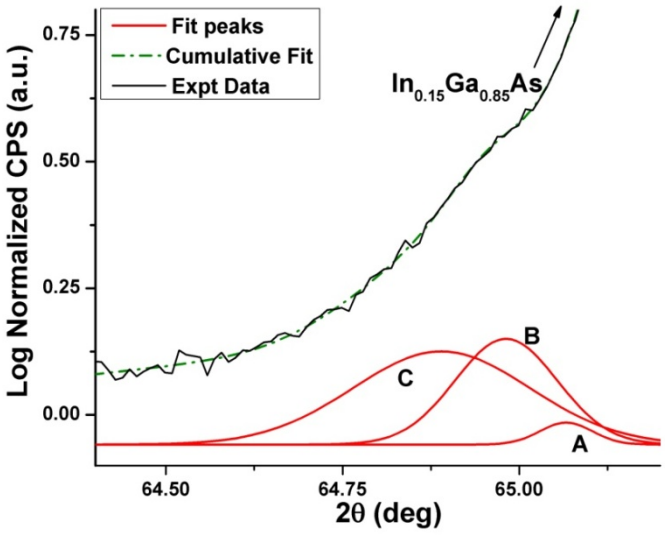

(b)

Fig. 5.4 Intrinsic regions in (a) PL and (b) X-ray spectra with Gaussian peaks

Table 5.2 Properties of Gaussian curves

Peak	Position	Adjusted for Room Temp.	Indium fraction
PL – I	981 nm/ 1.26eV	1.22 eV	0.14
PL – II	1015 nm/ 1.22 eV	1.19 eV	0.16
PL – III	1047 nm/ 1.18 eV	1.15 eV	0.19
PL – IV	1055 nm/ 1.17 eV	1.14 eV	0.2
PL – V	1096 nm/ 1.13 eV	1.1 eV	0.23
XRD – A	65.066^0	-	0.18
XRD – B	64.981^0	-	0.2
XRD - C	64.889^0	-	0.22

5.2.2 Critical thickness of the intrinsic region using MB model

Previously discussed MB model was used to calculate the critical thickness for the epilayer/substrate combination of $In_{0.24}Ga_{0.76}As$ intrinsic region and $In_{0.15}Ga_{0.85}As$ substrate that had misfit strain, *f*, of 0.0063. The Poisson's ratio for the intrinsic region is 0.32 while rest of the mechanical properties for $In_{0.24}Ga_{0.76}As$ layer are assumed similar to $In_{0.15}Ga_{0.85}As$. Fig. 5.5 shows a plot for the decay of elastic strain coefficient as a function of epilayer thickness with critical thickness predicted to be 2050 Å. The cross-sectional HRTEM results, in Fig. 5.6, showed that the total intrinsic layer thickness is 145 nm (1450 A^0) which is less than the MB prediction suggesting complete elastic absorption of the lattice misfit without generation of any dislocations, as HRTEM also shows a lack of any dislocations.

5.2.3 Strain comparison between QD and HOM devices using MB model

Fig. 5.7 shows a strain diagram comparison between (a) QD and (b) HOM samples. In both the samples the $In_{0.15}Ga_{0.85}As$ base layer has a higher lattice constant than the GaAs substrate layer resulting in a total misfit strain, *f*, as 0.011 that makes the base layer to experience compressive straining. For the HOM sample this compressive strain continues from

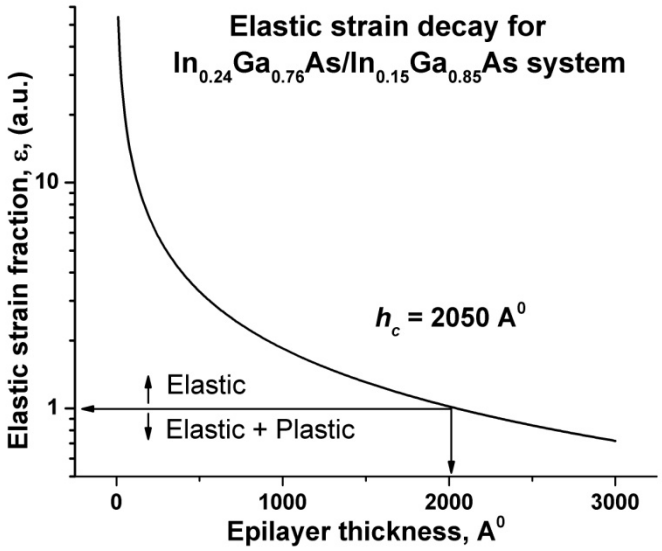

Fig. 5.5 Elastic strain decay in $In_{0.24}Ga_{0.76}As/In_{0.15}Ga_{0.85}As$ epitaxial growth system

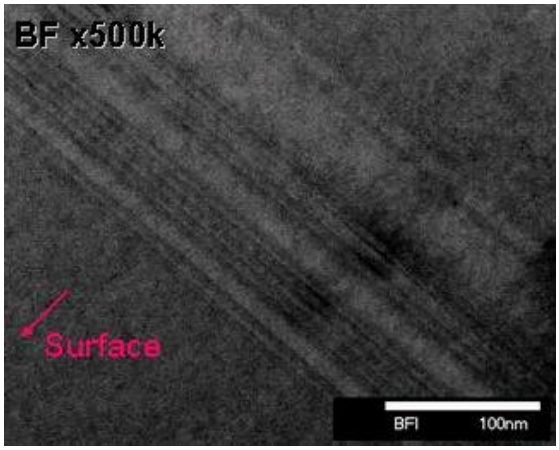

Fig. 5.6 Cross-sectional HRTEM image of QD device showing no evidence of dislocations

the *n*-doped base layer to the *p*-doped top (emitter) layer. This trend of strain continuation is changed for the QD sample due to an added step of incorporation of intrinsic region. Within the intrinsic region the GaAs seed layer experiences tensile strain, InAs layer is compressively strained while $In_{0.15}Ga_{0.85}As$ capping layer undergoes tensile strain. From the average lattice constant calculations, in Section 5.2.1, the intrinsic region lattice constant is 5.75 Å which is

higher than the buffer layer so, cumulatively, the intrinsic region is compressively strained. For the *p*-doped $In_{0.15}Ga_{0.85}As$ top layer in QD device the situation is reverse of the top layer in HOM device. The top layer in QD device has a lower lattice constant compared to the intrinsic region which, now, acts as a substrate subjecting the top layer under tension as opposed to the top layer in HOM sample which is under compression. The top layer/intrinsic region heteroepitaxy is almost identical to the intrinsic/buffer layer scenario, except for the Poisson's ratio which is 0.314 and since the top layer thickness is 200 nm it is within the critical thickness. Strictly adhering to the MB model, the calculated plastic strain in HOM sample is 0.008844 for a total 700 nm thickness. On the other hand the plastic strain in QD device is incorporated only up to the growth of 500 nm base layer, which is 0.0081 since the intrinsic and top layer thicknesses are well within the elastic limits. In comparison the HOM sample incorporated extra $7x10^{-4}$ units of plastic strain (approx. 7.5% of total misfit) than QD sample in the form interface misfit dislocations that could act as free carrier traps but an added step of intrinsic region growth in the QD sample minimized dislocations. Now consider an alternate scenario consisting of the exact intrinsic region growth directly atop a GaAs substrate. This heteroepitaxy would suffer from an increased misfit strain, f = 0.017 (higher than the intrinsic/buffer layer combination by almost a factor of 2) that would translate into a critical thickness of 64 nm which would trigger strain release during the deposition of 3rd intrinsic layer. So theoretically the buffer layer pins down the dislocation generation. Another aspect to be noticed is the strain reversal in the top layer lowering the cumulative strain absorbed in the QD sample compared to HOM sample. Now so far the cross-sectional HRTEM image is the only experimental evidence for QD device along with critical thickness calculations from MB model to support this theory of suppression of dislocations. A direct comparison of experimental data for both QD and HOM samples came from analysis of X-ray curves and the dark-current behavior. Before we compare that set of data, the next section introduces biaxially strained epilayers and their signature in the x-ray diffraction plots.

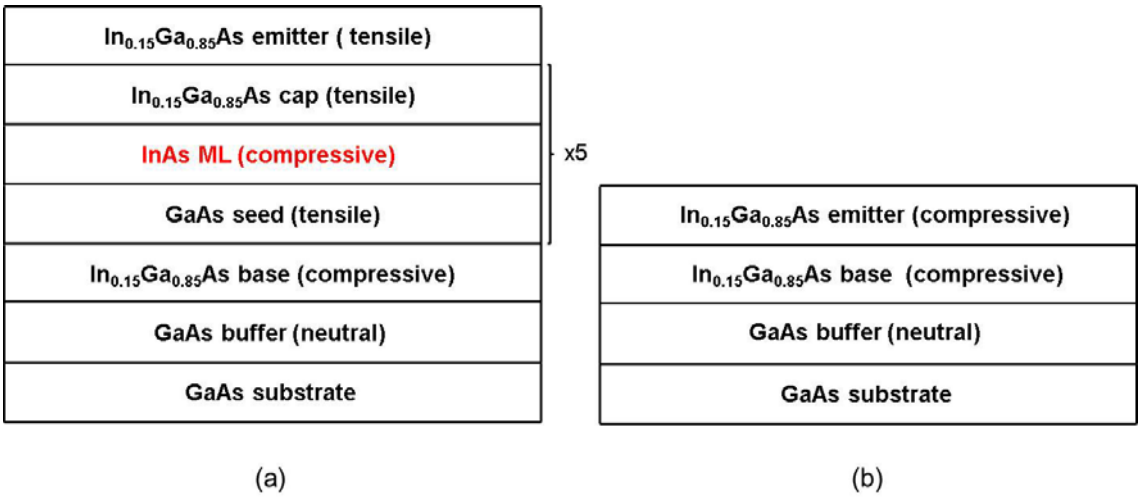

Fig. 5.7 Strain diagram of (a) HOM and (b) QD sample

5.3 Misfit Variation Analysis

5.3.1 Evidence of pseudo InGaAs layer

Four samples were grown using MBE that had 500 nm of InGaAs layers atop a GaAs (001) substrate with increasing indium content from 14 % to 30 %. Those samples were labeled Z680 (14%), Z677 (18%), Z678 (24%) and Z679 (30%), see Appendix A, with the corresponding misfit as, 1%, 1.3%, 1.7% and 2.2%; respectively. Fig. 5.8 shows the X-ray curves for all of the samples normalized against GaAs substrate peak at 66.02^0. The InGaAs peaks were registered at decreasing 2θ values as the indium content increased. For all of the samples a small 'bump' was registered at approx. 65.7^0 which when expanded looked like the inset in Fig. 5.8. Notice the change of y-axis scale from normal to logarithmic. The curves in the inset are a result of diffraction from (004) planes of the part of the epilayer in the vicinity of interface which is bi-axially strained prior to the existence of targeted lattice constant. To reminisce, the InGaAs layers are grown by keeping the indium, gallium and arsenic shutters open and maintaining the k-cell temperatures constant so that there is no possibility of indium content variation during each buffer layer growth. What can be seen from the inset is that the sample with 1% misfit shows highest peak emerging from strained lattice while the rest of the samples show some

reduction in the peak height as the misfit increases. Amongst rest of the three samples the peak intensity increases a bit as the misfit increases from 1.3 to 2.2%. Also can be noticed from the main plot is the reduction in InGaAs peak intensity as the misfit increases from 1 to 1.7 but for higher misfit it increases again. To study this trend the pseudo regions from each sample are analyzed in the next section.

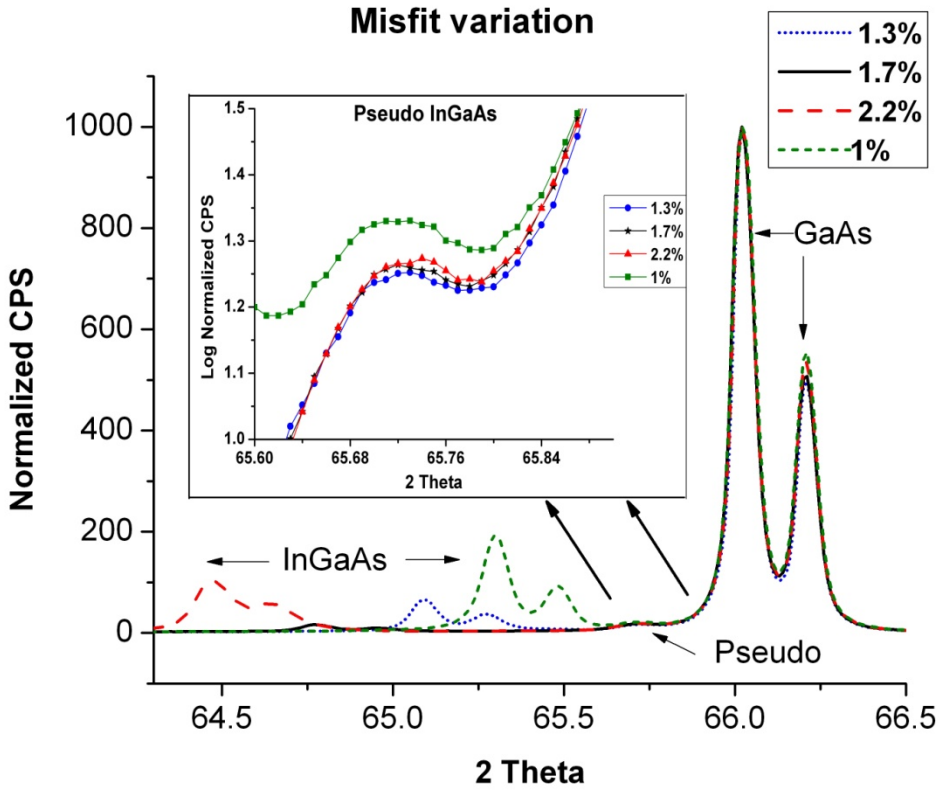

Fig. 5.8 X-ray curves for samples with misfit variation

5.3.2 Strain release signature in pseudo layers

Each X-ray plot in Fig 5.8 was analyzed using Gaussian curve fitting using Origin software. An example of this curve fitting is seen in Fig. 5.9 that shows logarithmic counts per second vs. 2θ plot for 1% misfit sample. The 'bump' in the normalized CPS plot in Fig. 5.8 was enhanced by taking a logarithm of CPS and then each individual peak was selected for Gaussian fitting

procedure with a baseline value of 1 so that the intensity of resultant GaAs and InGaAs Gaussian peaks were as close as possible to the experimental data. The pseudo peaks occurred at 65.73 (peak-1) and 65.89 (peak-2) degrees resembling elastically and plastically strained epilayers, respectively, that reside in the vicinity of the interface. Recalling Fig. 2.4 when the stored elastic strain energy exceeds the energy of misfit dislocation generation then it releases the stored strain energy by breaking an atomic bond at the epilayer-substrate interface forming a biaxially strained epilayer with a lattice constant slightly lower (departure towards GaAs lattice constant) than the elastically strained epilayer. Hence the positions of peaks 1 and 2 translate into higher and lower lattice constants that resemble elastically and plastically strained pseudo layers, respectively. Using similar curve fitting procedure pseudo peaks 1 and 2 were generated for higher misfit samples and a comparison of all of the Gaussian peaks is seen in Fig. 5.10. The legend designates the curves for each set of misfit Gauss peaks and Table 5.3 outlines the peak positions and heights. For all of the samples the positions of peak 1 remained within 0.008 deg. and those of peak 2 within 0.007 deg. suggesting no significant trend. On the other hand a variation in the intensity of both the peaks did exhibit a trend. The intensity of peak-1 reduced as the misfit increased from 1 to 1.3 which is attributed to the reduction in the volume of the higher lattice constant pseudo layer as the epilayer experienced an increment in the misfit and released it by generating dislocations. In other words, higher misfit resulted in a lower h_c so for identical buffer layer thicknesses the higher misfit sample generated more dislocations which increased the volume of the pseudo layer that housed defects which is duplicated as an increment in the intensity of peak-2. From 1.3 to 1.7% of misfit change, the peak-2 intensity increases significantly. This suggests enhanced strain release with 1.7% misfit. Peak-2 for 1.7% exhibited maximum intensity amongst all of the samples suggesting maximum absorption of misfit strain via a combination of elastic and plastic straining which was replicated as the weakest InGaAs peak intensity in the main plot of Fig. 5.8. For 2.2 % misfit the peak 1 remains relatively unchanged while peak-2 height reduces below that of 1.3% misfit. However we see in Fig. 5.8 that the main InGaAs peak intensity for 2.2%

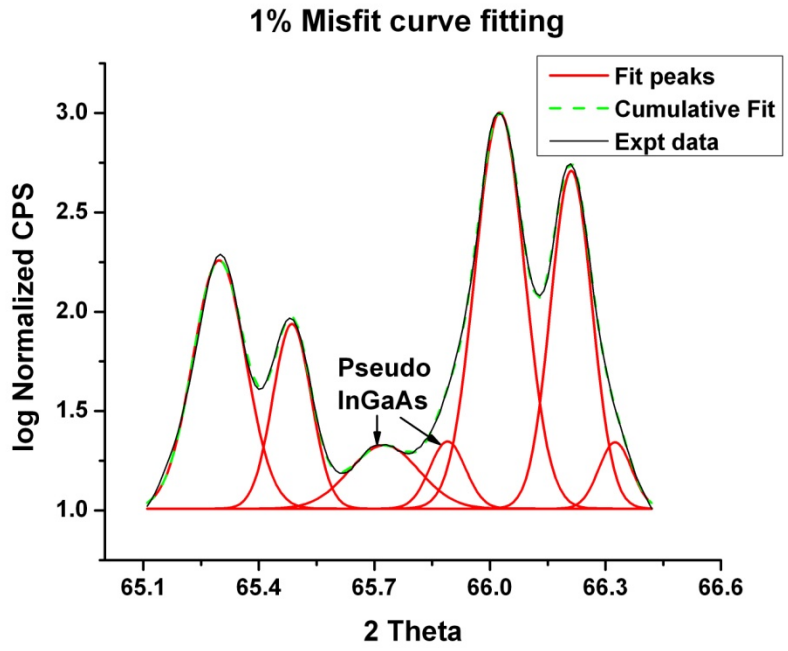

Fig. 5.9 Curve fitting of XRD data of 1% misfit sample

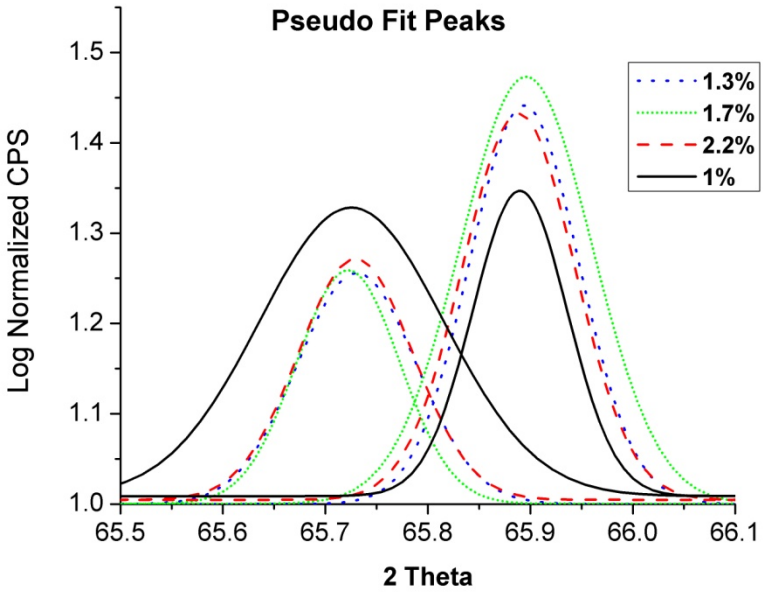

Fig. 5.10 Comparison of pseudo fit peaks as a function of misfits

misfit sample was increased as the indium fraction increased. Meaning the InGaAs epilayer in sample Z679 released a substantial amount of strain via interface dislocation generation and an additional mechanism that led to the emergence of a relaxed buffer layer with the intended stoichiometry. It has been observed in the literature that for an InGaAs/GaAs epitaxial growth system with indium content < 30% the process follows a 2 dimensional (2D) epilayer growth but beyond 30%, which is for misfit ≥ 2.1%, the epitaxial growth follows a 3 dimensional (3D) growth mechanism [1.2] generating edge type dislocations. These dislocations have burger's vector as ½d <110> and possess (001) <110> slip system making them sessile. It is worth noting that such dislocations have longer range of strain field but reduce the misfit strain considerably so that the epilayer with high misfit is relaxed at an early stage of growth. Generation of edge dislocations is thought to be a result of coalescence of 3D islands in some cases [2.37] while in other cases it is thought to be a result of the interaction between interface misfit dislocations and bending of misfit dislocations [2.37]. We recorded evidence of such threading dislocation during the growth of sample Z683 (Appendix A). This sample was a *p-i-n* diode with almost identical QD growth conditions as QD device (Z682) except the capping layer had 30% of InAs, as opposed to 15% in QD device. This growth was an attempt to reduce the lattice constant from InAs QD layer to the next GaAs seeding layer by incorporating $In_{0.3}Ga_{0.7}As$ cap that would gradually reduce the misfit compared to an abrupt change from InAs to $In_{0.15}Ga_{0.85}As$. Both the devices were fabricated into TEM samples and characterized using HRTEM, see Fig. 5.11. Clearly the inclusion of $In_{0.3}Ga_{0.7}As$ capping layer generated high density of threading dislocations that lied at 45^0 to the growth direction and continued in the top emitter layer. RHEED images for this samples exhibited diffused pattern doe to uneven growth fronts. This transformation of growth mode from 2D to 3D is expected to have occurred in the sample with 2.2 % misift. A signature of the edge type threading dislocations is hard to resolve in XRD plots because the epilayer in the vicinity of the threading dislocation is relaxed to the intended alloy lattice constant but we can reasonably infer strain relaxation by the re-emergence of the InGaAs buffer layer peak, which was almost invisible for 1.7% misfit.

Table 5.3 Properties of pseudo peaks as a function of misfit

Peak	Misfit	Position (deg)	Height (au)	Dislocation type
1	1%	65.725	0.320	60^0
	1.3%	65.730	0.256	60^0
	1.7%	65.722	0.259	60^0
	2.2%	65.729	0.267	60^0, edge
2	1%	65.889	0.338	60^0
	1.3%	65.893	0.441	60^0
	1.7%	65.895	0.473	60^0
	2.2%	65.888	0.428	60^0, edge

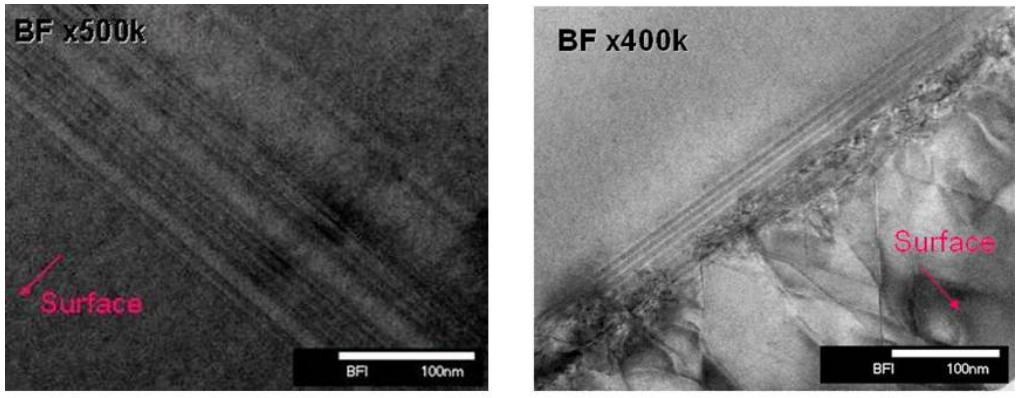

Fig. 5.11 Capping layer growth comparison as (a) 2D with $In_{0.15}Ga_{0.85}As$ and (b) 3D with $In_{0.3}Ga_{0.7}As$

5.4 Strain Release Comparison between QD and HOM Samples

The Gaussian curve fitting procedure was also conducted for QD and HOM samples. Fig. 5.12 shows normalized CPS vs. 2θ plots for QD (solid) and HOM (dash) devices with a similar bump, as seen previously, recorded at around 65.7^0 which is zoomed into the inset as log normalized CPS vs. 2θ plot. The logarithmic CPS vs. 2θ plot was separated into individual

Gaussian peaks against a log CPS baseline value of 1.2 and the resultant peaks are compared in Fig. 5.13 and the peak properties are outlined in Table 5.4. The peak-1 positions were within 0.004^0 and peak-2 within 0.005^0 of difference, respectively, between the QD and HOM samples. The intensity of peak-1 reduced slightly from QD to HOM sample indicating elastic strain release while corresponding peak-2 intensity recorded a considerable increment in HOM sample indicating higher volume of the pseudo layer with interface defects, compared to QD sample. This analytical data confirms the previous theoretical calculations that the QD sample minimizes generation of dislocations.

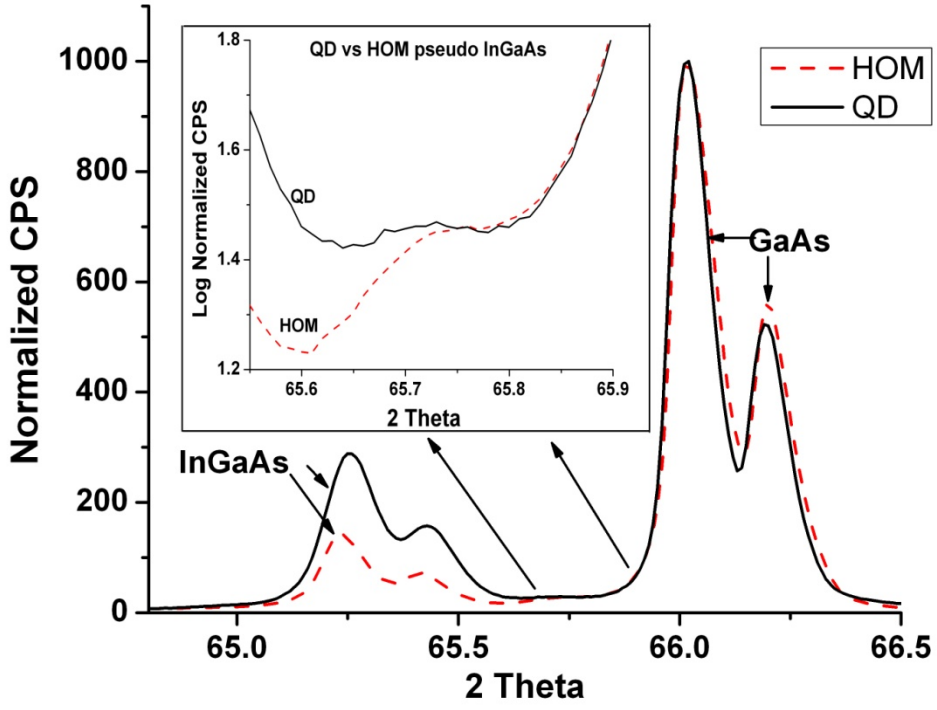

Fig. 5.12 X-ray peaks for QD and HOM sample

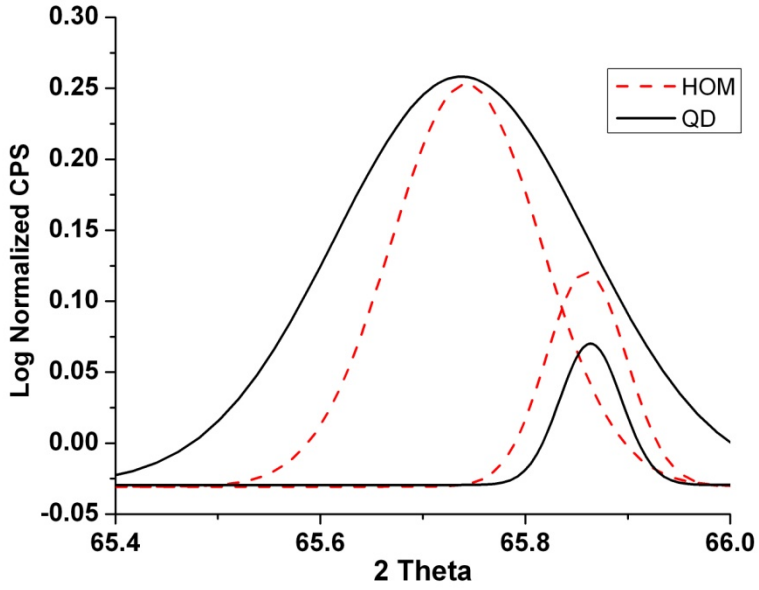

Fig. 5.13 Comparison of Gauss peaks resembling pseudo regions in QD and HOM samples

Table 5.4 Gaussian peaks from QD and HOM samples

Peak	Sample	Position	Height (au)	Dislocation type
1	QD	65.738	0.288	60^0
	HOM	65.742	0.283	60^0
2	QD	65.864	0.099	60^0
	HOM	65.859	0.151	60^0

5.5 Current-Voltage Measurements for QD and HOM Samples

Discussion in the previous section and the misfit strain releases calculations have shown that the quantum dot sample has minimized the generation of dislocations compared to its counterpart homojunction device, made up of the barrier material without any intrinsic region. To conduct a current-voltage performance characterization the QD and HOM samples were fabricated using lithography, etching and sputtering, as described in Chapter 3, into a set of devices with Pt contacts on base and top layers, see Fig. 5.14. The samples were tested for

diode behavior using a four-probe tool without any illumination and the results are shown in Fig. 5.15. The data shows a stark reduction in the QD dark current compared to the HOM device. Recalling the expressions for radiative (J_{rad}) and non-radiative (Shockley-Hall-Read, J_{SHR}) current densities in a diode [2.67, 2.68],

$$J_{rad} = J_0\left[e^{\frac{qV}{kT}-1}\right] \tag{2.25}$$

$$J_{SHR} = \frac{qn_iW}{\sqrt{\tau_n\tau_p}}\left(e^{\frac{qV}{2kT}}-1\right) \tag{2.27}$$

Where V is the applied bias, W is the space charge width, n_i is the intrinsic carrier density, k is the Boltzmann's constant, τ_n and τ_p are electron and hole lifetimes, T is the substrate temperature and J_0 is the reverse saturation current. J_{SHR} represents the current by non-radiative recombination as a result of trapping of the free carriers at the defect sites which along with J_{rad} forms the total dark current as,

$$J_{dark} = J_0e^{\frac{qV}{nkT}} \tag{2.28}$$

where 'n' is the ideality factor for a device. For n values close to 1 a device is radiatively dominated while a device that is non-radiatively dominated results into higher values of n. It should be noted that higher the contribution from non-radiative current in a diode higher will be the total dark current. When applied to the experimental evidence of dark current behaviors of QD and HOM samples we can infer that higher dark current from the HOM structure is attributable to the growth of top layer that continues to suffer compressive strain, same as the base layer, and releases the misfit strain by generating extra defects. The QD device, on the other hand, generates defects only during the growth of the base layer and once the kinetics of growth are changed for deposition of the intrinsic layers then the base layer in QD sample acts

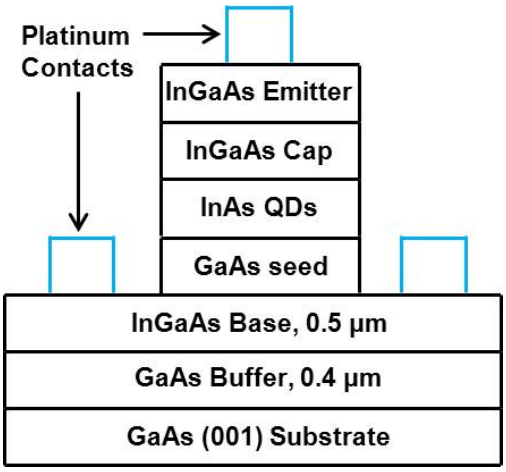

Fig. 5.14 Device structure after lithography, etching and metal deposition

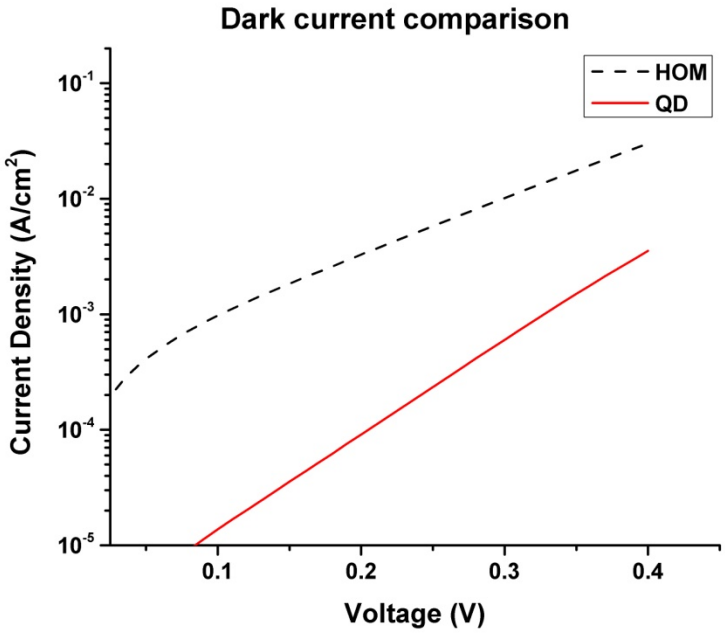

Fig. 5.15 Dark current comparison

as a substrate that imposes a lower lattice misfit towards the intrinsic region setting a higher strain release threshold. The thickness of the intrinsic region remains lower than the critical thickness predicted by Matthews-Blakeslee [5.2] and once again when the kinetics are changed

for the top layer growth then this layer suffer from tensile strain, as opposed to compression in the HOM, and the top layer thickness, lower than h_c, does not trigger any dislocations in that layer. Dark current behavior shown in Fig. 5.15 came as a surprise during the course of this work that warranted a further review of growth conditions, electron microscopy characterizations, PL spectroscopy and especially X-ray data which exhibited a signature of the biaxially strained pseudomorphic layers, with higher and lower lattice constants, respectively; representing elastic and defective regions in the vicinity of epilayer-substrate interface, that helped understand improved strain build-up within the QD device compared to HOM.

5.6 A Comparison of the Method of Buffer Layer Growth to Previous Attempts at Dislocation Reduction

In the past there have been attempts at reducing dislocations in the lattice mismatched epitaxial growths that consisted of,

a. Substrate patterning [2.38, 2.39]: This method used a mesa patterned substrate that allowed heteroepitaxial growth of small sized structures that imposed a shorter dislocation glide length to exit at the sample edge so that the probability of dislocations interactions, responsible for the generation of sessile edge dislocations, were lowered. This method suffered from a drawback that it shortened the active device area making it unsuitable for optoelectronic applications, such as photovoltaic devices. Moreover the presumption of glide mechanism is under doubt [5.3] and is not a widely accepted phenomenon in the scientific community affecting acceptance of this method.

b. Strained-layer superlattice [2.33]: This method employed a deposition step of few nanometer thick layer of a material with a significant lattice mismatch to the underlying substrate in an attempt to trigger the dislocation glide. This method, unfortunately, was successful in lowering dislocation density

only by 5 – 10% and actually was responsible for enhanced dislocation interactions to generate edge-type defects.

c. Compositional grading [2.40]: This method involved epitaxial deposition of an alloy compositionally graded (CG) at the rate of, *e.g.*, 0.1 (elemental fraction) per μm thickness on a lattice mismatched substrate. Due to low misfit at each step of grading the possibility of high strain release build-up was reduced drastically. A drawback for this method is the necessity to grow thick layers that require long times making this technique inefficient, plus thick compositionally graded layers invited a moderate to significant compromise on the freedom of band gap design, which actually is an expected asset of lattice mismatched systems.

d. Strain balancing [2.73]: To surpass the Shockley-Queisser solar cell efficiency limit [2.71] quantum dots based *p-i-n* devices have been proposed [2.72, 2.73] that would absorb solar irradiation in a wider range than a single band gap structure thereby enhancing the carriersdensity and eventually the photovoltaic efficiency. The proposed design employed low dimensional low band gap structures to be sandwiched within the intrinsic region. The work in the field of QD based *p-i-n* devices is currently in its infancy as it tries to minimize dislocations within the intrinsic region generated as a result of lattice misfit between quantum dot structures and the matrix. Lately strain-balancing method has been employed which consisted of InAs QD island capping by an alloy that had a lattice constant less the underlying GaAs substrate. By selecting appropriate thickness of the capping layer strain balancing attempts to match the average lattice constant of the intrinsic region as close as possible to the GaAs substrate so that the total misfit is almost zero. As mentioned in Chapter 2, this method has shown some improvement [2.76] in enhancing the short circuit

current density (J_{sc}) compared to a control *p-n* device made up of the barrier material. However strain balancing has shown higher dark current compared to the *p-n* control device suggesting defect generations in spite of substrate lattice constant matching.

In the wake of the drawbacks of those aforementioned defect reduction methods our approach of buffer layer growth establishes following advantages:

1. Simplicity: The buffer layer method requires deposition of an epilayer with an intermediate lattice constant that would act as a substrate with a lower lattice misfit for the subsequent intrinsic region growths. This aspect discards the complications involved in the strain balancing approach like employing more than three elements for the entire growth mode [2.76, 2.78].
2. Efficient device fabrication: The thickness of the buffer layer in our QD sample was 0.5 μm and it was sufficient to form a substrate with a closer lattice constant to the intrinsic layers. This aspect overcomes the inefficient time considerations encountered during compositional grading method.
3. Band gap freedom: The buffer layer growth might affect band gap design freedom in a minor to negligible degree but definitely would provide more freedom than compositional grading.
4. Better thermal stress management: By incorporating closely matched lattice alloy compositions the entire device can withstand thermal stress for a broader range of device growth temperatures. This is advantageous overstrain balancing method that incorporates drastically different intrinsic region elements with different thermal expansion co-efficients that would enhance the thermal stress gradient within the adjacent layers making it unsuitable for wider substrate temperature kinetics.
5. Easier assessment of strain build-up: This aspect of the buffer layer method is a key advantage over all of the previous methods, especially strain balancing. Strain balancing approach attempts to pre-assess the average lattice constant of the

intrinsic region prior to the growth and given the anisotropic nature of the structure and morphology of quantum dot islands it is very difficult to anticipate the strain build-up. Plus in an attempt to keep the lattice constant of the capping layer lower than the substrate it actually introduces significant misfit strain between islands and the capping layer that bolsters the interdiffusion phenomenon [4.14 – 4.16] thereby forming ternary and quaternary alloys. In the buffer layer growth method the capping layer had the same alloy composition as the buffer layer because the misfit strain that triggers the dislocation generation had already been lowered. The buffer layer method acknowledged the limitations over the anticipation of strain build up in the intrinsic region and solved the problem of high misfit before the islands were deposited.

6. First instance of dark current reduction: To our knowledge there has been no report of dark current reduction in a lattice mismatched QD based *p-i-n* device compared to its counterpart *p-n* device made up of the barrier material. As far as the current understanding of strain release and critical thickness behavior goes the QD device incorporated more misfit strain compared to HOM device and intuitively would have generated more dislocations. However we witnessed a contradictory behavior since the QD device managed to absorb the misfit on an account of buffer layer incorporation and managed to pin down dislocation generation phenomenon.

In summary, we have realized an innovative method to successfully grow a QD based *p-i-n* diode structure that minimized the generation of dislocations compared to its counterpart *p-n* structure. The current-voltage measurements under illumination conditions were conducted on both the devices and the QD device showed a higher open circuit voltage (V_{oc}) compared to the HOM device and is presented in Chapter 6. A thorough analysis of those results is beyond the scope of this work, instead we provide a set of directions as a future work for photocurrent behavior analysis.

CHAPTER 6

CONCLUSIONS AND FUTURE WORK

6.1 Conclusions

We have presented a new growth method that can minimize dislocations in a semiconductor quantum dots based *p-i-*n diode structure that can incorporate higher lattice strain compared to a *p*-n structure without quantum dots. To our knowledge this is the first time a QD based *p-i-n* device has shown lower dark current than the corresponding *p-n* control device made up of the barrier material.

The *p-i-n* diode structure consisting of an intrinsic region, with 5 layers of 2.1 monolayer (ML) indium arsenide (InAs) incorporated between $In_{0.15}Ga_{0.85}As$ (*p*) and (*n*) layers, atop a gallium arsenide substrate, was grown using an ultra-high vacuum molecular beam epitaxy tool. The InAs ML absorbed a lattice misfit of approx. 7.2% which was released by forming islands by Stranski-Krastanov self-assembly method. By optimizing the kinetics of epitaxial growth we were able to fabricate 35 ± 3 nm sized, high density (2.5×10^{10} per cm^2) InAs quantum dots that exhibited pyramidal/dome shapes of 7 ± 1nm heights. Low temperature (6K) photoluminescence (PL) characterization recorded photon activity at 1300 nm wavelength which was analyzed and determined to be emerging from strain released top portion of the islands that formed atomic like discrete density of states with an e^1-hh^1 transition energy of approx. 0.885 eV. A *p-n* device (HOM) was fabricated by epitaxial deposition of *p* and *n*-doped $In_{0.15}Ga_{0.85}As$ layers without any quantum dots. The QD and HOM samples were tested using x-ray diffraction and PL methods. X-ray data was used to calculate the indium fraction in the base and top InGaAs layers, which was 0.145 and 0.152 for QD and HOM samples respectively. X-ray and PL data resembling the intrinsic region in QD sample were analyzed to calculate the average lattice constant of intrinsic region as 5.75 Å.

The x-ray data exhibited a signature of the strain release mechanism for InGaAs base layer by recording a set of intermediate peaks resulting from (004) Brag diffractions off of the elastically strained and plastically relaxed sections of the base layer in the vicinity of base-substrate interface. A set of buffer layer growths with an increasing lattice misfit exhibited a reduction in the intensity of the peak corresponding to the elastic region and an enhancement of the intensity for the pseudo peak resembling the plastically relaxed region. This analytical data suggested elastic strain release by breaking off atomic bonds in the vicinity of the interface. A similar x-ray characterization was performed for QD and HOM samples. The QD sample exhibited incorporation of higher elastic strain compared to HOM sample, even though HOM sample was set to a lower lattice misfit atop the GaAs substrate. The increased number of defects in the HOM device acted as free carrier traps thereby recording higher dark (leakage) currents compared to QD device. This analysis, along with the cross-sectional transmission electron microscopy images, helped formulate a new method of epitaxial growth that could control the strain build-up better than the previously reported methods. The incorporation of buffer layer reduces the total misfit experienced by intrinsic region with advantages such as simplicity, fabrication efficiency, a minor to negligible compromise over band gap freedom, enhanced thermal stress management and a better assessment of strain build-up.

6.2 Future Work

The QD and HOM samples were fabricated using lithography, etching and metal deposition methods into a device to be used for current-voltage measurements, see Fig. 5.14. It is to be noted that HOM device had identical epitaxial layers as the QD sample, except without any intrinsic region. Those two devices were tested under 850, 950 and 1300 nm radiations by using an optical filter over an atomic mass zero (AM0) light source used for a four-probe testing tool. The results of those tests are seen in Figs. 6.1 – 6.3. The short circuit current density, J_{sc} and open circuit voltage, V_{oc}, under all of the three illumination conditions are outlined in Table 6.1. The photocurrent behavior under 850 nm illumination is attributable to photon absorption by InGaAs base and emitter (top) layers in both the samples while under 950 nm illumination

conditions HOM device showed a negligible photocurrent activity whereas the intrinsic region of the QD device contributed towards the recorded photocurrent behavior. The QD sample showed photon activity under long infrared conditions with J_{sc} of 0.16 μA/cm^2 and a. V_{oc} of 0.012 V. Recalling a discussion in Chapter 4 regarding PL spectra at approx. 1400 nm wavelength this long IR photocurrent would seem to be related to the quantum confined free carriers within the InAs islands. However an interesting result is recorded as an enhancement of open circuit voltage in the QD device compared to the HOM sample, under near infrared illumination conditions. This behavior has not been witnessed in the literature and using superposition approximation, Eqn. 2.29, it can be attributed to the reduced dislocations within the QD device compared to HOM, which resulted in a lower leakage current. But at the same time the J_{sc} in HOM sample is higher than J_{sc} of the QD device by a factor of 10. Both of these results are contradictory to the proposed theories of low-dimensional devices since they predict that (a) the short circuit current increases due to higher free carrier density and (b) the open circuit voltage is set by the higher band gap matrix material [2.79]. Moreover the mechanism of excitation of trapped free carriers is unclear. Another thing to be noted is the 'dips' seen in the I-V data for QD device under long infra-red illuminations, at applied bias of -0.035, 0.01 and 0.04 V. Those peaks were not recorded under dark conditions suggesting an unknown behavior related to excitation of quantum confined free carriers. Unfortunately, at this point of time there is no definite analysis that can explain all of those recorded behaviors although we speculate either tunneling of carriers through adjacent layers eventually into the matrix or a phonon assisted excitation of trapped carriers to overcome the restrictions imposed by matrix band gap. As far as the current understanding goes two types of characterizations could be performed as a future work, *viz.* (1) setting a constant bias and testing the photocurrent over a period of time to check for applied bias dependency that may provide an insight into coupling of wave functions within adjacent layers that could assist tunneling and (2) testing the photocurrent behavior by heating the sample over a range of temperatures to find out a relation, if there is any, between

phonons and confined carriers. Also the enhancement of V_{oc} and reduction of J_{sc} needs a review of the physics of quantum dots based devices.

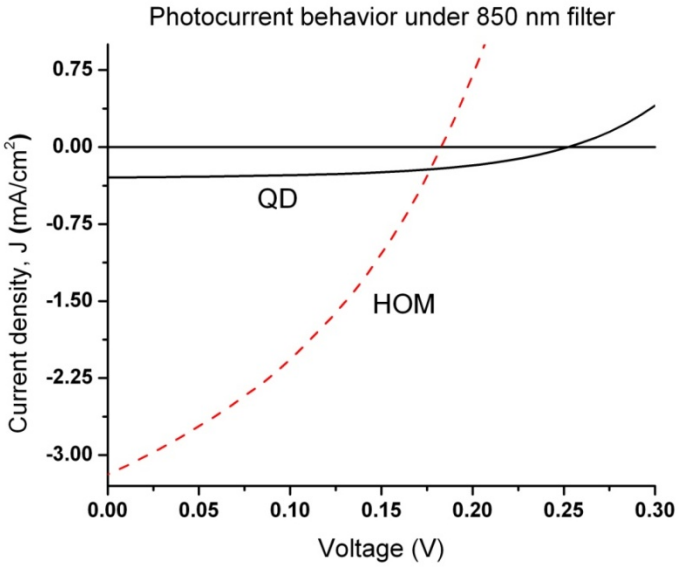

Fig. 6.1 Photocurrent behavior under 850 nm illumination

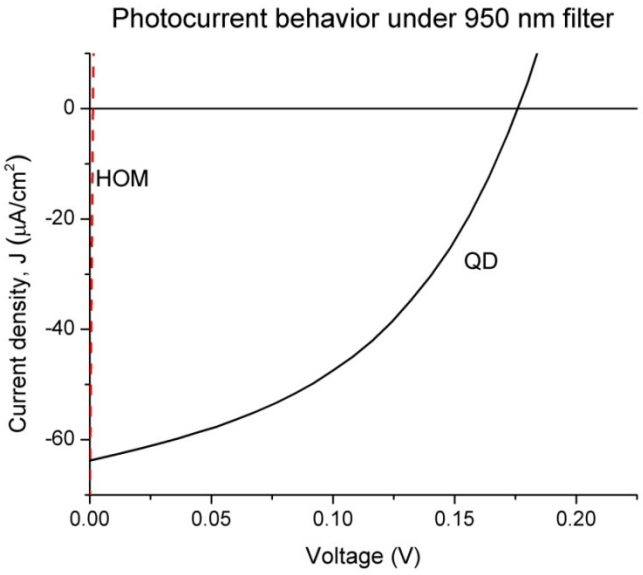

Fig. 6.2 Photocurrent behavior under 950 nm illumination

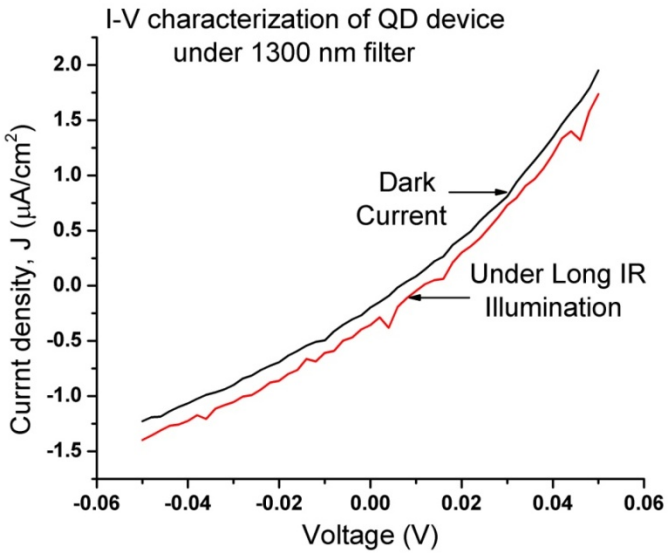

Fig. 6.3 Photocurrent behavior of QD device under long infrared illumination

Table 6.1 Photocurrent performance of QD and HOM samples under various illumination conditions.

Filter	Sample	J_{sc}	V_{oc}
850 nm	QD	0.29 mA/cm^2	0.25 V
	HOM	3.16 mA/cm^2	0.18 V
950 nm	QD	63.5 μA/cm^2	0.18 V
	HOM	294 μA/cm^2	0.004 V
1300 nm	QD	0.35 μA/cm^2	0.012 V

APPENDIX A

EPITAXIAL GROWTH PARAMETERS FOR VARIOUS SAMPLES

Sample No.	Substrate Temperature ^{0}C	In/Ga BEP ratio	As/In+Ga BEP ratio	In (%) in buffer layer	InAs growth rate (Å/sec, ML/sec)	InAs deposition (ML)
	GaAs /InGaAs/InAs					
Z653	550/-/345	0.387	19.9	23.37	N/A	None
Z655	550/340/550	0.22	9.71	N/A	N/A	3.4
Z659	600/450/530	0.171	20.8	11.32	N/A	None
Z663	600/-/-	0.193	13.5	15.2	N/A	None
Z664	600/450/-	0.152	22.22	10.27	N/A	None
Z665	600/450/-	0.218	14.49	14.2	0.195, 0.063	2.9
Z667	600/450/530	0.2179	14.06	13.8	0.195, 0.063	2.9
Z669	600/450/530	-	-	14.14	0.195, 0.063	2.9
Z673	600/450/-	0.219	14	13.94	0.195, 0.063	None
Z677	600/450/530	0.282	17.52	16.97	0.22, 0.073	2.5
Z678	600/450/530	0.421	15.82	22.94	0.36, 0.121	3
Z679	600/450/530	0.579	14.22	28.56	0.48, 0.16	2.72
Z680	600/450/530	0.216	17.76	14.5	0.16, 0.054	2.1
Z682	600/450/530	0.216	17.76	14.5	0.16, 0.054	2.1
Z683	600/450/530	0.216, 0.579	17.76, 14.22	14.5	0.16, 0.054/0.48, 0.16	2.1
Z688	600/450/530	0.25	16.14	16.1	0.248, 0.08	3.2
Z690	600/450/-	0.25	16.14	16.05	0.248, 0.08	3.2

REFERENCES

CHAPTER 1

1 E. A. Fitzgerald, 'Dislocations in strained-layer epitaxy: Theory, experiment and applications', Mat. Sci. Rep., 7 1991, p 87

2 J. W. Matthews, A. E. Blakeslee; 'Defects in epitaxial multilayers I: Misfit dislocations', J. Cryst. Gr., 27, 1974, p 118

3 T. Suzuki, S. Takeuchi, H. Yoshinga; 'Dislocation dynamics and plasticity', Springer series in Mat. Sci., Springer-Verlag Berlin Heidelberg, 1991, p 1

4 F. C. Frank, J. H. Van der Merwe; 'One dimensional dislocations I: Static theory', Proc. Roy. Soc. A, 198, 1949, p 205

5 G. E. Moore, 'Cramming more components onto integrated circuits', Electronics, 38 (8), 1965

6 V. A. Shchukin, N. N. Ledenstov, D. Bimberg; 'Epitaxy of Nanostructures', Springer, 2004, p 3

7 R. F. C. Farrow, 'Molecular Beam Epitaxy – Application to key materials', Noyes Publications, p 2

8 J. F. Nye, 'Physical properties of Crystals', Clarendon, Oxford, 1972

9 V. A. Shchukin, N. N. Ledenstov, D. Bimberg, Epitaxy of Nanostructures, Springer, 2004, p 167

10 N. N. Ledenstov, M. Grundman, N. Kirstaedter, O. Schmidt, R. Heitz, J. Bohrer, D. Bimberg, V. M. Ustinov, V. A. Schchukin, P. S. Kopev, Zh. I. Alferov, S. S. Ruvimov, A. O. Kosogov, P. Werner, U. Richter, U. Gosele, J. Heydenreich, Proceedings of the 7th

11 International Conference on Modulated Semiconductor Structures, Madrid, Spain, 1995, Solid State Elect, 40, 1996, p 785

12 Inst. Mater. Re. & Eng., Agency for Science, Technology & Research, Singapore, newsletter 2005

13 S. M. Hubbard, C. G. Bailey, C. D. Cress, S. Polly, J. Clark, D. V. Forbes, R. P. Raffaelle, S. G. Bailey, D. M. Wilt, 'Short circuit current enhancement of GaAs solar cells using strain compensated InAs quantum dots', 33rd IEEE Photovoltaic specialist conference proceedings, San Diego, 2008

14 R. Oshima, Y. Nakamura, A. Takata, Y. Okada; 'Multi-stacked InAs/GaNAs strain compensated quantum dot solar cells', 22nd EU-PVSEC, Milan, 2007

15 C. G. Bailey, S. M Hubbard, D. V. Forbes, R. P. Raffaelle; 'Evaluation of strain balancing layer thickness for InAs/GaAs quantum dot arrays using high resolution x-ray diffraction and photoluminescence', Appl. Phys. Lett., 95, 2009, p 203110

16 R. Beanland, J. P. R. David, A. M. Sanchez; 'Quantum dots in strained layers – preventing relaxation through the precipitate hardening effect', J. Appl. Phys., 104, 2008, p 123502

17 T. Asano, Z. Fang, A. Madhukar; 'Deep levels in GaAs (001)/InAs/InGaAs/GaAs self-assembled quantum dot structures and their effect on quantum dot devices', J. Appl. Phys., 107, 2010, p 073111

CHAPTER 2

1 http://www.tf.uni-kiel.de/matwis/amat/semi_en/kap_5/backbone/r5_1_4.html

2 L. Vegard, Z. Phys., 5, 1921, p 17

3 S. Adachi, 'Physical properties of III-V semiconductor compounds', John Wiley & Sons, 1992, p 79

4 U. Dehlinger, 'Zur Theorie der Rekristallisation reiner Metalle', Annln. Phys., 2, 1929, p 749

5 F. C. Frank, J. H. Van der Merwe; ‘One dimensional dislocations I: Static theory’, Proc. Roy. Soc. A, 198, 1949, p 205

6 J. Frenkel, T. Kontorova; ‘On the theory of plastic deformation and twinning’, J. Phys. 1, 1939, p 137

7 F. C. Frank, J. H. Van der Merwe; ‘One dimensional dislocations III: Influence of the second harmonic term in the potential representation, on the properties of the model’, Proc. Roy. Soc. A, 200, 1949, p 125

8 J. H. Van der Merwe, ‘Crystal interfaces. Part I. Semi-infinite crystals’, J. Appl. Phys., 34, 1964, p 117

9 J. W. Matthews, ‘Accommodation of misfit across the interface between single-crystal films of various face-centered cubic metals', Phi’. Mag., 13, 1966, p 1207

10 N. Cabrera, Memoires Scientifiques Rev. Metallurgy, 62, 1965, p 205

11 J. W. Matthews, Epitaxial growth, Part B; Academic Press, New York, 1975

12 L J. A. M. Sondag-Huethorst, H.R.J. van Helleputte, L.G.J. Fokknik; ‘Generation of electrochemically deposited metal patterns by means of electron beam (nano) lithography of self-assembled monolayer resists’, Appl. Phys. Lett., 64, 1994, p 285

13 M. Lee, C.-U. Kim; ‘Investigation on self-aligned HgTe nano-crystals induced by controlled precipitation in PbTe-4HgTe quasi-binary compound semiconductor alloys’, Physica B, 304 2001, p 267

14 D. Kim, K. Tomihira, S, Okahara, M. Nakayama; ‘Highly efficient preparation of size controlled CdS quantum dots with high photoluminescence yield’, J. Cryst. Gr., 310, 2008, p 4244

15 R. F. C. Farrow, ‘Molecular Beam Epitaxy – Application to key materials’, Noyes Publications, p 2

16 J. G. Amar, F. Family; ‘Critical cluster size: Island morphology and size distribution in sub monolayer epitaxial growth’, Phys. Rev. Lett., 74 (11), 1995, p 2066

17 V. Bressler-Hill, S. Varma, A. Lorke, B. Z. Nosho, P. M. Petroff, W. H. Weinberg;' Island scaling in strained heteroepitaxy: InAs/GaAs (001)', Phys. Rev. Lett., 74 (16), 1995, p 3209

18 S. Liu, L. Bönig, J. Detch, H. Metiu;' Sub monolayer growth with repulsive impurities: Island density scaling with anomalous diffusion', Phys. Rev. Lett., 74 (22), 1995, p 4495

19 G. S. D. Bales, D. C. Charzan;' Transition from compact to fractal islands during sub monolayer epitaxial growth', Phys. Rev. Lett., 74 (24), 1995, p 4879

20 N. P. Kobayashi, T. R. Ramachandran, P. Chen, A. Madhukar; 'In situ atomic force microscopy of InAs three dimensional islands on GaAs (001)', Appl. Phys. Lett., 68, 1996, p 3299

21 D. Vanderbilt,' Shape transition in growth of strained islands: spontaneous formation of quantum wires', Phys. Rev. Lett., 70, 1993, p 2782

22 V. A. Shchukin, A. I. Borovkov, N. N. Ledenstov, D. Bimburg; 'Tuning and breakdown of faceting under externally applied stress', Phys. Rev. B, 51, 1995, p 10104

23 V. A. Shchukin, A. I. Borovkov, N. N. Ledenstov, P. S. Kop'ev; 'Theory of quantum wire formation on corrugated surface', Phys. Rev. B, 51, 1995, p 17767

24 K-O. Ng, D. Vanderbilt; 'Stability of periodic domain structures in a two dimensional dipolar model', Phys. Rev. B, 52, 1995, p 2177

25 Daruka, A-L. Barabasi; 'Dislocation free island formation in heteroepitaxial growth: A study at equilibrium', Phys. Rev. Lett., 79, 1997, p 3708

26 V. A. Shchukin, N. N. Ledenstov, D. Bimberg; ' Epitaxy of Nanostructures', Springer, 2004, p 16

27 L. D. Landau, E. M. Lifshitz;' Statistical physics: part I, Pergammon, New York, 1980

28 Y. Cho, J. R. Arthur;' Molecular beam epitaxy', Prog. In Solid State Chem., 10, 1975, p 157

29 Y. Cho, J. R. Arthur;' Molecular beam epitaxy', Prog. In Solid State Chem., 10, 1975, p 141

30 L. Däweritz, R. Hey;' Reconstruction and defect structure of vicinal GaAs (001) and AlGaAs (001) surfaces during MBE growth', Surf. Sci., 236, 1990, p 15

31 W. G. Schmidt, F. Bechstedt, J. Bernholc; 'GaAs (001) surface reconstructions: geometries, chemical bonding and optical properties', Appl. Surf. Sci., 190, 2002, p 264

32 L. Reimer, 'Transmission electron microscopy: Physics of image formation and microanalysis', Springer series in optical sciences, Springer-Verlag, 2nd Ed, 1989

33 J. W. Matthews, A. E. Blakeslee, S. Mader; 'Use of misfit strain to remove misfit dislocations from epitaxial thin films', Thin Solid Films, 33, 1976, p 253

34 D. D. Perovic, G. C. Weatherly, J.-M. Baribeau, D. C. Houghton; 'Heterogeneous nucleation sources in molecular beam epitaxy-grown Ge_xSi_{1-x}/Si strained layer superlattices', Thin Solid Films, 183, 1989, p 141

35 ASTM F1404 – 92 (2007) Test Method for Crystallographic Perfection of Gallium Arsenide by Molten Potassium Hydroxide (KOH) Etch Technique

36 E. A. Fitzgerald, D. G. Ast, P. D. Kirchner, G. D. Pettit, and J. M. Woodall; 'Structure and recombination in InGaAs/GaAs heterostructures', J. Appl. Phys., 63, 1988, p 693

37 E. A. Fitzgerald, P. D. Kirchner, G. D. Pettit, J. M. Woodall, D. G. Ast; 'Dislocations and Interfaces in Semiconductors', TMS, Warrendale, 1988, p 173

38 E. A. Fitzgerald, G. P. Watson, R. E. Proano, D. G. Ast, P. D. Kirchner, G. D. Pettit, J. M. Woodall; 'Nucleation mechanisms and the elimination of misfit dislocations at mismatched interfaces by reduction in growth area', J. Appl. Phys., 65, 1989, p 2220

39 E. A. Fitzgerald, P. D. Kirchner, R. Proano, G. D. Pettit, J. M. Woodall, D. G. Ast; 'Elimination of interface defects in mismatched epilayers by a reduction in growth area', App. Phy. Lett., 52, 1988, p 1496

40 E. A. Fitzgerald, Y.-H. Xie, M. L. Green, D. Brasen, A. R. Kortan, J. Michel, Y.-J. Mii, B. E. Weir; ' Totally relaxed GexSi1-x layers with low threading dislocation densities grown on Si substrates', App. Phys. Lett., 59, 1991, p 811

41 G. W. Bryant, G. S. Solomon; 'Optics of quantum dots and wires', Artech House, 2005, p 5

42 L. P. R. Kassab, L. Ferreira Frietas, K. Ozga, M. G. Brik, A. Wojciechowski; 'ZnO–TeO2–Yb/Tm glasses with silver nano-particles as laser operated quantum electronic devices', Opt. Las. Tech., 42, 2010, p 1340 – 1343.

43 N. J. Ekins-Daukes, I. Ballard, C. D. J. Calder, K. W. J. Barnham, G. Hill, J. S. Roberts; 'Photovoltic efficiency enhancement through thermal up-conversion', App. Phys. Lett., 82, 2003, p 1974

44 P. L. Souza, M. P. Pires, B. Yavich, F. Racedo, C. V-B. Tribuzy; 'Amplitude modulators based on Stark effect', Microelec. Jou., 33, 2002, p 341 – 348

45 J. Skromme, A. Sasikumar, B. M. Green, O. L. Hartin, C. E. Weitzel, M. G. Miller; 'Reduction of low-temperature nonlinearities in pseudomorphic AlGaAs/InGaAs HEMTs due to Si-related DX centers', IEEE Trans. Elec. Dev., 57 (4), 2010, p 749 – 754

46 Y.-J. Xiong, B.-K. Xiong; 'Resonant transport through graphene nanoribbon quantum dots', J. App. Phys. 109, 2011, p 103707

47 H. Kong, H. K. Cho, M. Y. Kim, R. J. Choi, B. K. Kim; 'Strain variation p-GaN by different spacer layers in the light emitting diodes and their micro structural and emission behaviors', J. Cryst. Gr., 312, 2010, p 2128 – 2132

48 G. M. Jones, B. H. Hu, C. H. Yang, M. J. Yang, Y. B. Lyanda-Geller; 'Observation of one-electron charge in an enhancement-mode InAs single-electron transistor at 4.2 K', App. Phys. Lett., 88, 2006, p 192102

49 L. Nevou, V. Liverini, F. Castellano, A. Bismuto, J. Faist; 'Asymmetric heterostructure for photovoltaic InAs quantum dot infrared photodetector', App. Phys. Lett., 97, 2010, p 23505

50 H. J. Queisser, 'Photovoltaic conversion at reduced dimensions', Physica E, 14, 2002, p 1

51 V. A. Shchukin, N. N. Ledenstov, D. Bimberg; Epitaxy of Nanostructures, Springer, 2004, p 167

52 Ratsch, A. Zangwill; 'Equilibrium theory of Stranski-Krastanov epitaxial morphology', Surf. Sci. 293, 1993, p 123

53 R. Niedermayer, Thin Films, 1, 1968, p 25

54 S.M. Pintus, S.I. Stenin, A.I. Toropov, E.M. Trukhanov, V.Yu. Karasyov; 'Morphological transformations of thin heteroepitaxial films', Thin Solid Films, 151, 1987, p 275

55 C. W. Snyder, J. F. Mansfield, and B. G. Orr; 'Kinetically controlled critical thickness for coherent islanding and thick highly strained pseudomorphic films of InxGa1-xAs on GaAs(100)', Phys. Rev. B, 46, 1992, p 9551

56 V. A. Shchukin, N. N. Ledenstov, V. M. Ustinov, Yu. G. Musikhin, V. B. Volovik, A. Schliwa, O. Stier, R. Heitz, D. Bimberg; Mat. Res. Soc. Symp. Proc., 618, 2000, p 79

57 N. N. Ledenstov, V. A. Shchukin, D. Bimberg, V. M. Ustinov, N. A. Cherkashin, Yu. G. Musikhin, B. V. Volovik, G. E. Cirlin, Zh. I. Alferov; 'Semicon. Sci. Tech. 16, 2001, p 502

58 N. N. Ledenstov, M. Grundman, N. Kirstaedter, O. Schmidt, R. Heitz, J. Böhrer, D. Bimberg, V. M. Ustinov, V. A. Shchukin, P. S. Kop'ev, J. Heydenreich; Proc. 7th Int. Conf. Mod. Semi. Str., 1995; Sol. St. Elec., 40, 1996, p 785

59 Y.-Y. Lin, J. Singh; 'Self-assembled quantum dots: A study of strain energy and intersubband transitions', J. Appl. Phys., 92, 2002, p 6205

60 P. N. Keating, 'Effect of invariance requirements on the elastic strain energy of crystals with application to the diamond structure', Phys. Rev., 145, 1966, p 637

61 R. M. Martin, 'Elastic Properties of ZnS Structure Semiconductors', Phys. Rev. B, 1, 1969, p 4005

62 S. Krishna, J. Sabarinathan, K. Linder, P. Bhattacharya, B. Lita, R. S. Goldman; 'Growth of high density self-organized (In,Ga)As quantum dots with ultranarrow photoluminescence linewidths using buried In(Ga,Al)As stressor dots', J. Vac. Sci. Technol. B, 18, 2000, p 1502

63 S. Tomić, P. Howe, N. M. Harrison, T. S. Jones; 'Theoretical analysis of strain and strain decay in InAs/GaAs (001) multilayer quantum dot growth', J. Appl. Phys., 99, 2006, p 093522

64 Q. Xie, A. Madhukar, P. Chen, N. Kobayashi; 'Vertically self-organized InAs quantum box islands on GaAs (001)', Phys. Rev. Lett., 75, 1995, p 2542

65 S. M. Sze, 'Physics of semiconductor devices', John Wiley and Sons, 1981.

66 J. Nelson, 'The Physics of solar cells', Imperial College Press, 2003

67 P. T. Landsberg, Recombination in Semiconductors, Cambridge university press, 1991

68 C. T. Sah, R. N. Noyce, W. Shockley; Proc. Inst. Radio Eng., 45, 1957

69 A. Lindholm, J. G. Fossum, E. L. Burgess; 'Application of the superposition principle to solar-cell analysis', IEEE Trans. Elec. Dev., 26, 1979, p 165

70 M. A. Green, 'Prospects for photovoltaic efficiency enhancement using low-dimensional structures', Nanotech., 11, 2000, p 401

71 W. Shockley, H. J. Queisser; 'Detailed balance limit of efficiency of *p-n* junction solar cells', J. Appl. Phys., 32, 1961 p 510

72 Luque, A. Marti; 'Increasing the efficiency of ideal solar cells by photon induced transitions at intermediate levels', Phys. Rev. Lett., 1997, p 5014

73 V. I. Klimov, 'Detailed balance power conversion limits of nanocrystal-quantum-dot solar cells in the presence of carrier multiplication', App. Phys. Lett., 89, 2006, p 123118

74 N. J. Ekins-Daukes, J. M. Barnes, K. W. J. Barnham, J. P. Connolly, M. Mazzer, J. C. Clark, R. Grey, G. Hill, M. A Pete, J. S. Roberts; 'Strained and strain-balanced quantum well devices for high-efficiency tandem solar cells', Sol. En. Mat. Sol. Cel., 68, 2001, p 71

75 N. J. Ekins-Daukes, K. Kawaguchi, J. Zhang; 'Strain-balanced criteria for multiple quantum well structures and its signature in X-ray rocking curves', Cryst. Gr. Design, 2, 2002, p 287

76 S. M. Hubbard, C. G. Bailey, C. D. Cress, S. Polly, J. Clark, D. V. Forbes, R. P. Raffaelle, S. G. Bailey, D. M. Wilt; 'Short circuit current enhancement of GaAs solar cells using strain compensated InAs quantum dots', 33rd Photovolt. Spec. Conf., 2008, San Diego, CA

77 C. G. Bailey, S. M. Hubbard, D. V Forbes, R. P. Raffaelle; 'Evaluation of strain balancing thickness for InAs/GaAs quantum dot arrays using high resolution x-ray diffraction and photoluminescence', App. Phys. Lett., 95, 2009, p 203110

78 R. Oshima, T. Hashimoto, H. Shigekawa, Y. Okada; 'Multiple stacking of self-assembled InAs quantum dots embedded by GaNAs strain compensating layers', J. App. Phys., 100, 2006, p 083110

79 C. G. Bailey, D. V. Forbes, R. P. Raffaelle, S. M. Hubbard, 'Near 1 V open circuit voltage InAs/GaAs quantum dot solar cells', App. Phys. Lett., 98, 2011, p 163105

CHAPTER 3

1 Y. Cho, J. C. Tracey; US Patent 3, 969, 164, 1976

2 Y. Cho, H.C. Casey, C. Radice, P. W. Foy; 'Influence of growth conditions on the threshold current density of double heterostructure lasers prepared by molecular beam epitaxy', Elec. Lett., 16 (2), 1980, p 72

3 J. P. Contour, J. Massies, A. Saletes; 'X-ray photoelectron spectroscopy study of GaAs (001) surface thermo cleaning prior to molecular beam epitaxy', Appl. Phys. A, 38, 1985, p 45

4 http://www.microchemicals.com/photoresist/photoresist_az_5214_e_eng.htm

5 Kittel, 'Introduction to solid state physics', Wiley, 6th Ed, 1986, p 29

6 V. A. Shchukin, N. N. Ledenstov, D. Bimberg, Epitaxy of Nanostructures, Springer, 2004, p 296

7 K. Schroder, 'Semiconductor material and device characterization', Wiley Intersciene, 1990, p 3

CHAPTER 4

1 V. A. Shchukin, N. N. Ledenstov, D. Bimberg; ‘ Epitaxy of Nanostructures’, Springer, 2004, p 16

2 A. Y. Cho, J. R. Arthur;’ Molecular beam epitaxy’, Prog. In Solid State Chem., 10, 1975, p 15

3 L. Reimer, ‘Transmission electron microscopy: Physics of image formation and microanalysis’, Springer series in optical sciences, Springer-Verlag, 2nd Ed, 1989

4 S. Adachi, ‘Physical properties of III-V semiconductor compounds’, John Wiley & Sons, 1992, p 4

5 Z. Mi, J. Yang, P. Bhattacharya; ‘Molecular beam epitaxial growth and characteristics of ultra-low threshold 1.45 μm metamorphic InAs quantum dot lasers on GaAs’, J. Cryst. Gr., 301-302, 2007, p 923

6 L. Reimer, ‘Transmission electron microscopy: Physics of image formation and microanalysis’, Springer series in optical sciences, Springer-Verlag, 2nd Ed, 1989, p 283

7 O. Auciello, A. R. Krauss; ‘In-situ real time characterization of thin films’, Wiley-Interscience, 2001, p 37

8 A. Feltrin, A. Freundlich; ‘RHEED metrology of Stranski-Krastanov quantum dots,’ J. Cryst. Gr., 301-302, 2007, p 38

9 M. J. da Silva, A. A. Quivy, S. Martini, T. E. Lamas, E. C. F. da Silva, J. R. Leite; ‘Large InAs/GaAs quantum dots with an optical response in the long wavelength region’, J.. Cryst. Gr., 278, 205, p 103

10 B. Ilahi, L. Sfaxi, E. Tranvoues, G. Bremond, M. Baira, C. Bru-Chevalier, H. Maaref; 'Toward long wavelength low density InAs/GaAs quantum dots’, Phys. Lett. A, 357, 2006, p 360

11 V. A. Shchukin, N. N. Ledenstov, D. Bimberg, Epitaxy of Nanostructures, Springer, 2004, p 211

12 V. A. Shchukin, N. N. Ledenstov, D. Bimberg, Epitaxy of Nanostructures, Springer, 2004, p 209

13 S. Guha, A. Madhukar, K. C. Rajkumar; 'Onset of Incoherency and defect introduction in the initial stages of molecular beam epitaxial growth of highly strained $In_xGa_{1-x}As$ on GaAs (100)', Appl. Phys. Lett., 57 (20), 1990, p 2110

14 V. A. Shchukin, N. N. Ledenstov, D. Bimberg, Epitaxy of Nanostructures, Springer, 2004, p 296

15 T. Kaizu, M. Takahasi, K. Yamaguchi, J. Mizuki; 'Modification of InAs quantum dot structure during annealing', J. Cryst. Gr., 301-302, 2007, p 248

16 P. B. Joyce, T. J. Krzyzewski, G. R. Bell, T. S. Jones, S. Malik, D. Childs, R. Murray; 'Effect of growth rate on the size, composition and optical properties of InAs/ Gas quantum dots grown by molecular-beam epitaxy', Phys. Rev. B, 62 (16), 2000, p 10891

17 C. Guille, F. Houzay, J. M. Moison, F. Barthe; 'Intermixing at InAs/GaAs and GaAs/InAs interfaces', Surf. Sci., 189/190, 1987, p 1041

18 F. Houzay, J. M. Moison, C. Guille, F. Barithe, M. van Rompay; 'Surface segregation of third-column atoms in III-V ternary arsenides', J. Cryst. Gr., 95, 1989, p 35

19 J. M. Moison, F. Houzay, F. Barthe, J. M. Gerard, B. Jusserand, J. Massies, F. S. Turco-Sandroff', Surface segregation in III-V alloys', J. Cryst. Gr., 111, 1991, p 141

20 I. Mukhametzanov, Z. Wei, R. Heitz, A. Madhukar; 'Punctuated island growth: an approach to examination and control of quantum dot density, size and shape evolution', Appl. Phys. Lett., 75 (1), 1999, p 85

21 O. Madelung, 'Landolt-Bornstein numerical data and functional relationships in science and technology', vol. 22, Springer-Verlag, 1987, p 82

22 C. Kittel, 'Introduction to solid state physics', John Wiley & Sons, 1986, p 106

23 S. Ghanad-Tavakoli, M. A. Naser, D. A. Thompson, M. J. Deen; 'Experimental characterization and theoretical modeling of the strain effect on the evolution and

interband transitions of InAs quantum dots on $In_xGa_{1-x}As$ ($0.0 \leq x \leq 0.3$) metamorphic pseudo substrates on GaAs wafers', J. Appl. Phys., 106, 2009, p 063533

CHAPTER 5

1 F. C. Frank, J. H. Van der merwe; 'One-dimensional dislocations. II. Misfitting monolayers and oriented overgrowth', Proc. Roy. Soc. Lond. A, 198, 1949, p 216

2 F. C. Frank, J. H. Van der Merwe; 'One-dimensional dislocations. IV. Dynamics', Proc Roy. Soc. Lond. , 201, 1950, p 261

3 R. People, J. C. Bean; 'Calculation pf critical layer thickness versus lattice mismatch for Ge_xSi_{1-x}/ Si strained layer heteroctructures', Appl. Phys. Let. 47, 1985, p 322

4 J. W. Matthews, A. E. Blakeslee; 'Defects in epitaxial multilayers', J. Cryst. Gr., 27, 1974, p 118

BIOGRAPHICAL INFORMATION

Jateen S. Gandhi received his B.E. degree in Polymer Science and Engineering at Maharashtra Institute of Technology, Pune, India, in 2002. In 2004 he received his M.S. degree in Materials Science and Engineering at The University of Texas at Arlington, under the supervision of Dr. Ronald L. Elsenbaumer. He then worked for Alpla, Inc. in Jefferson City, MO as a Process Engineer until Summer 2005. In Fall 2005 he began work as a full-time Ph.D. candidate under a joint guidance of Dr. Wiley P. Kirk and Dr. Choong-un Kim. His research project was focused on epitaxial growths of defect-free quantum-dots based semiconductor devices. He desires to work in the semiconductor research field.